AD-774 310

ANALYSIS AND EVALUATION OF RADOME MATERIALS AND CONFIGURATIONS FOR ADVANCED RF SEEKERS

E. B. Joy, et al

Georgia Institute of Technology

Prepared for:

Army Missile Command

31 January 1974

Best
Available
Copy

GEORGIA INSTITUTE OF TECHNOLOGY

FINAL REPORT
PROJECTS E-21-628 and A-1535

ANALYSIS AND EVALUATION OF RADOME MATERIALS AND
CONFIGURATIONS FOR ADVANCED RF SEEKERS

by

E. B. Joy and G. K. Huddleston
School of Electrical Engineering

and

H. L. Bassett, C. W. Gorton and S. H. Bomar, Jr.
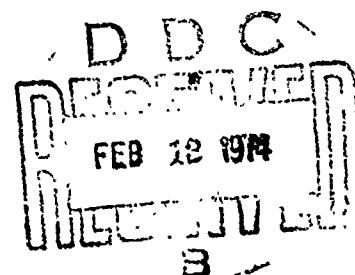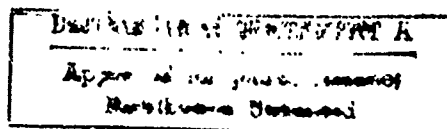Engineering Experiment Station

Contract No. DAAH01-73-C-0796

31 January 1974

DDC
FEB 12 1974
B

FOREWORD

This final research report was prepared jointly by the School of Electrical Engineering and the Engineering Experiment Station of the Georgia Institute of Technology, Atlanta, Georgia, under Contract No. DAAH01-73-C-0796. This contract was initiated by the RF Guidance Technology Branch of the Advanced Sensors Directorate, Research, Development, Engineering and Missile Systems Laboratory, U. S. Army Missile Command, Redstone Arsenal, Alabama. The contract was administered under the direction of Carlton H. Cash and Thomas W. Morgan of the RF Guidance Technology Branch.

The period of performance covered by this report extends from 1 May 1973 to 31 December 1973.

Report authors are: Edward B. Joy and Gene K. Huddleston of the School of Electrical Engineering and Harold L. Bassett, Charles W. Gorton and Steve H. Bomar, Jr., of the Engineering Experiment Station. Other personnel participating in this work includes Earle A. Welsh, Research Engineer, and James N. Farmer, Student Assistant.

The views and conclusions contained in this document are those of the authors and should not be interpreted as necessarily representing the official policies, either expressed or implied, of the U. S. Army Missile Command or the U. S. Government.

TABLE OF CONTENTS

iii

LIST OF FIGURES

LIST OF TABLES

SECTION I

INTRODUCTION

This report describes the results of a research program to select, analyze, and evaluate various radome materials and configurations in order to determine a preliminary design of a radome which can be used with advanced RF seekers operating over the 8.0 to 18.0 GHz frequency band and physically constrained for operation in a five-inch (outside) diameter missile.

The basic radome configuration considered consists of a tangent ogive shape surmounting a cylinder and an n-order monolithic wall structure. Attention is directed toward the first-order (half-wave) wall structure because of its superior bandwidth compared to the higher order structures; furthermore, the 5-inch outside diameter requirement dictates as thin a wall as possible to allow room inside for the antenna system. Details of the radome shape and position of the antenna inside the radome are given in the drawing of Figure 11.

The radome design process described herein follows the natural course of determining the temperatures and mechanical stresses to be encountered, selecting candidate radome materials, and assessing the effects of radome shape and radome material on the electrical performance of the seeker system. Based on these results, a radome design is selected which yields the best electrical performance while meeting the requirements of the flight environment.

Section II presents a discussion of the assumed aerodynamic heating and drag considerations for the radome under study. The range of temperatures

1

and effects of radome fineness ratio on missile trajectory and range are also presented.

Section III presents electrical and mechanical data for candidate radome materials. Criteria for selecting a single material from among those studied are also discussed.

Section IV presents computed electrical performance data for a number of radome configurations.

The conclusions drawn from the data presented are given in Section V. A radome design is also recommended.

SECTION II

AERODYNAMIC HEATING AND DRAG

1. Introduction

One of the first steps in the design of any radome is the determination of the effects of the flight environment on the radome. One of the most important effects to be determined is the range of temperatures and stresses to be encountered by the radome following a specified trajectory. Another important effect is that of the shape of the radome on the missile trajectory. These effects of temperature, stress, and radome shape are important because they influence greatly the choice of radome material and, ultimately, the electrical performance of the seeker antenna system enclosed by the radome.

In this section, the aerodynamic heating and drag considerations are examined. Upper bounds on radome temperatures are calculated independently of the radome material, radome shape, and trajectory by using a steady-state analysis and a flat plate assumption. These results, presented in Table I, influence the initial choice of candidate radome materials. Following the calculation of upper bounds on the temperature, the results of a transient temperature analysis are presented for three candidate materials. The transient analysis does account for the flight trajectory and radome material. The effects of the radome shape and wall thickness on the mechanical stresses and missile trajectory are also calculated and presented.

3

2.   Aerodynamic Heating

The initial calculations related to aerodynamic heating were the determination of the stagnation temperature, the flat plate laminar recovery temperature, and the flat plate turbulent recovery temperature. The stagnation temperature is the upper bound on the temperature that any location on the radome surface can reach. Physically, it is the temperature attained by the air flowing around the radome (at the outer edge of the boundary layer) at the stagnation point on the radome. For a radome at zero angle of attack, the stagnation point is the radome tip. Actually, the outer surface of the radome at the stagnation point will reach a temperature that is less than the stagnation temperature because of thermal radiation from the surface and heat conduction into the radome material. The recovery temperatures calculated correspond to the temperature of a thin plate placed parallel to the flow under adiabatic conditions; i.e., internal conduction and thermal radiation are assumed to be zero. Physically, the recovery temperatures represent an upper bound of the outer surface temperature in the aft region of a pointed radome. Whether the laminar or turbulent recovery temperature is considered depends on whether the boundary layer is laminar or turbulent at the point under consideration. The results of the calculations of stagnation and recovery temperatures are presented in Table I. These calculations are based on sea-level conditions for a standard day under steady-state conditions.

The transient temperature response of the hemispherical radome was determined at the stagnation point by means of finite difference equations and the aid of a high-speed digital computer. Inputs to the computer-aided

4

TABLE I

STAGNATION AND RECOVERY TEMPERATURES

		Temperatures	
Flight Velocity (meters/sec.)	Stagnation ($^\circ$F)	Laminar Recovery ($^\circ$F)	Turbulent Recovery ($^\circ$F)
0	59	59	59
200	95	90	91
400	202	180	185
600	380	330	342
800	623	537	555
1000	925	796	826

temperature analysis included radome material properties, nose radius, radome wall thickness, and flight velocity as a function of time. The radome material properties needed for determining temperature profiles are density, specific heat, thermal conductivity, and surface emittance. In addition, the coefficient of thermal expansion, modulus of elasticity, and Poisson's ratio were used as inputs so that thermal stresses could be calculated. Also, a heat transfer coefficient for the outside surface (front side) and a boundary condition for the inside surface (back side) of the radome were specified. The heat transfer coefficient was calculated using an equation relating nose radius and flight velocity for sea level flight. The equation used is an empirical relationship which was developed following

the procedure recommended by van Driest [1]. The back side of the radome was assumed to be perfectly insulated; this is a fairly universal assumption which uncouples the transient radome heating from the thermal response of the contents of the radome. Although a variety of intermediate results are obtained, those of primary interest are front side temperature (to see if material temperature limits are exceeded), back side temperature (to see if the interior of the radome becomes too high in temperature), and thermal stress (to see if material failure will result). The calculations for the three materials of interest are presented in Figures 1 and 2. It is noted that the temperatures and thermal stresses shown in these figures are well within the operating limits of the three materials shown.

3. Radome Drag Coefficient

As the fineness ratio L/D of the radome is changed, the overall drag of the hypothetical missile changes, resulting in a modified trajectory. In investigating this effect, the modified trajectory was related to the original trajectory. The assumption was made that the overall drag coefficient was constant throughout the flight. The trajectory calculations for each fineness ratio were made using the same missile weight, fuel weight, thrust, and burn time. It is noted that the minimum velocity required for maneuverability is reached for a fineness ratio of 0.5 at about 0.67 on the normalized time axis of Figure 3. The results of these calculations are presented in Figure 3.

In order to evaluate the mechanical loading on the radome with an angle of attack, calculations were made using a ten degree angle of attack at the

6

Polyimide Quartz, t = 0.281"
Slip-cast Fused Silica, t = 0.301"
Pyroceram⑨ 9606, t = 0.230"

Back Surface Thermal Stress (psi)

3000
2500
2000
1500
1000
500
0
-500

0   5   10   15   20   25   30

Flight Time-Seconds

Figure 2. Back Surface Stress vs.
Flight Time for 3
Materials.

Temperature °F

400
350
300
250
200
150
100
50

F.S.
F.S.
F.S.
B.S.
B.S.
B.S.
B.S.

0   5   10   15   20   25   30

Flight Time-Seconds

Figure 1. Front Surface and Backside
Temperature vs. Flight Time
for 3 Materials.

7
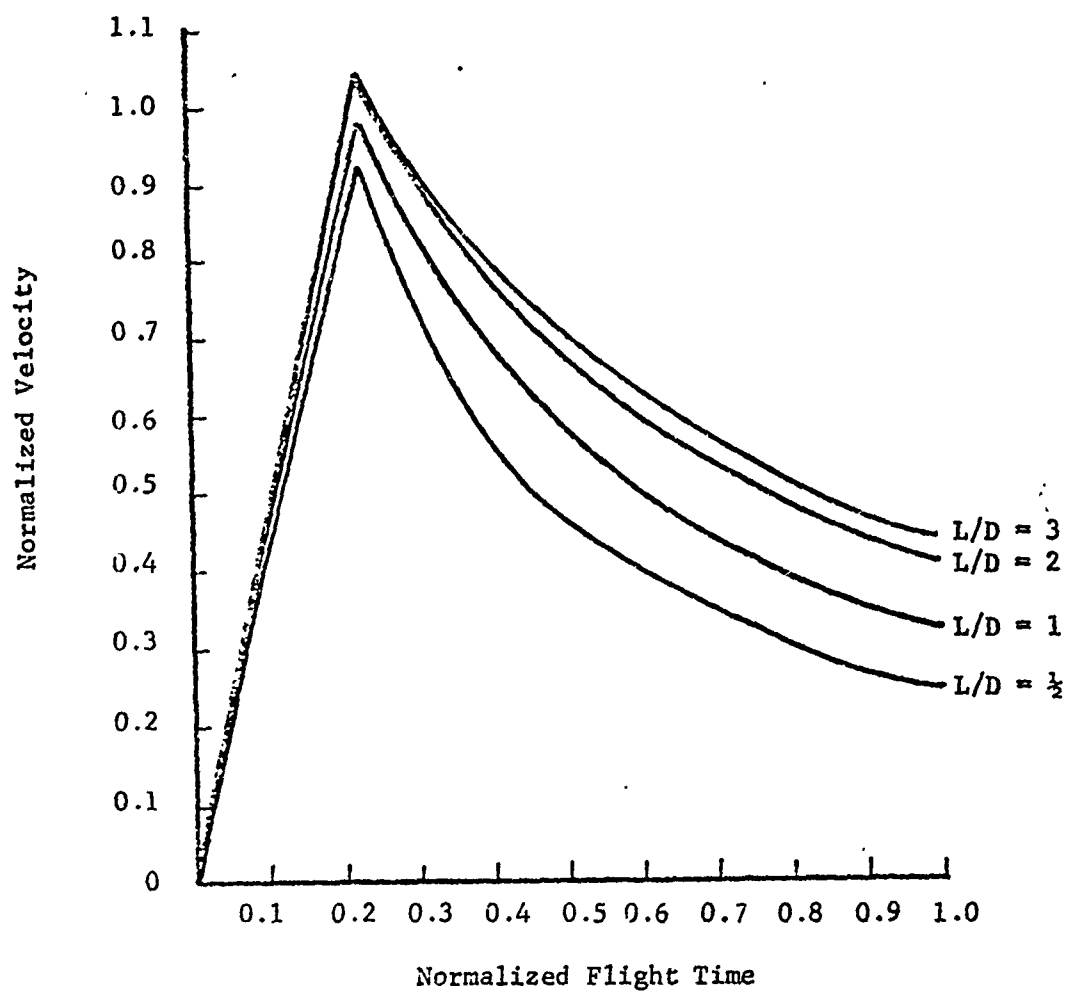
Figure 5. Change in Trajectory due to Radome Drag
Coefficient

8

maximum velocity in the trajectory. Sea level conditions were assumed. These calculations are based on a Newtonian pressure distribution using the results presented by Mayo [2]. The stresses are calculated from the aerodynamic axial load and bending moment. The results of these calculations are presented in Table II. The stresses indicated refer to the maximum compressive or tensile stress in the radome wall at the base of the radome. All of the stresses shown in Table II are small for the three materials of interest.

TABLE II

MECHANICAL LOADING AT MAXIMUM VELOCITY
ANGLE OF ATTACK = 10°

L/D	Radome Wall Thickness (inches)	Compressive Stress (p.s.i.)	Tensile Stress (p.s.i.)
½	0.250	224	0
½	0.375	153	0
1	0.250	242	< 1
1	0.375	170	< 1
2	0.250	450	348
2	0.375	330	242
3	0.250	698	642
3	0.375	500	462

SECTION III

RADOME MATERIALS SELECTION

1. Introduction

The thermal and mechanical data presented in Section II were used as guidelines in selecting candidate radome materials. The criteria used in selecting the materials were: (1) strength during peak temperatures, (2) thermal shock resistance, (3) microwave transmission properties, (4) weight, (5) fabricability, (6) rain erosion resistance, and (7) cost. Some of the materials considered are listed in Table III. The electrical properties of all the listed materials are relatively good up to the temperatures indicated and higher; e.g., measurements at Georgia Tech on polyimide-quartz samples indicate that the material will operate to at least 1000°F with only small degradation of electrical properties.

For background information and to put some of these materials into perspective, a review of the current operating radomes is in order. Glass reir   ed plastic radomes have been widely used to the range of Mach 3.

example, the B-1 aircraft radome is constructed of polyimide quartz.

er aircraft have used radomes made of glass reinforced polyesters, epoxies, and silicones. Available fibers include E-glass (most common), S-glass (slightly higher temperature capability than E-glass), fused quartz (highest temperature capability and most expensive), and PRD-49 (a high temperature organic fiber related to nylon and manufactured by DuPont). Other resins are available including polyurethane (low temperature capability used on commercial aircraft), silicones (good elevated temperature properties

TABLE III

CANDIDATE RADOME MATERIALS FOR HIGH PERFORMANCE AIRCRAFT AND MISSILES

Material	Decomposition or Melting Temp (°F)	Thermal Shock Resistance	Rain Erosion Resistance	Weight	Ease of Fabrication	Relative Cost
Glass reinforced polyester	250-300	good	poor	low	good	low
Glass reinforced epoxy	300-400	good	poor	low	good	low
Glass reinforced polyimide	600	good	poor	low	good	low
Glass reinforced polybenzimidazole		(competitive with polyimide)				
Aluminum oxide	3630	poor	excellent	high	good	low
Slip-cast fused silica	3140	excellent	poor	low	good	low
Beryllium oxide	4620	good	excellent	high	good	high
Cordierite	2460	good	good	high	good	low
Hot pressed boron nitride	4950	excellent	poor	low	poor	high
Isotropic pyrolytic boron nitride	4950	excellent	poor	low	poor	high
Reaction sintered silicon nitride	3400	excellent	good	high	good	(?)

but low strength), phenyl silanes (similar to silicones, used on the F-14 aircraft), Teflon (non-charring ablator), and polybutadiene (a newly developed high temperature resin, manufactured by Firestone). With present technology, none of the multitude of fiber reinforced resin systems can be expected to find applications above Mach 3 to 3.5. However, this class of materials is experiencing st idy development for uses up to this range of Mach numbers; polybutadiene resin and PRD-49 are the newest additions, just now becoming available in commercial quantities. As a class, the glass fiber reinforced plastics are usually preferred over ceramics for radome applications where mission requirements are mild enough for them to operate successfully. They do not suffer from the brittleness of ceramics, are light weight, relatively easy to fabricate, and relatively low in cost.

Aluminum oxide has been used for missile radomes operating up to about Mach 3. One example is the Sparrow III air-to-air missile. This material has excellent rain erosion resistance, but above Mach 3 it cannot survive the thermal shock resulting from aerodynamic heating.

Cordierite (PYROCERAM 9606[R] and Rayceram III) has been used for radomes up to about Mach 4. It is used on the Navy's Standard Missile for surface to air, anti-aircraft operation. Cordierite has good rain erosion resistance, but a low melting point and moderate thermal shock capability. It was a leading candidate for the Army's Sam-D missile, but was eventually discarded in favor of slip-cast fused silica because of thermal shock considerations and the fact that it is manufactured by a proprietary process. It was a candidate, however, for this program and was carefully considered as the radome material.

13

Slip-cast fused silica presently appears to be the only candidate radome material for use above Mach 6. That does not mean, however, that it is excluded as a candidate material at lower speeds. This material is being used on the SAM-D program and has been a candidate for other missile programs. This material has excellent thermal shock resistance, but has poor rain erosion resistance. Fabrication technology has reached the point of commercial reliability, and the cost is moderate.

Boron nitrides, both hot pressed and isotropic pyrolytic boron nitride, have excellent thermal shock resistance but poor rain erosion resistance. They have not been seriously considered for radomes because they cannot be fabricated in large shapes; even if fabrication technology were developed, the cost would probably be prohibitive. They are both good candidates for small windows operating to Mach 8 or higher.

Beryllium oxide has excellent rain erosion resistance and good thermal shock resistance. It has never been used for an operational radome, primarily because of the toxic nature of finely divided beryllium oxide powders. Costs of machining with the required safety precautions are prohibitive. It has been used for high power transmission windows.

Reaction sintered silicon nitride is a new material currently under development for possible radome use. Potentially, it offers good thermal shock resistance in aerodynamic heating, much better rain erosion resistance and higher strength than fused silica. It probably will operate into the Mach 6 range. Fabrication techniques and cost should be comparable to fused silica, but this material is not yet ready for commercial production.

From the preceding discussion of candidate radome materials, several

observations are apparent:

(1) Various materials, including glass fiber reinforced plastics
     and aluminum oxide, are suitable for radomes up to Mach 3.

(2) Cordierite is suitable for radomes up to about Mach 4 or 5.

(3) Slip-cast fused silica is presently the only strong candidate
     for radomes in the range above Mach 5. This material has re-
     latively low strength and poor rain erosion resistance. Reaction
     sintered silicon nitride may offer relief from these deficiencies,
     up to about Mach 6, with further development.

(4) Beryllium oxide and the boron nitrides are not suitable for
     radomes because of fabrication difficulties and cost; they are
     useable for dielectric windows with isotropic pyrolytic boron
     nitride being useable up to very high Mach numbers.

2. Materials Data

For the application of concern here, four candidate radome materials

were considered: polyimide-quartz, glass reinforced polybenzimidazole,

slip-cast fused silica and cordierite (Pyroceram 9606®). For comparison

purposes, the strength properties of four glass fiber reinforced plastic

materials are plotted in Figure 4. The strength properties of the PBI

laminates are plotted in Figures 5 and 6. The ceramic material strength

properties are plotted in Figure 7. Alumina is included here for com-

parison purposes. The radome stresses shown in Figure 2 of Section II are

very low compared to the maximum stress that the materials will withstand.

Both the polyimide/E-Glass BPI-373 and the polyimide quartz BPI-373 maintain

good strength properties to $800°F$. The PBI laminate possesses slightly

better properties as indicated in Figure 5.
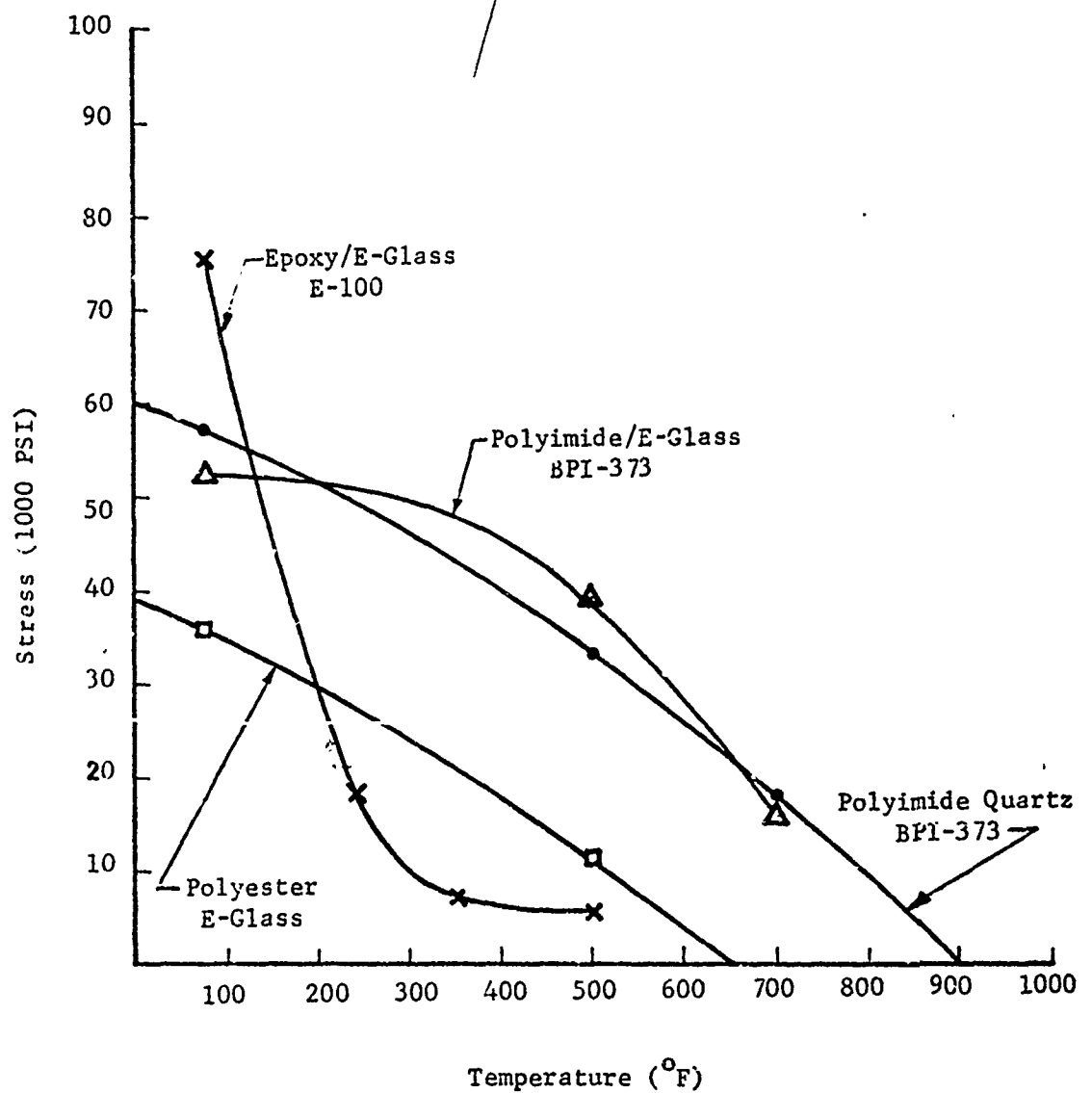
Figure 4. Maximum Flexural Stress of Four Glass Fiber Reinforced
           Plastic Materials as a Function of Test Temperature [3]

16
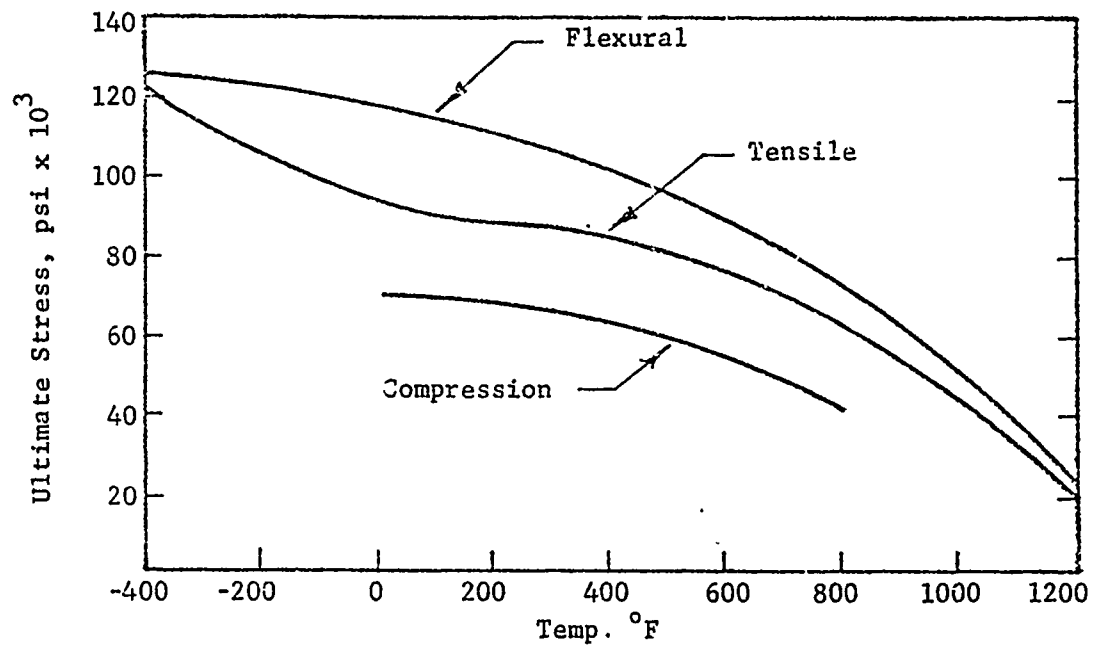
Figure 5. Strength Properties versus Temperature for
PBI Laminate (Imidite 1850/1581 S-Glass
Fabric, HTS Finish) [4].
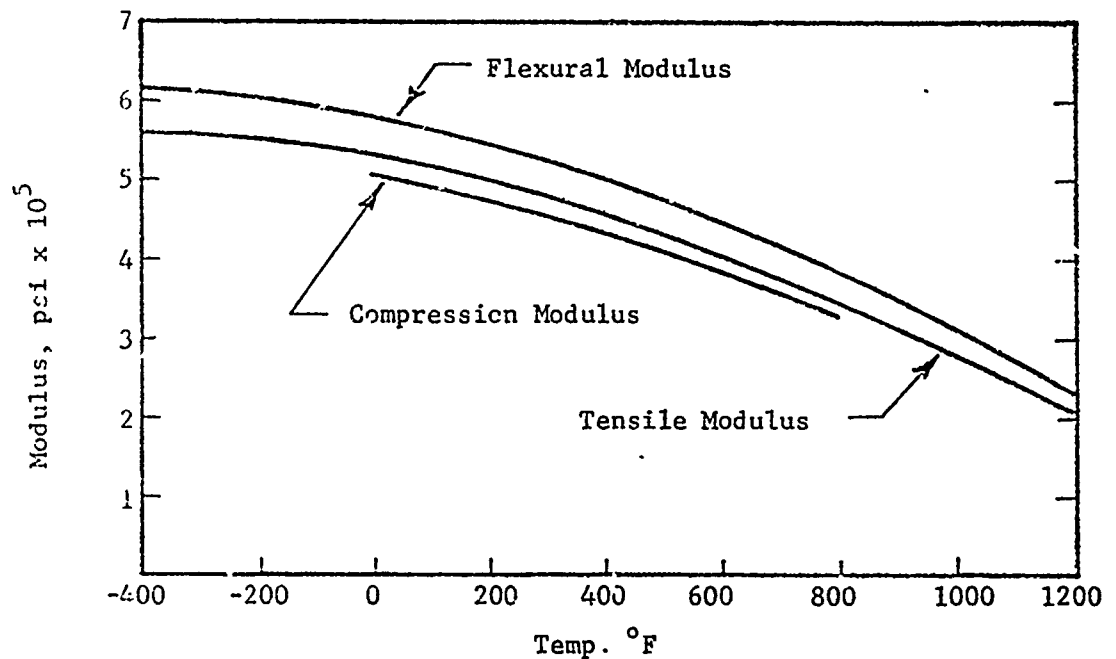
Figure 6. Elastic Modulus Properties versus
Temperature for PBI Laminates
(Imidite 1850/1581 S-Glass
Fabric, HTS Finish) [4].

17
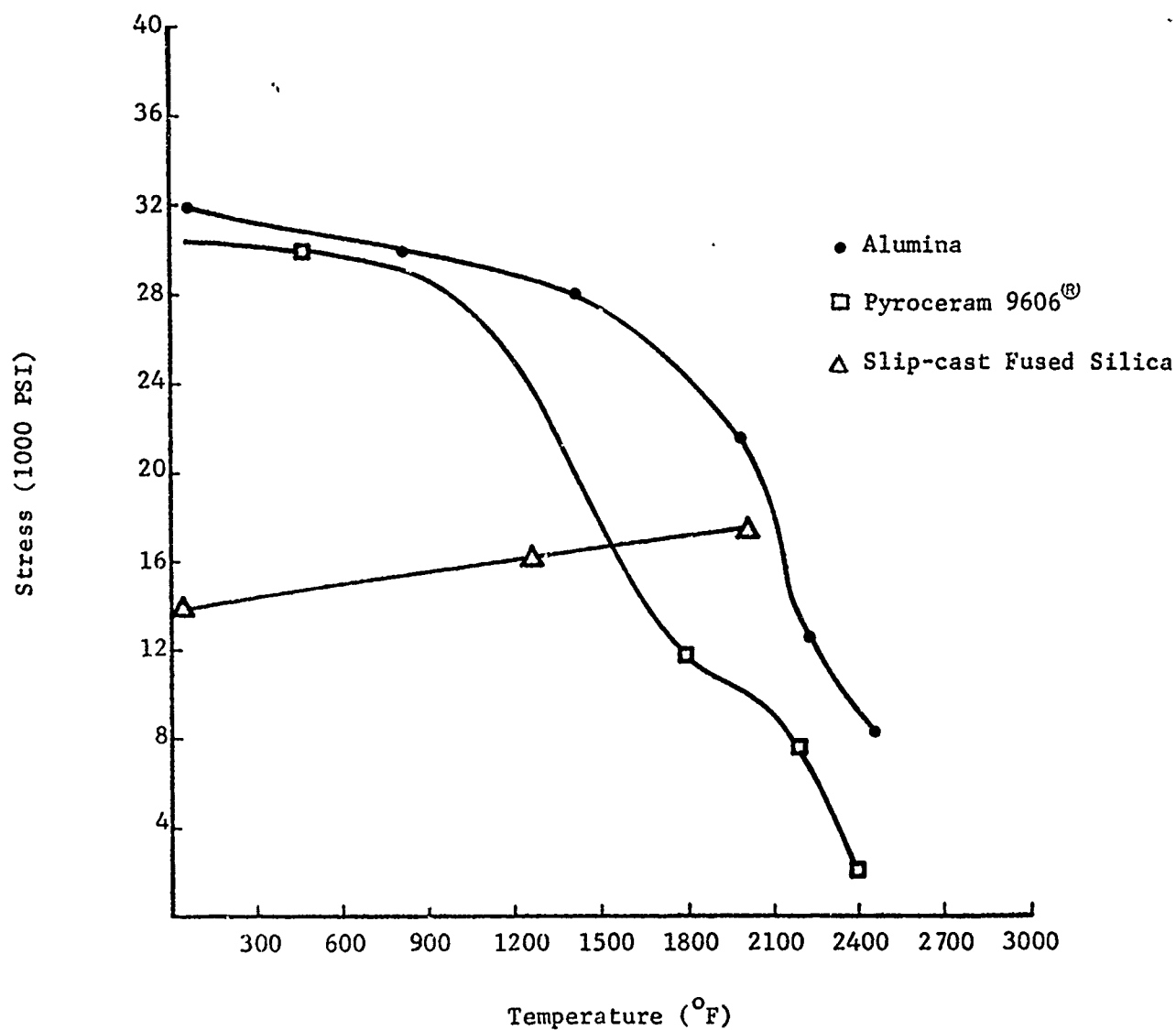
Figure 7. Maximum Flexural Stress of Ceramic Test Bars as
a Function of Test Temperature [3]

The other considerations for material properties were the electrical characteristics. As indicated in Figure 8, the dielectric constant of polyimide-quartz BPI-373 increases slightly from 3.25 to 3.3 over a temperature range from ambient to 600°F. This is a 1.5 percent increase and will not cause serious degradations in radome-antenna performance due to this effect. This change is also typical of PBI. The electrical properties of slip-cast fused silica and Pyroceram[®] shown in Figures 9 and 10 change very little over the operating temperature range shown in Figure 1. This particular property is a feature of the ceramic materials, and it is an advantage that is given due consideration when choosing a radome material. Fortunately, the maximum expected radome outer surface temperature is not very high so that the organic materials considered can survive the environment.

In general, the expected change in electrical performance of the radome due to the temperature dependence of the electrical properties is not significant for the four radome materials considered. The perused data are not included in this report on organic materials whose temperature-electrical performance fell below the two organics considered. For example, Epoxy/E-Glass E-100 has a 7 percent variation in dielectric constant from ambient to 600°F and its loss tangent is greater than 0.03. Similar results have been found with Polyester/E-Glass, Vibrin-135 and Polyimide/ E-Glass BPI-373.

Since the environment is such that an organic material will survive, it is advantageous to eliminate the ceramics and consider only the organic materials polyimide quartz and PBI. The ceramics are much more fragile than
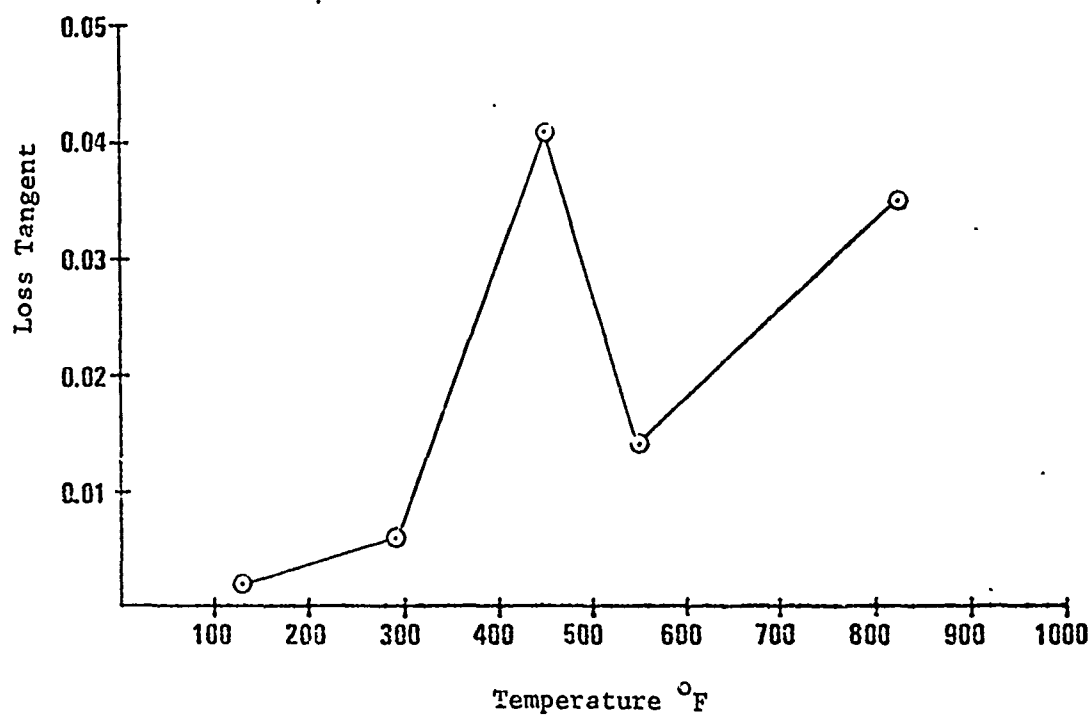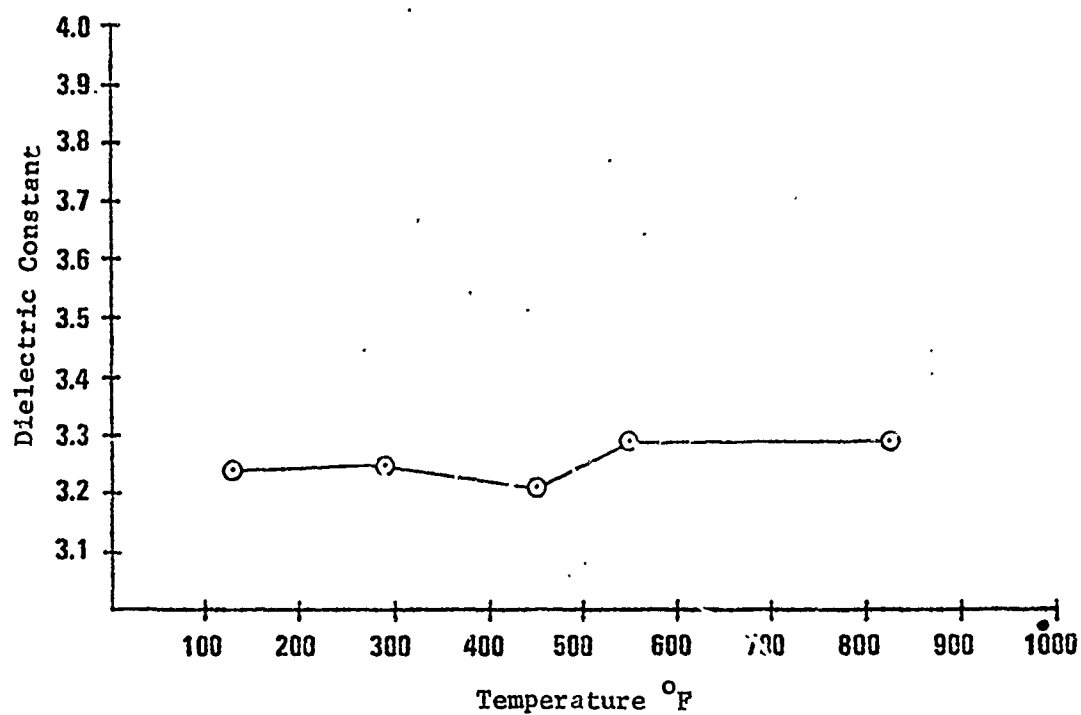
Figure 8. Dielectric Constant and Loss Tangent of Polyimide/Quartz
BPI-373 versus Temperature [3]

20
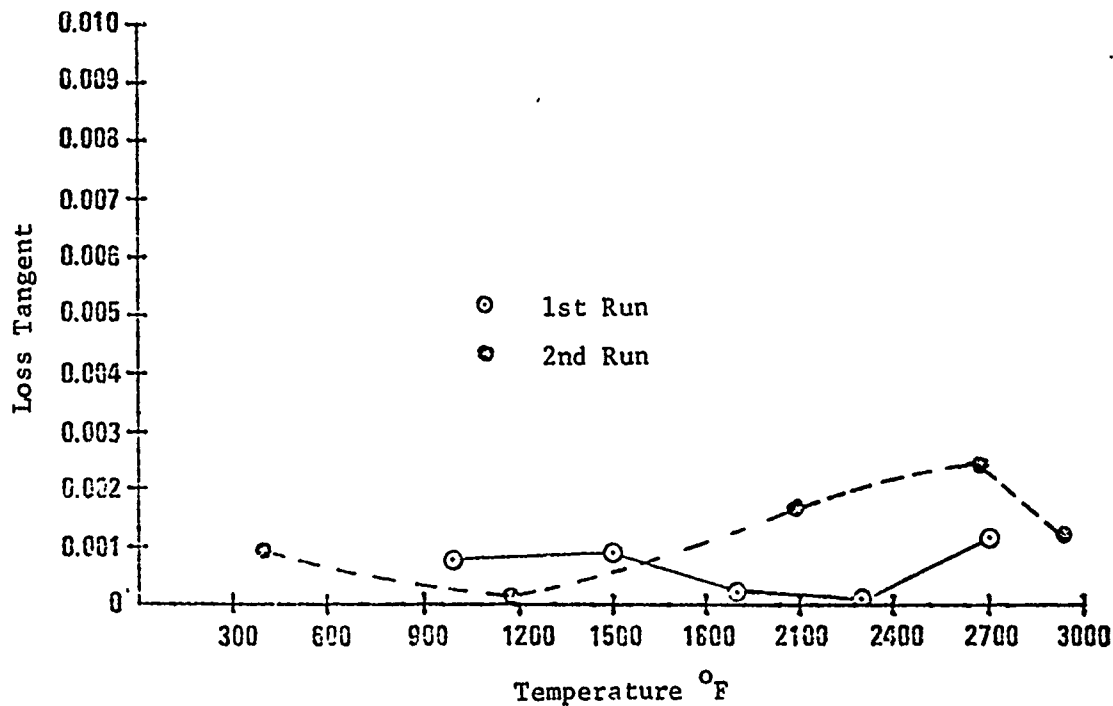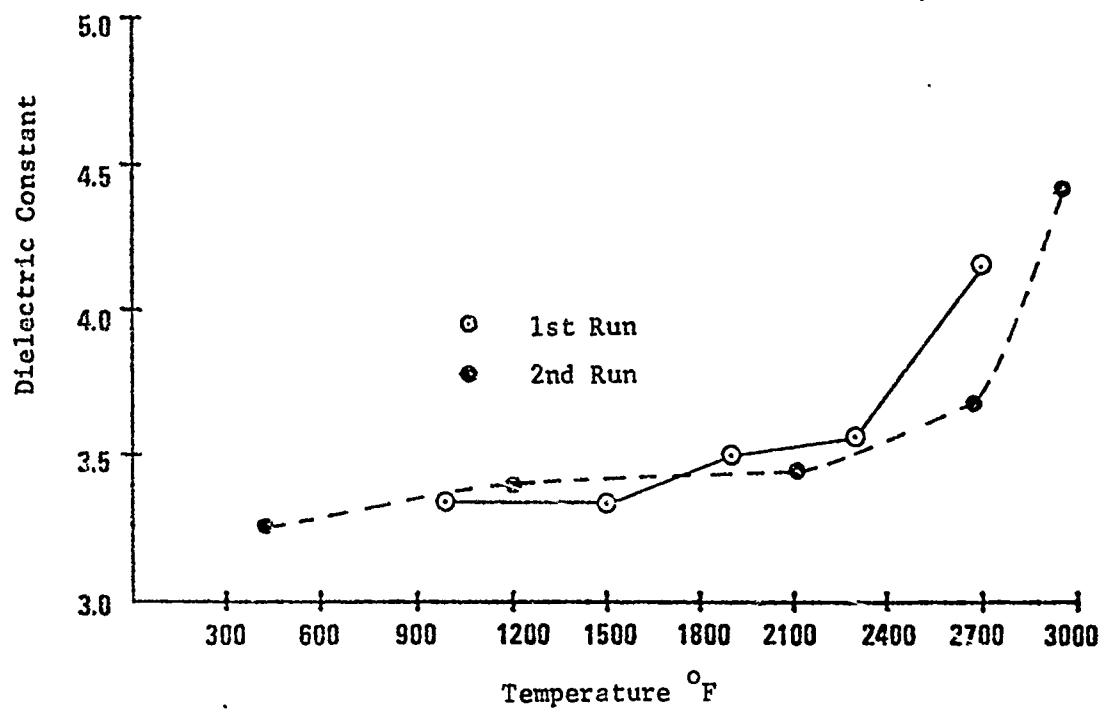
Figure 9. Dielectric Constant and Loss Tangent of SCFS versus Temperature [3]
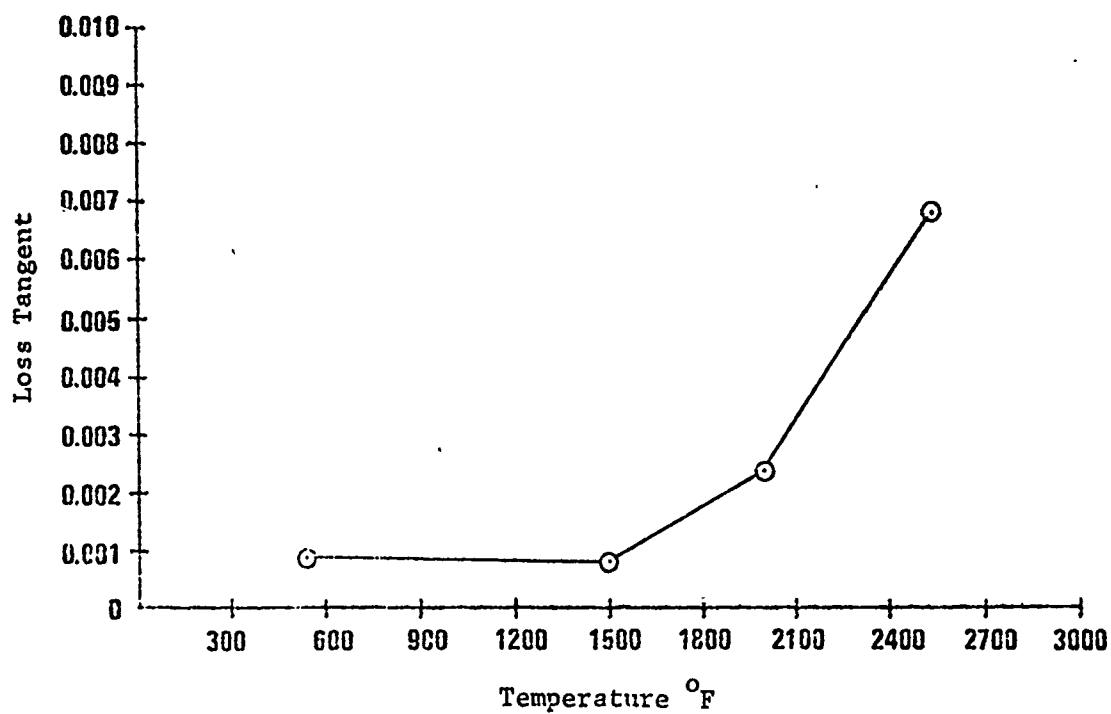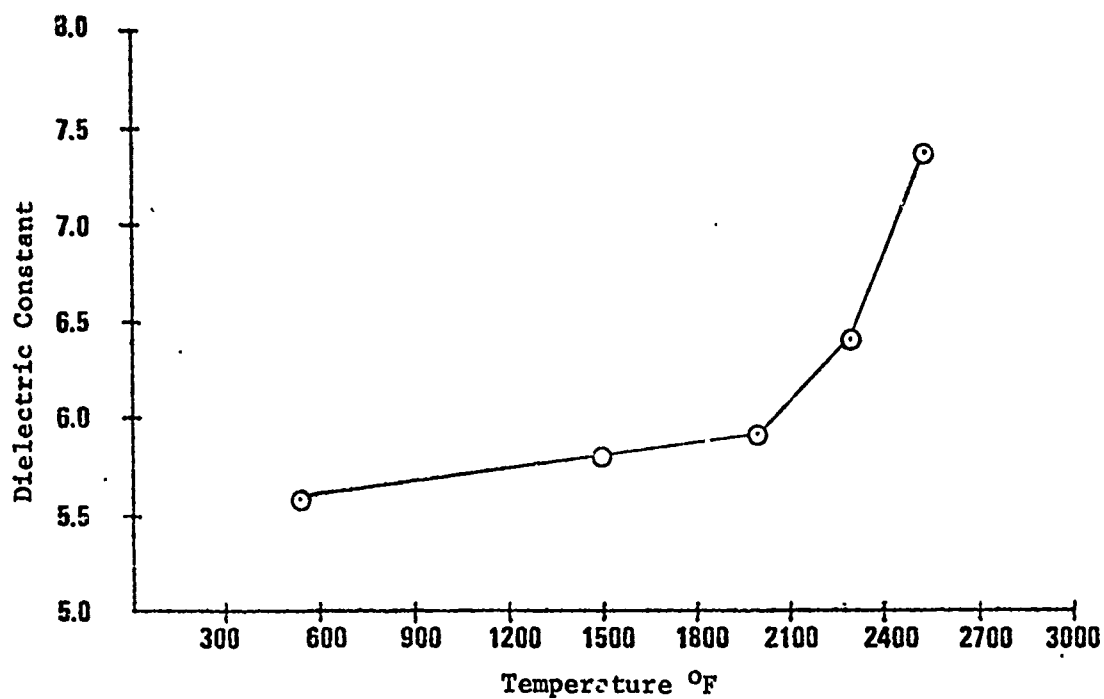
Figure 10. Dielectric Constant and Loss Tangent of Pyroceram® 9606 versus Temperature [3]

the organics; and if it is found that grinding of the ceramic is necessary to obtain a desired thickness, the organic design would be less expensive. The most desirable feature of Cordierite is its resistance to rain erosion. It will withstand rainfall conditions much better than the other materials. Slip-cast fused silica will absorb moisture and, although there are techniques to seal the radome, this adds to the overall cost.

In the next section, the effects of the radome shape and electrical properties of three radome materials on the electrical performance of the seeker system are presented. In the last section, a final choice of radome material and shape is made and presented.

SECTION IV

ELECTRICAL PERFORMANCE STUDY

1. Introduction

Electrical performance data for a number of candidate radome designs were determined analytically using the radome analysis computer program developed earlier and described in Reference 5. The radiating properties of the phase monopulse antenna were characterized using the plane wave spectrum representation of the near field of the antenna as described in 2c below. The important electrical performance parameters of the seeker system (boresight error, error slope, null depth, and power loss) were computed at three frequencies (8, 12, and 18 GHz) for three different radome materials (fused silica, polyimide,[1] and Pyroceram®) and for a number of fineness ratios (0.5 to 2.8) and antenna gimbal positions. Graphs of the electrical performance parameters of the antenna/radome combinations are presented in subsection 3 below and used in selecting an optimum radome design for the seeker system considered. The antenna/radome geometry, radome shape, electrical performance parameters, and antenna characterization are described in subsection 2 below.

2. Definitions of Input and Output Parameters

(a) Radome Shape

The radome shape considered is shown in Figure 11. The radome consists of a 5-inch outside diameter cylindrical section surmounted by a

---

[1] The polyimide referred to in Section IV is polyimide E-glass which has a relative dielectric constant of 3.8. PBI also has a relative dielectric constant of 3.8; thus the polyimide curves are representative of the PBI materials. Polyimide quartz has dielectric properties similar to slip-cast fused silica ($\rho = 1.95$ g/cc).

24
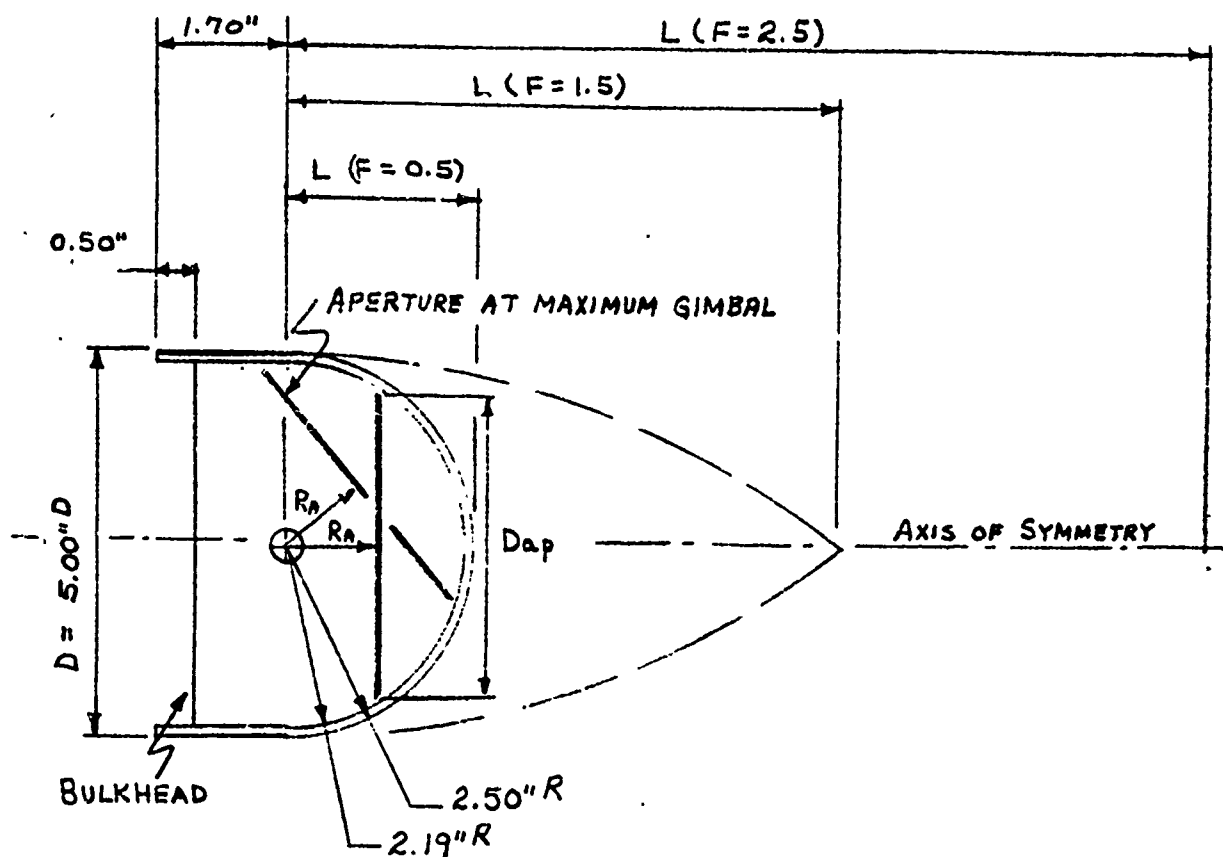
NOTE: ANTENNA APERTURE DIAMETER IS RELATED TO THE DISTANCE R_A BY THE
RELATION SHOWN.   IF R_A=1.20", THEN)=3.70".

Figure 11.   Antenna/Radome Geometry.

tangent ogive. Various degrees of streamlining of the radome are obtained

by varying the fineness ratio of the tangent ogive portion of the two-

section radome where the fineness ratio F is defined as the ratio of the

length L of the tangent ogive to its outside diameter D at a point P where

a tangent to the ogive shape is parallel to the axis of symmetry of the

radome; i.e., F = L/D. In Figure 11, the center of generation of the

tangent ogive is located at the gimbal point of the antenna so that such

a point P lies on the outer surface of the radome in the plane perpendicular

to the radome axis and containing the gimbal point. In the analysis, fine-

ness ratios of 0.5 (a hemisphere), 1.0, 1.5, 2.0, 2.5, and 2.8 were considered.

The location and orientation of the near-field aperture of the circu-

larly polarized, phase monopulse antenna are also shown in Figure 11. The

aperture is offset from the gimbal point by the distance R_A as shown. A

value of $R_A = 1.20$ inches was used in the analysis to conform to the dimen-

sions of an actual antenna system under consideration for this application.

The maximum diameter of the circular aperture which can fit inside the

radome is given by

$$D_{ap} = 2 \sqrt{\left(\frac{D}{2} - t_w\right)^2 - R_A^2} \tag{1}$$

where

D = Outside diameter of the radome

t_w = Thickness of the radome wall

R_A = Distance of the aperture from the gimbal point

The maximum wall thicknesses to consider follow from the equation defining

a n-order monolithic radome wall [6]; i.e.,

$$t_w = \frac{n\lambda o}{2\sqrt{\epsilon_r^2 - \sin^2\theta_d}} \tag{2}$$

26

where

$n = 1$ for half-wave wall

λ_o = Free-space wavelength

ϵ_r = Dielectric constant of wall material

θ_d = Design angle (60 degrees)

Using the dielectric constants of the three wall materials considered in Equation (2) at the (center) design frequency of 12 GHz results in the following wall thicknesses for first-order walls:

Material	ϵ_r	tan δ	t_w (inches)
Fused Silica	3.33	0.001	0.306
Polyimide	3.80	0.006	0.282
Pyroceram	5.20	0.001	0.233

From the above data it is clear that the material with the thickest wall is fused silica (polyimide quartz has dielectric properties similar to fused silica). Consequently, a maximum wall thickness of 0.31 inches was used in Equation (1) above to determine the diameter of the aperture. It is important to choose an aperture of maximum diameter as explained in subsection 2c below. (The loss tangents for the materials of interest are given in the above data for completeness; tan δ does not enter into the calculation of wall thickness.)

To complete the specification of the radome shape, it is necessary to include a radome base as shown in Figure 11 to represent the bulkhead where the radome is attached to the missile body. The orientation of the aperture inside the radome at the maximum gimbal angle considered is also shown in Figure 11.

27

(b) Antenna/Radome Orientation

The coordinate systems used to orient the antenna inside the radome are shown in Figure 12. These coordinate systems represent a specialization of the system defined in Reference 5 which explains why three systems of rectangular coordinates are used instead of just two.

The antenna coordinate system (x_A, y_A, z_A) is located in the reference system at $(x = 0, y = 0, z = R_A)$ and oriented as shown. The principal planes of the antenna radiation patterns are also defined in Figure 12 as the azimuth and elevation planes. For reference, the spherical coordinates of the origin O_A of the antenna system in the reference system are O_A : $(r_a = 1.20, \theta_a = 0°, \theta_a = 90°)$. The angle $\gamma_{3A} = 90°$ to bring the z and z_A axes into coincidence. The z_A - axis also coincides with the true electrical boresight direction of the antenna.

The orientation of the radome coordinate system (x_R, y_R, z_R) with respect to the reference system may be specified by the spherical coordinates of the origin O_R of the radome system. Note that the z_R - axis (and z_A) passes through the origin of the reference system which also coincides with the gimbal point inside the radome. For reference, O_R is located at $r_r = 1.20$ (inches) while ϕ_r and θ_r are varied to produce the required scanning of the antenna inside the radome to various look directions.

In order to simplify the specification of the antenna look direction, the angles ϕ_p and θ_L are defined as shown in Figure 12. These angles are related to ϕ_r, θ_r according to

$$\phi_r = \phi_p + 180° \tag{3}$$

$$\theta_r = 180° - \theta_L \tag{4}$$

When $\phi_p = 0$, $\theta_L = 0$, the axis of the radome coincides with the boresight direction of the antenna, and we say that the antenna is looking straight

28
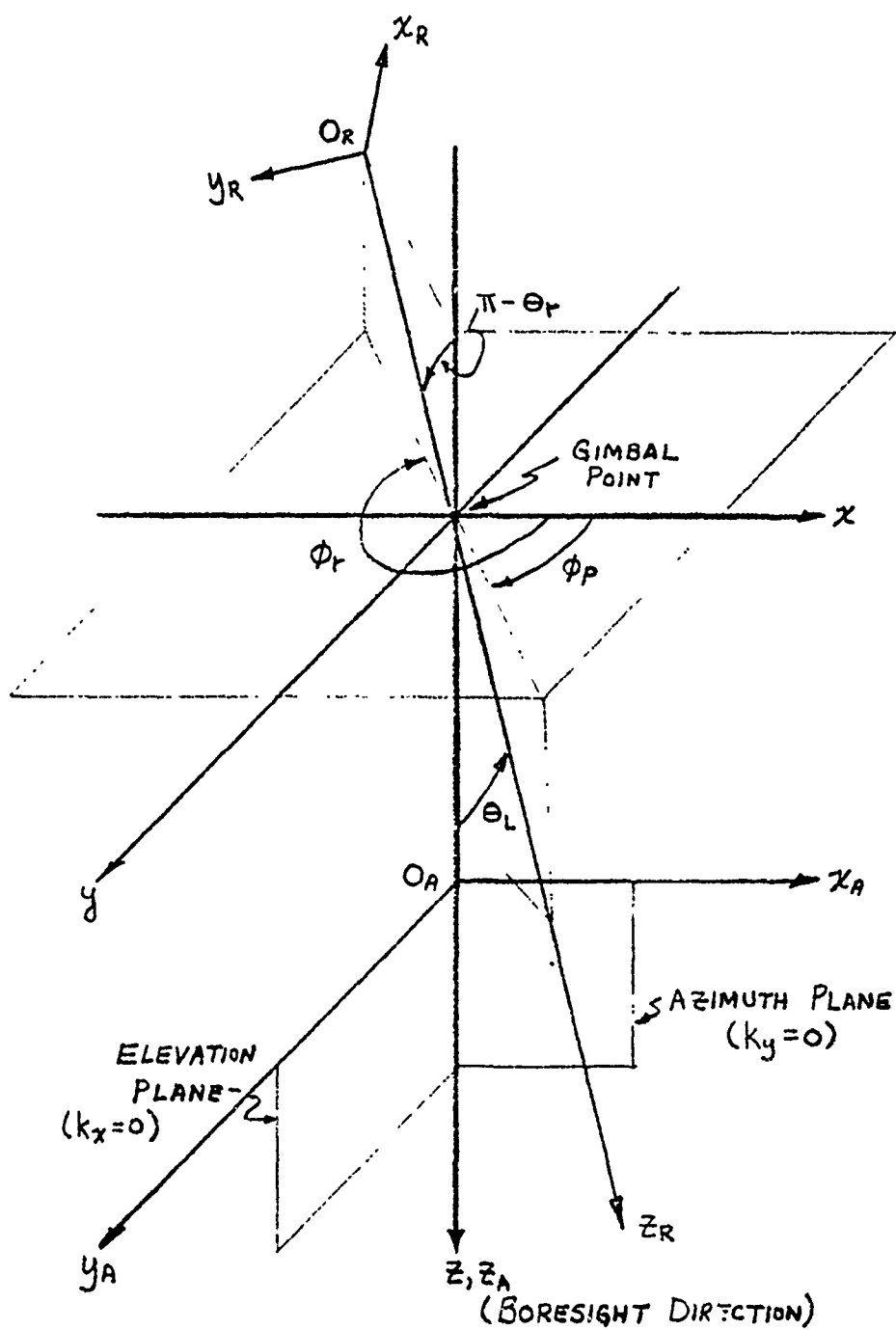
Figure 12. Coordinate Systems Used in Radome Analysis.
Reference System: (x, y, z)
Antenna System: (x_A, y_A, z_A)
Radome System: (x_R, y_R, z_R)

29

ahead. When $\phi_p = 0$ and $\theta_L > 0$, we say that the antenna is scanned in the azimuth plane (+ x_Z, z_A plane); when $\theta_L < 0$, the antenna is still scanned in the azimuth plane but in the opposite direction (- x_Z, z_A plane). Similar scan of the antenna in the elevation plane is accomplished by setting $\phi_p = 90°$ and varying θ_L. Any other plane of scan may be specified by setting ϕ_p while varying θ_L to produce the desired scan in that plane; e.g., when $\phi_p = 45°$, scan in the so-called crosstalk plane may be effected.

It is advantageous to note that identical effects will be produced in the antenna radiation patterns when scanned in either the azimuth or elevation planes because of symmetry in the radome and symmetry in the patterns of the antenna considered. For example, if the antenna is scanned in the azimuth plane, the azimuth pattern will be most affected, especially in boresight error. The same effects would be produced for scan in the elevation plane, with the roles of the azimuth and elevation principal planes being reversed. Note also that for scan in any given plane, the magnitudes of the effects will be the same for $+\theta_L$ as for $-\theta_L$. Consequently, it is necessary to consider scan of the antenna through only positive values of θ_L for any plane of scan specified by ϕ_p in order to determine the magnitudes of errors in the boresight direction, error slope, and so on. Furthermore, tests conducted using the radome analysis computer program showed that maximum errors occurred in the azimuth pattern for scan in the azimuth plane; hence, it was concluded that for the purposes of selecting the best radome design, scan of the antenna in only the azimuth plane need be considered. This finding greatly reduced the number of look directions required to produce representative data, resulting in substantial savings in computation time.

30

(c) Antenna Characterization

Ideally, the far-field radiation pattern of the antenna mounted in place, without radome, would be known in both amplitude and phase for two orthogonal components at each frequency and scan position of the antenna. Equally ideal would be the knowledge of the near field distribution of the antenna mounted in place, without radome, both in amplitude and phase for two orthogonal components of electric field at each frequency and scan position of the antenna. In most cases, however, this complete description is unavailable and some assumptions and approximations must be made. In the case at hand, the antenna to be used has not been designed, constructed or measured. It is known, however, that the antenna to be used should be circularly polarized and configured as a dual plane monopulse with sum, elevation plane difference and azimuth plane difference patterns. The pattern of the antenna should be frequency independent from 8 - 18 GHz and would probably use spirals as its main radiating elements. And finally, the antenna will be gimballed and must fit within a 5-inch outer diameter radome whose maximum wall thickness is 0.31 inch. What follows is a synthesis of a complex vector near-field distribution which meets these specifications under the assumption of no near field variation with antenna scan.

The far-field pattern of the antenna is specified in the antenna coordinate system of Figure 12. The far-field components are denoted $E_\theta(\theta,\phi,r)$, $E_\phi(\theta,\phi,r)$ and $E_r(\theta,\phi,r)$ where $E_r(\theta,\phi,r) = 0$ in the far field of any antenna of finite size. Also, in the far field, the dependence of the electric field components on r is of the form $1/r$ so that on a sphere of constant radius about the antenna, this term is a constant and will be

31

suppressed. With the above simplifications the far field of the antenna is composed of $E_\theta(\theta,\phi)$ and $E_\phi(\theta \cdot \phi)$.

Let us now define a complex polarization ratio as follows:

$$R(\theta,\phi) = \frac{E_\theta(\theta,\phi)}{E_\phi(\theta,\phi)} \tag{5}$$

Given that the polarization ratio has been specified for all angles (θ,ϕ) let us now calculate the relationship between $E_x(\theta,\phi)$ abd $E_y(\theta,\phi)$ in the far field as these are the components that will relate to the near-field components which we ultimately want to determine.

It is well known that the $E_x(\theta,\phi)$ and $E_y(\theta,\phi)$ components of the far-field may be written in terms of $E_\theta(\theta,\phi)$ and $E_\phi(\theta \cdot \phi)$ under the assumption that $E_r(\theta,\phi)=0$ as follows:

$$E_x(\theta,\phi) = E_\theta(\theta,\phi) \cos\theta \cos\phi - E_\phi(\theta,\phi) \sin\phi \tag{6}$$

$$E_y(\theta,\phi) = E_\theta(\theta,\phi) \cos\theta \sin\phi + E_\phi(\theta,\phi) \cos\phi \tag{7}$$

Incorporating Equation (5) into Equations (6) and (7) and dividing Equation (6) by Equation (4) yields:

$$\frac{E_x(\theta,\phi)}{E_y(\theta,\phi)} = \frac{R(\theta,\phi) \cos\theta \cos\phi - \sin\phi}{R(\theta,\phi) \cos\theta \sin\phi + \cos\phi} \tag{8}$$

Thus it is seen that the polarization ratio $R(\theta,\phi)$ also determines the ratio between $E_x(\theta,\phi)$ and $E_y(\theta,\phi)$ for all angles (θ,ϕ). It is convenient to change the (θ,ϕ) coordinate used in Equation (8) to normalize wavenumbers coordinates (k_x,k_y). The normalized wavenumbers k_x, k_y and k_z are defined as follows:

$$k_x = \sin\theta \cos\phi \tag{9}$$

$$k_y = \sin\theta \sin\phi \tag{10}$$

$$k_z = \cos\theta \tag{11}$$

$$k_x^2 + k_y^2 + k_z^2 = 1 \tag{12}$$

32

From these Equations the following useful relationships may be derived:

$$\sin\theta = \sqrt{k_x^2 + k_y^2} \tag{13}$$

$$\cos\theta = \sqrt{1 - k_x^2 - k_y^2} \tag{14}$$

$$\sin\phi = \frac{k_y}{\sqrt{k_x^2 + k_y^2}} \tag{15}$$

$$\cos\phi = \frac{k_x}{\sqrt{k_x^2 + k_y^2}} \tag{16}$$

Substituting Equations (13) through (16) into Equation (8) yields:

$$M(k_x,k_y) = \frac{E_x(k_x,k_y)}{E_y(k_x,k_y)} = \frac{R(k_x,k_y)\sqrt{1 - k_x^2 - k_y^2}\; k_x - k_y}{R(k_x,k_y)\sqrt{1 - k_x^2 - k_y^2}\; k_y - k_x} \tag{17}$$

For the case at hand, the polarization ratio, $R(k_x,k_y)$, is equal to $j(=\sqrt{-1})$ for all angles (k_x,k_y); i.e., the radiation is circularly polarized.

The power pattern of an antenna may be specified as

$$P(k_x,k_y) = \frac{E_x^*(k_x,k_y)\,E_x(k_x,k_y) + E_y^*(k_x,k_y)\,E_y(k_x,k_y) + E_z^*(k_x,k_y)\,E_z(k_x,k_y)}{\eta} \tag{18}$$

where η is the intrinsic impedance of free space in ohms and * denotes complex conjugate. At each point of the far field, the field is a plane wave for which

$$\vec{k} \cdot \vec{E} = 0$$

33

Equation (19) may be expanded and $E_z(k_x, k_y)$ may be determined as a function of $E_x(k_x, k_y)$ and $E_y(k_x, k_y)$ as follows:

$$E_z(k_x, k_y) = \frac{-1}{k_z} \left[k_x E_x(k_x, k_y) + k_y E_y(k_x, k_y) \right] \tag{20}$$

Substituting Equation (20) into Equation (18), the far-field power pattern may be determined as a function of $E_x(k_x, k_y)$ and $E_y(k_x, k_y)$ as follows:

$$P(k_x, k_y) = \frac{E_x^*(k_x, k_y) E_x(k_x, k_y)}{\eta} \left[1 + \frac{k_x^2}{k_z^2} \right] + \frac{E_y^*(k_x, k_y) E_y(k_x, k_y)}{\eta} \left[1 + \frac{k_y^2}{k_z^2} \right] \cdot$$

$$+ \frac{E_x^*(k_x, k_y) E_y(k_x, k_y) + E_y^*(k_x, k_y) E_x(k_x, k_y)}{\eta} \left[\frac{k_x - k_y}{k_z^2} \right] \tag{21}$$

Let us digress to show three relationships for arbitrary complex numbers. Let $c = a + jb$ and $d = e + jf$ be arbitrary complex numbers where a, b, e, and f are real. Then

$$c*c = (a - jb)(a + jb) = a^2 + b^2, \text{ a real number} \tag{22}$$

$$c+c* = (a + jb) + (a - jb) = 2a, \text{ a real number} \tag{23}$$

$$c*d + d*c = (a - jb)(e + jf) + (e - jf)(a + jb) \tag{24}$$

$$= ae + jaf - jbe + bf + ae + jbe - jfa + bf$$

$$= 2 (ae + be), \text{ a real number}$$

Using Equation (24) we see that the last term of Equation (21) is real and thus the whole right hand side of Equation (21) is real as it should be for real power flow. Substituting Equation (17) into Equation (21) yields

$$P(k_x, k_y) = \frac{E_y^*(k_x, k_y) E_y(k_x, k_y)}{\eta} \left[\left(\frac{1}{1 - k_x^2 - k_y^2} \right) (M^*(k_x, k_y) M(k_x, k_y)(1-k_y^2) \right.$$

$$\left. + (1 - k_x^2) + (M^*(k_x, k_y) + M(k_x, k_y)(k_x, k_y)) \right] \tag{25}$$

34

where $k_z^2 = 1 - k_x^2 - k_y^2$ from Equation (12) has been used.

Defining the factor of Equation (25) in brackets to be $B(k_x,k_y)$, Equation (25) becomes

$$P(k_x,k_y) = \frac{E_y^*(k_x,k_y)\ E_y(k_x,k_y)}{\eta}\left[B(k_x,k_y)\right] \tag{26}$$

where from Equations (22) through (24), $B(k_x,k_y)$ is seen to be real.

$P(k_x,k_y)$ may be written as a product of conjugates as:

$$P(k_x,k_y) = A^*(k_x,k_y)\ A(k_x,k_y) \tag{27}$$

Thus we may associate the factors in Equation (26) with those in Equation (27) as

$$A^*(k_x,k_y)\ A(k_x,k_y) = \left[\frac{E_y(k_x,k_y)}{\sqrt{\eta}}\ B(k_x,k_y)\right]^*\ \left[\frac{E_y(k_x,k_y)}{\sqrt{\eta}}\ B(k_x,k_y)\right] \tag{28}$$

Solving for $E_y(k_x,k_y)$ yields

$$E_y(k_x,k_y) = \sqrt{\eta}\ \frac{A(k_x,k_y)}{\sqrt{B(k_x,k_y)}} \tag{29}$$

$E_x(k_x,k_y)$ may then be found from Equation (17) as

$$E_x(k_x,k_y) = M(k_x,k_y)\ E_y(k_x,k_y) \tag{30}$$

Unfortunately there is no unique way to accomplish the separation of the power pattern as indicated in Equation (27). One way to accomplish this however, is to let $A(k_x,k_y)$ be the complex far-field component of the $E_y(x \cdot y)$ component of a first-guess near-field distribution which has characteristics similar to the specified antenna except that it has only a $E_y(x \cdot y)$ component. Such characteristics might include spatial limitations and spatial variations which are characteristic of antennas in the class under consideration. Using the resultant far-field component

35

$A(k_x, k_y)$, E_x and E_y in the far field may be determined from Equations (29) and (30). The near field of the antenna may then be calculated from the well known inverse Fourier transform as follows:

$$E_{xnf}(x,y) = \frac{FT^{-1}\left[E_x(k_x,k_y)\right]}{\dfrac{jk_z e^{-j\vec{k}\cdot\vec{r}}}{r}} \tag{31}$$

$$E_{ynf}(x,y) = \frac{FT^{-1}\left[E_x(k_x,k_y)\right]}{\dfrac{jk_z e^{-j\vec{k}\cdot\vec{r}}}{r}} \tag{32}$$

where FT^{-1} is the inverse Fourier transform operation and $E_{xnf}(x,y)$ and $E_{ynf}(x,y)$ are the x and y components of the near field distribution, respectively.

The procedure developed above allows one to determine $E_x(x,y)$ and $E_{ynf}(x,y)$ near field distributions which produce a far field which is circularly polarized (i.e. for the case $R(\theta,\phi) = j$) everywhere in the far field. Also the near field distribution has spatial characteristics which meet the specifications the class of antennas under consideration.

The choice of the first-guess near-field distribution represents a compromise between a four-spiral antenna and a frequency independent antenna. The resultant is an expanding four-spiral phase monopulse antenna. The four spirals are located at the corners of a square and touch each other. The center of each spiral moves radially outward and each spiral expands inversely with frequency and directly with wavelength. Each spiral has a diameter of approximately 1.23λ at all operating frequencies.

36

The size of the spirals was limited by the space limitations within the radome at 8 GHz, the low end of the frequency band. The electric field distribution for each spiral is identical, except for phasing, and is symmetric about the axis of the spiral. The field on each spiral had a radial cosine distribution with zero field in the center and peak field near the edge of the spiral.

After readjustment through the use of Equations (29) through (32) the resulting near field distributions produced the sum, elevation difference and azimuth difference far-field patterns shown in Figures 13, 14, and 15, respectively. Tests showed that the cross polarization component of each of these fields (the opposite sense circular) was no greater than 30 db below the primary component of these fields throughout the entire far-field power patterns. As the near-field distributions had constant wavelength dimensions at all operating frequencies, the far-field power patterns did not change over the specified band.

(d) Output Parameters

The parameters chosen to characterize the electrical performance of the antenna/radome combination were boresight errors in the azimuth and elevation planes, monopulse error slope in these two planes, the depths of the difference pattern nulls, and the power loss in the 3-db contour of the sum pattern. For a given set of input parameters, the radome analysis computer program was used to calculate the sum power pattern SUM (k_x, k_y), the azimuth difference power pattern $DAZ(k_x, k_y)$, and the elevation difference power pattern $DEL(k_x, k_y)$. The output parameters are then calculated from these power patterns as described in what follows.
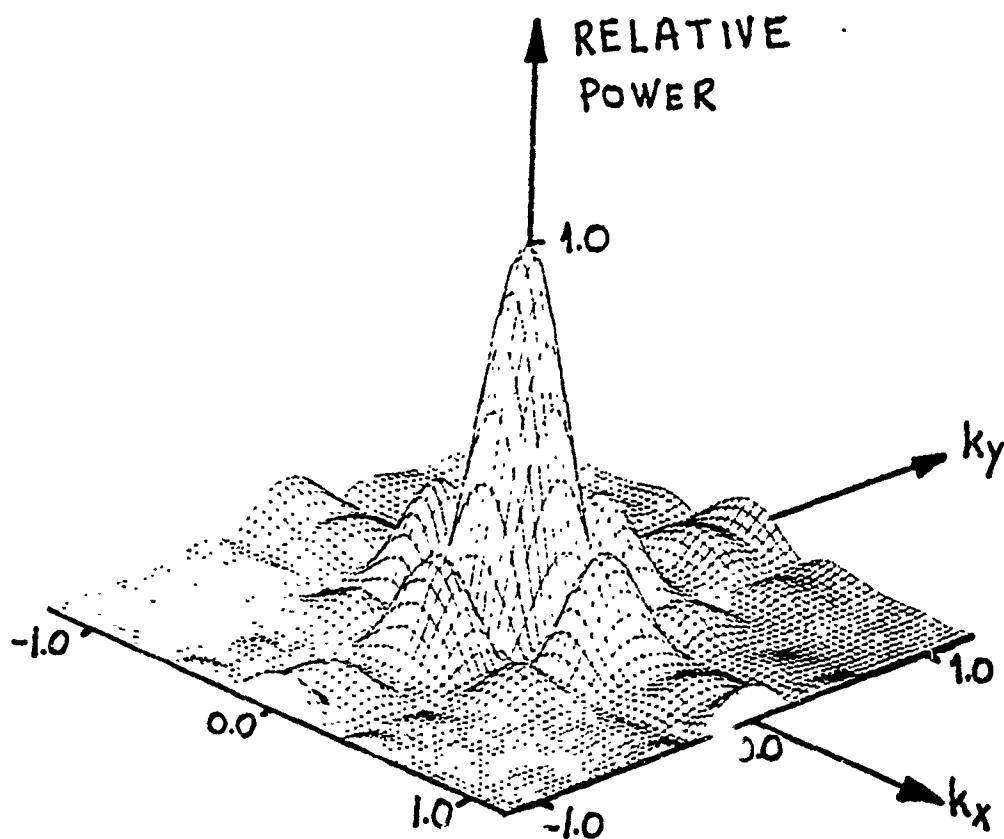
37

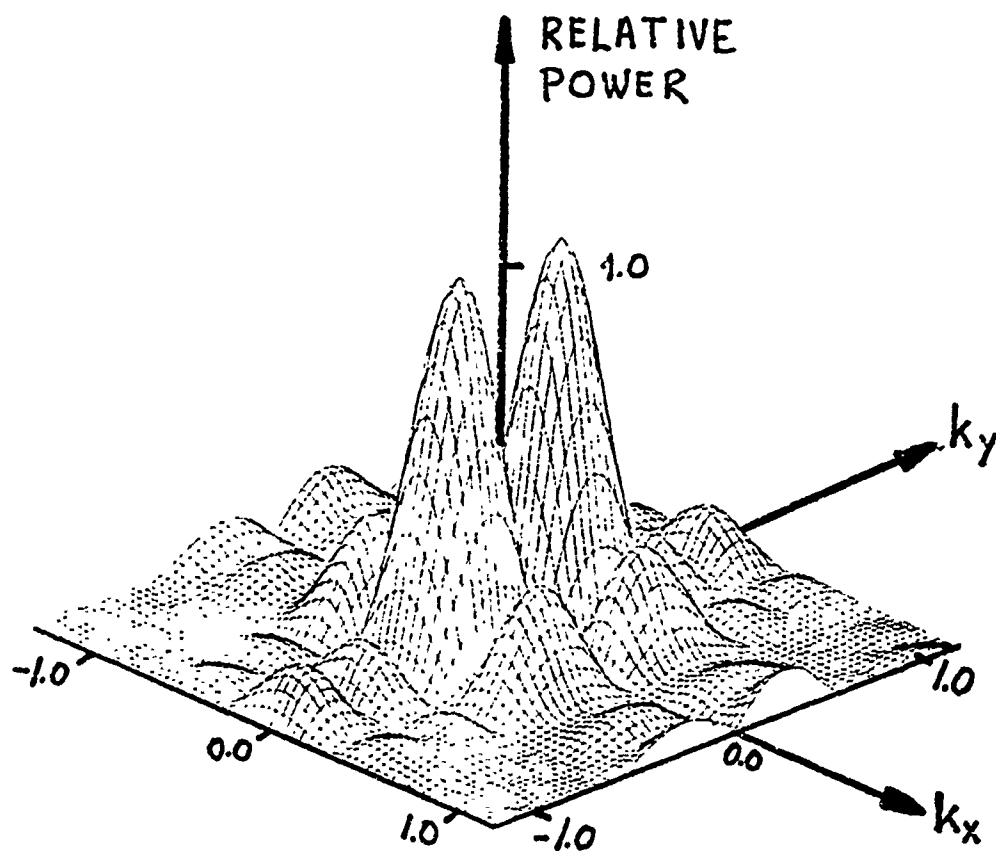Figure 13.   Far Field Power Pattern of Antenna in
Sum Mode

Figure 14. Far Field Power Pattern of Antenna in
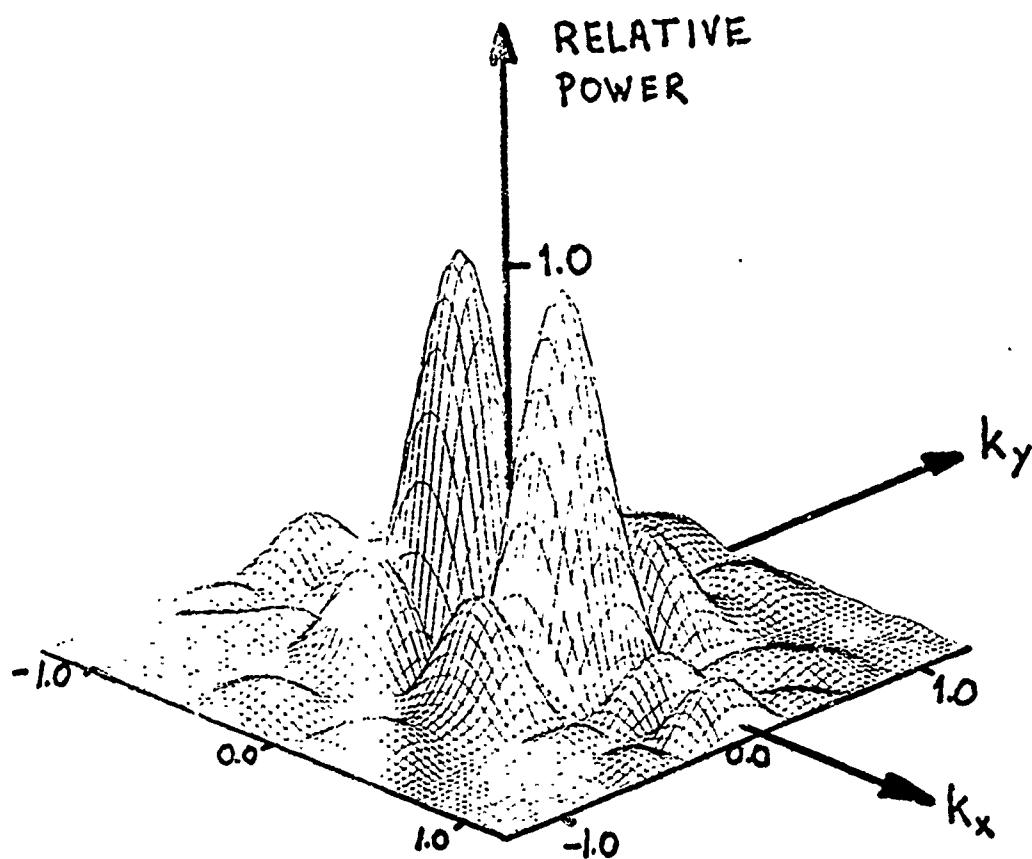Elevation Difference Mode

Figure 15. Far Field Power Pattern of Antenna in
Azimuth Difference Mode

The boresight error in the azimuth plane is found by first forming the ratio

$$RAZ(k_x) = \sqrt{\frac{DAZ(k_x,0)}{SUM(k_x,0)}} \qquad (33)$$

and then converting to decibels

$$RAZDB(k_x) = 20 \log RAZ. \qquad (34)$$

The square root is taken to convert the power patterns to voltage patterns. Setting $k_y = 0$ in Equation (33) has the effect of restricting attention to the azimuth plane defined in Figure 12. The discrete value of k_x for which $RAX(k_x)$ is a minimum is then found by a point-by-point com------n of the values of $RAX(k_x)$ in the vicinity of $k_x = 0$. (The true bor-   · ? cection is at $k_x = 0$, $k_y = 0$; the effect of the radome is to cau& :   1 errors in the electrical boresight direction.) Since the va--- uf k_x found may not coincide with exact null position, parabolic interpolation (using three points on each side of the minimum point) is used to find the exact null position in wavenumber coordinates; viz., KXNULL. A similar procedure is used with $DEL(k_x,k_y)$ to find the null position KYNULL in the elevation plane ($k_x = 0$). The boresight errors are then given in milli-radians by

$$BSEAZ = Sin^{-1}(KXNULL) \cdot 1000 \qquad (35)$$

$$BSEEL = Sin^{-1}(KYNULL) \cdot 1000 \qquad (36)$$

where the sense of the error is described by the following:

BSEAZ $< \Rightarrow \phi = \pi$ plane (Figure 12)

BSEAZ $> \Rightarrow \phi = 0$ plane (Figure 12)

41

$$\text{BSEEL} < 0 \Rightarrow \phi = \frac{3\pi}{2} \quad \text{plane (Figure 12)}$$

$$\text{LSEEL} > 0 \Rightarrow \phi = \frac{\pi}{2} \quad \text{plane (Figure 12)}$$

The monopulse error slope in azimuth, ESLPAZ, is defined by

$$\text{ESLPAZ} = \frac{d}{dk_x} \left[\text{RAZ}(k_x) \right] \, k_x = \text{KXNULL} \tag{37}$$

Since the derivative changes signs on either side of the null, the slope is actually found on both sides of the null and an average is taken of the two magnitudes. In the actual calculations, $\text{RAZDB}(k_x)$ is used so that the error slope in volts per degree is given by

$$\text{ESLPAZ} = \frac{\text{Antilog (NULLDB)}}{20 \log e} \left[\frac{d}{dk_x} \left(\frac{\text{RAZDB}(k_x^+) - \text{RAZDB}(k_x^-)}{2} \right) \right] \tag{38}$$

$$k_x$$

where

$$\text{NULLDB} = \text{RAZDB (KXNULL)}$$

$$e = \text{Eulers constant}$$

and where k_x^+, k_x^- indicate that the derivatives are taken on either side of the null. The depth of the null is just NULLDB. A similar procedure is carried out for these parameters in the elevation plane.

The final output parameter is the power loss in the 3-dB contour of the sum pattern. This loss is defined by

$$\text{PLOSS} \triangleq - 10 \log \left(\frac{\text{P3DBR}}{\text{P3DBO}} \right) \tag{39}$$

where

P3DBR = Power in 3-dB contour of sum pattern with radome in place

P3DBO = Power in 3-dB contour of sum pattern without radome

The 3-dB contour is the half-power contour on a sphere for the sum power pattern. The power calculated is that received by a circularly polarized

42

antenna when the seeker antenna transmits the sum pattern. The parameter PLOSS is an indication of the reduction in gain of the seeker antenna due to inner radome reflection, losses in the radome wall, distortions of the radiation pattern, and depolarization of the circularly polarized waves radiated by the seeker antenna as caused by the radome.

3.   Computed Electrical Performance

The results of the computer analysis have been plotted and are presented in this section. The plots are grouped into two main divisions: The first division consists of plots of the boresight error in milliradians, the monopulse error slope in millivolts per degree, the power loss in decibels and the depth of the difference null in decibels of the far field pattern with radome in place, all as a function of the look angle of the antenna within the radome. These plots are repeated for various candidate radome materials and fineness ratios at three frequencies. The second group of plots are principle plane cuts of a polyimide radome-enclosed antenna operating in the sum mode, the azimuth difference mode and the elevation difference mode. These plots are repeated for two fineness ratios and for three frequencies.

The first group of plots are presented in order to determine which radome material is electrically superior and which fineness ratio is optimum. Far-field patterns were calculated for fused silica, polyimide and Pyroceram radomes with fineness ratios of 0.5, 1.5, and 2.5 at 8 GHz, 12 GHz, and 18 GHz. All plots are a function of the look angle of the antenna with respect to the radome where zero degree look angle corresponds to the tip of the radome. Figure 16 is a graph of the boresight error produced by the fused silica radome for look angles from zero degrees

to 35 degrees. Also on this figure is a graph of the monopulse error slope with a fused silica radome in place. Both of these graphs contain three sets of data; one for a radome of fineness ratio equal to 0.5, one for a radome of fineness ratio equal to 1.5 and one for a radome of fineness ratio of 2.5, all operating at a frequency of 8 GHz. As expected, the boresight error for a fineness ratio of 0.5 (a hemisphere) is zero and the error slope is constant for the various look angles. The boresight error is seen to be greatest for a fineness ratio of 1.5 and returns to lower values for a fineness ratio of 2.5. Graphs to be displayed later for a polyimide quartz radome show this variation in boresight error in more detail for intermediate fineness ratios. The error slope is seen to be a weak function of fineness ratio and look angle and, as shown later for polyimide, is only severe in the tip region. Figure 17 contains the graphs for power loss and null depth for a fuzed silica radome at 8 GHz for fineness ratios of 0.5, 1.5, and 2.5. The power loss is seen to monotonically increase with fineness ratio and monotonically decrease with look angle. The graph of null depth shows that the null tends to fill in almost monotonically with look angle. Actually, it will be seen later that the null depth values peak at a look angle of approximately 20 degrees. This look angle corresponds to the peak of one of the two difference pattern main lobes passing through the tip region of the radome. The 0.5 fineness ratio null depth is the lowest and remains constant with look angle, as expected. Figure 18 and 19 are repetitions of Figures 16 and 17 but at a frequency of 12 GHz, the design frequency. The 12 GHz behavior is very similar to the 8 GHz behavior for the boresight error, the monopulse error slope and the null depth, but the losses for all fineness ratios at 12 GHz are very low. Figures 20 and 21

44

are repetitions of Figure 16 and 17 but for a frequency of 18 GHz. Small differences can be seen, but the overall performance is very similar to the 8 GHz case. Figures 22 through 27 are similar to Figures 17 through 21 except that the material is polyimide instead of fused silica. All of the polyimide graphs contain data for six fineness ratios: 0.5, 1.0, 1.5, 2.0, 2.5, and 2.8. Also, the look angle of zero degrees is included as well as additional look angles of 12.5 degrees, 17.5 degrees, and, on some graphs, 40 degrees. Figure 22 shows that the boresight error can be minimized at two fineness ratios. A fineness ratio of 0.5 is ideal with zero boresight error for all look angles. Second best is a fineness ratio of 2.5 since this fineness ratio produces the least boresight error of the non-hemispherical fineness ratios. The error slope graph shows that the error slope increases with fineness ratio in the tip region. This increase in error slope is probably due to the attenuation as a function of look angle which would lower the gain of the difference pattern in the null region. Figure 23 shows that radome losses for polyimide can become quite severe in the tip region for large fineness ratios. The null depth graphs show a pronounced peak as a difference pattern main lobe passes through the tip of the radome at a look angle of approximately 20 degrees. The remaining figures for polyimide at 12 GHz and 18 GHz are very similar to those for fused silica but are given in more detail. Figures 28 through 33 are repetitions of Figure 16 through 21 except that the material is Pyroceram.[6] Pyroceram is seen to produce characteristics very similar to fused silica and polyimide.

Two conclusions may be reached concerning the three materials tested. First, there is no dramatic difference between materials with regard to boresight error, error slope or null depth. Second, the losses for fused

silica and polyimide are approximately the same whereas the loss for Pyro-, ceram is a few decibels higher.

Two conclusions regarding the best fineness ratio can be reached. First, the fineness ratio of 0.5 is clearly the best electrically. Second, the next-best fineness ratio is 2.5, for as can be seen from the boresight error graphs, the boresight error becomes very large for fineness ratios of 1.0 and 1.5 then decreases to a minimum at 2.5 and then increases again for larger ratios.

The second group of plots contains principal plane patterns for a polyimide radome-enclosed antenna. The patterns are for various look angles and for two fineness ratios. Figures 34 through 39 are exceptions to the rule; these are principal plane patterns for an "air" radome (no radome at all). Figure 34 is the azimuth plane slice of the far-field sum and azimuth difference patterns. The sum pattern is normalized to zero decibels with a peak at zero degrees azimuth. The difference pattern is normalized to the sum pattern with resulting main lobes of approximately -3 dB at ±20 degrees in azimuth. Figure 35 is the elevation plane slice of the far-field sum and elevation difference patterns. These patterns are seen to be identical to the previous figure for the azimuth plane. This symmetry exists as the antenna is symmetric and the "air" radome is symmetric. Figures 36 and 37 are the same as Figures 34 and 35 except that the frequency is now 12 GHz. The 12 GHz patterns are the same as the 8 GHz patterns since the antenna is frequency independent and so is the "air" radome. Figures 38 and 39 are repetitions of Figures 34 and 35 for 18 GHz and are also the same as the 8 GHz patterns. Figures 40 and 41 are the 8 GHz patterns, Figures 42 and 43 are the 12 GHz patterns and Figures 44 and 45 are the 18 GHz patterns for a polyimide radome with fineness ratio of 2.5 at a look angle of zero degrees

46

in azimuth and zero degrees in elevation. In these figures, the azimuth

plane patterns are seen to be the same as the elevation plane patterns

since the radome is symmetric for this look angle.

It is noted that the losses are significant at 8 and 18 GHz and low

at 12 GHz. Figures 46 through 51 are the 8, 12, and 198 GHz patterns for

the polyimide radome with fineness ratio of 2.5 at a look angle of 17.5

degrees in azimuth and zero degrees in elevation. Figures 46 and 47 are

typical of these patterns and show the asymmetry of the two principal

planes since the radome is not symmetric at this look angle. The most

significant feature of these figures is the rise of the difference pattern

null in the azimuth plane. Figures 42 through 57 show the same radome with

the same fineness ratio for a look angle of 40 degrees in azimuth and 0

degrees in elevation. Figures 58 through 63 are the patterns for a look

angle of 17.5 degrees in azimuth and 17.5 degrees in elevation. The sequence

of figures from Figure 64 to Figure 87 are a repetition of Figures 40 through

63 except that the fineness ratio is 0.5 (a hemisphere). The significant

feature of the hemispherical radome is that no distortion of the patterns

occur for any look angle. The only feature displayed is the constant losses

at 8 and 18 GHz.
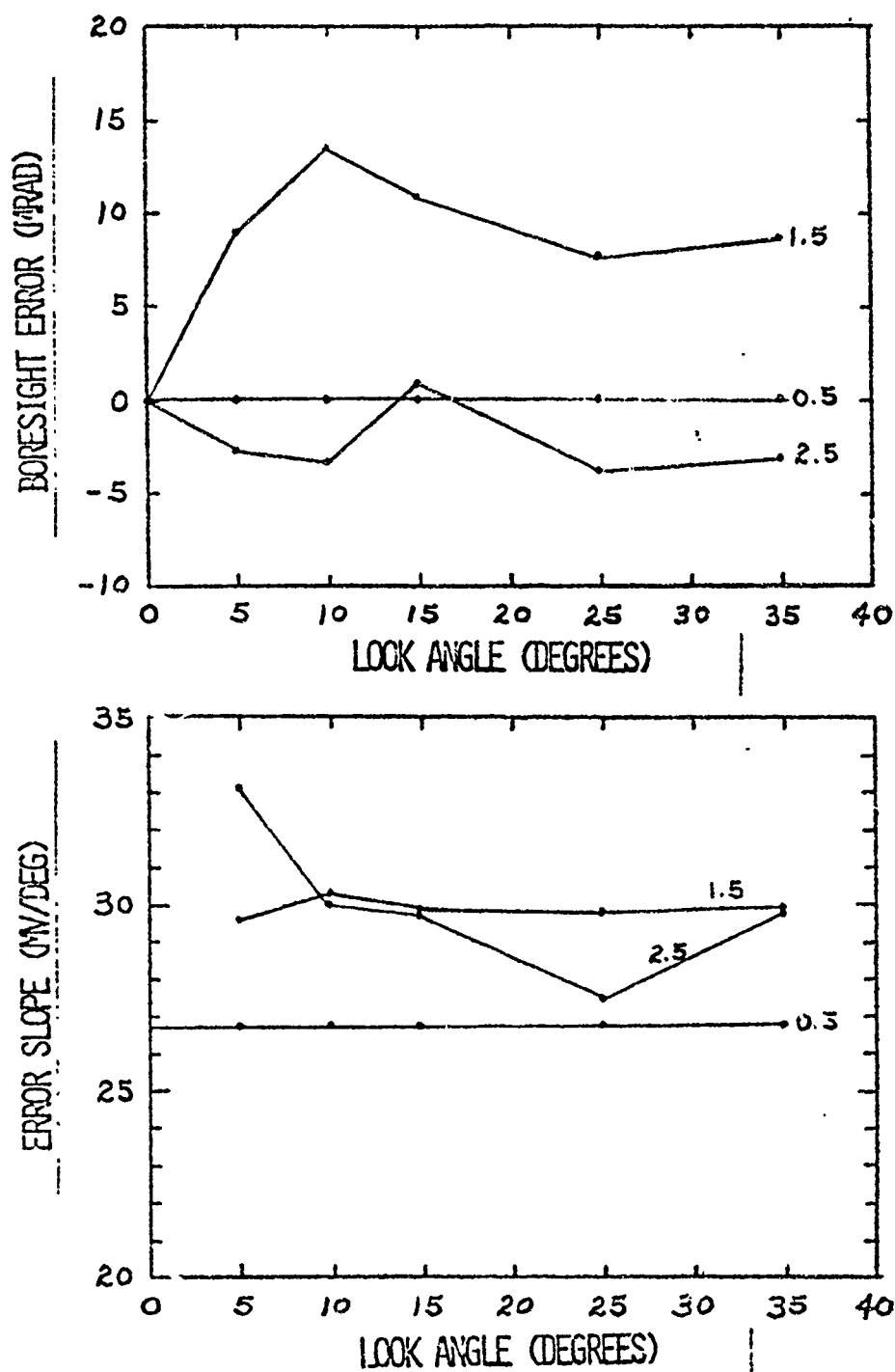
FIGURE 5. BORESIGHT ERROR AND MONOPULSE ERROR SLOPE VERSUS LOOK
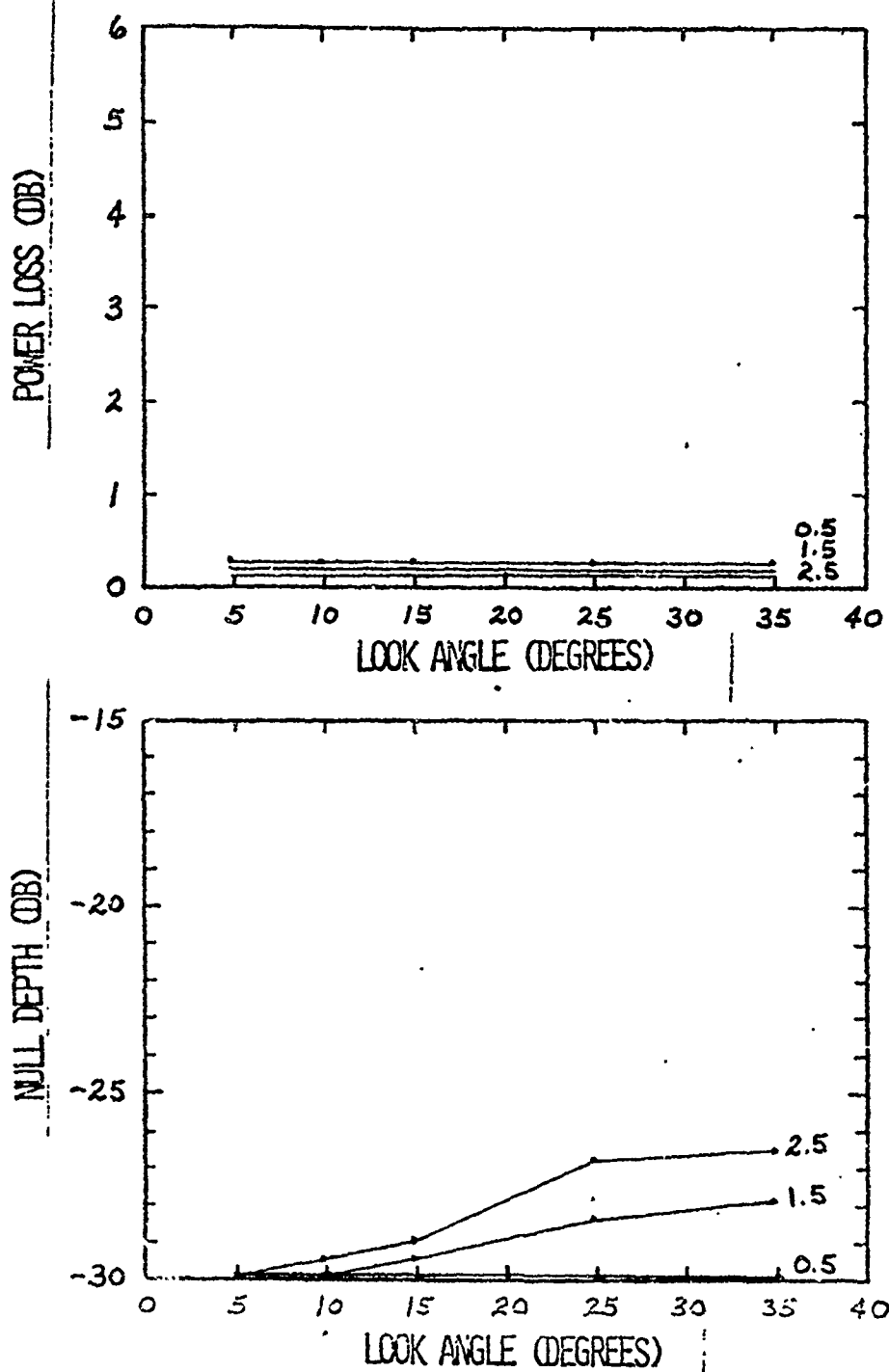ANGLE AND FINENESS RATIO FOR FUSED SILICA AT 8 GHZ.
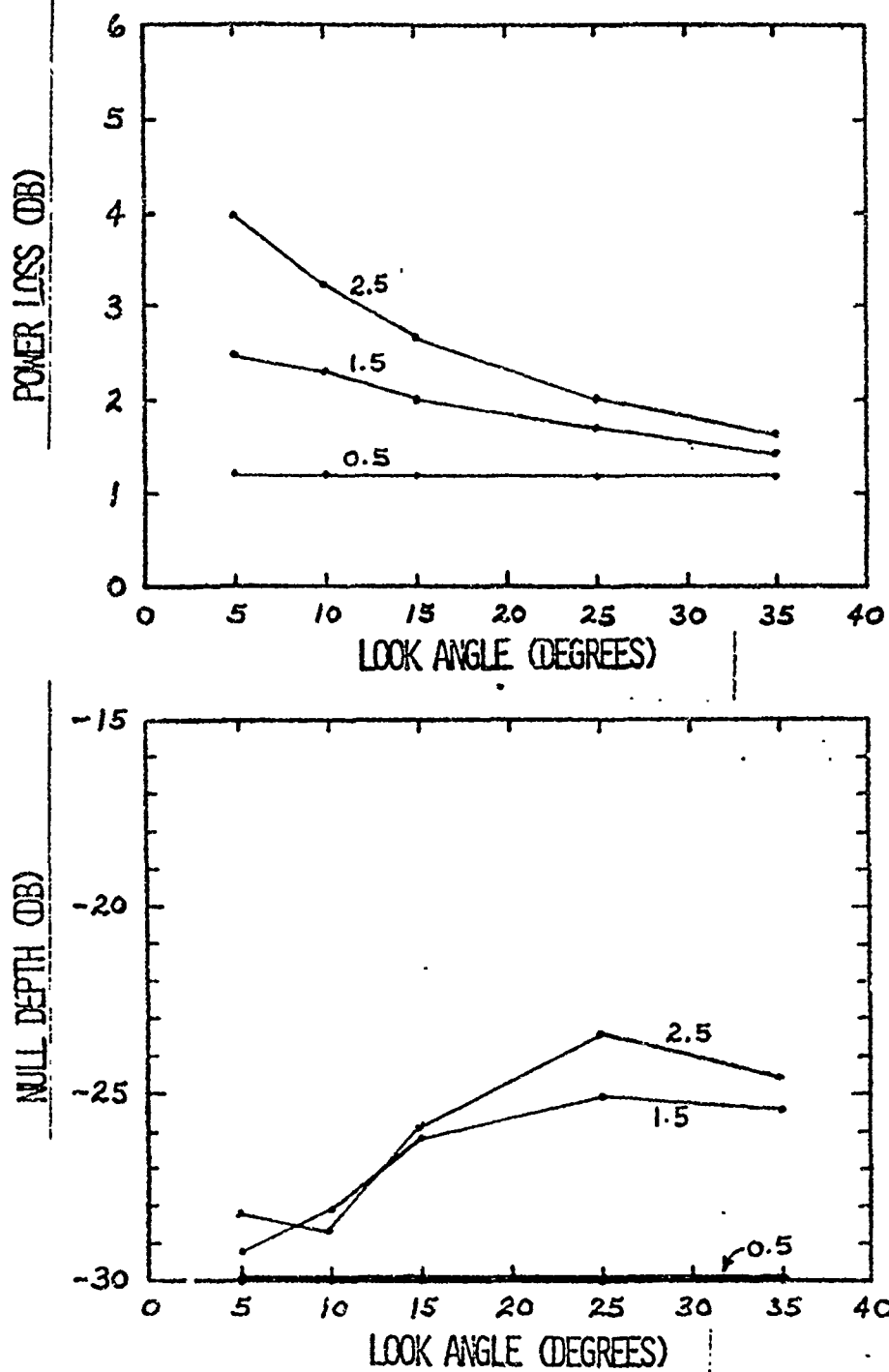
FIGURE 17. POWER LOSS IN 3 DB CONTOUR OF SUM PATTERN AND NULL
DEPTH OF MONOPULSE RATIO VERSUS LOOK ANGLE AND
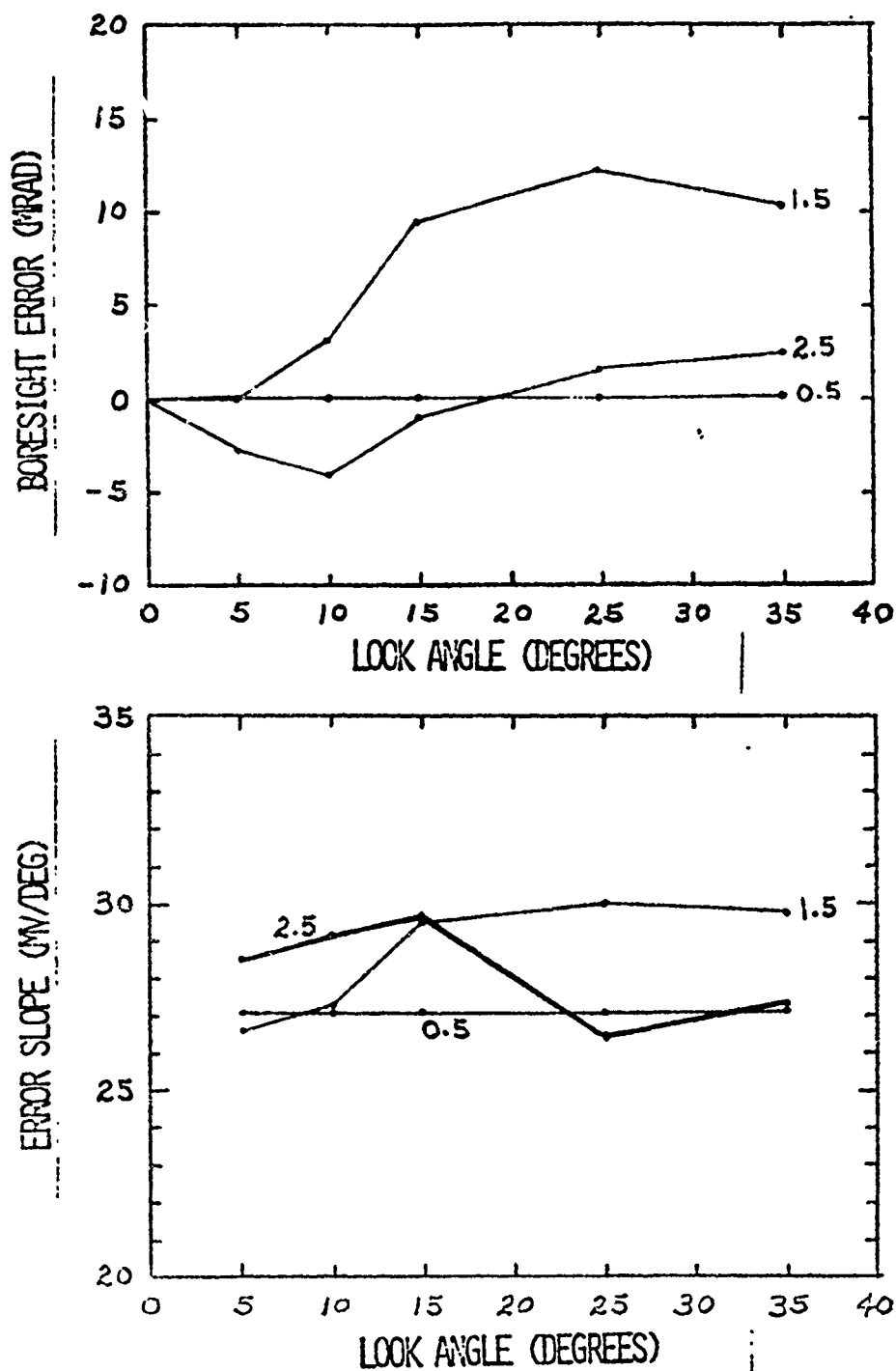FINENESS RATIO FOR FUSED SILICA AT 8 GHZ.

49
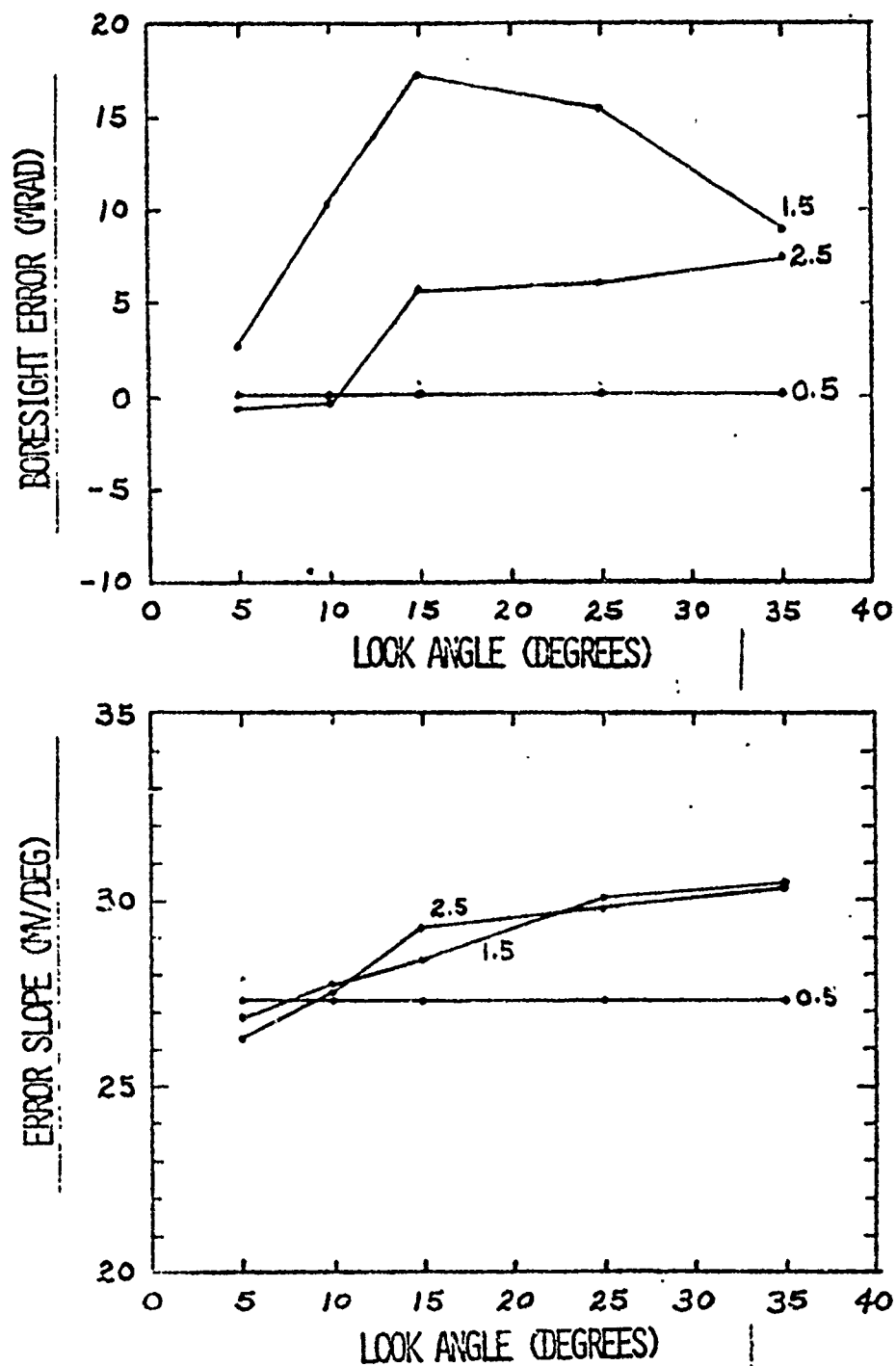
FIGURE 18. BORESIGHT ERROR AND MONOPULSE ERROR SLOPE VERSUS LOOK ANGLE AND FINENESS RATIO FOR FUSED SILICA AT 12 GHZ.
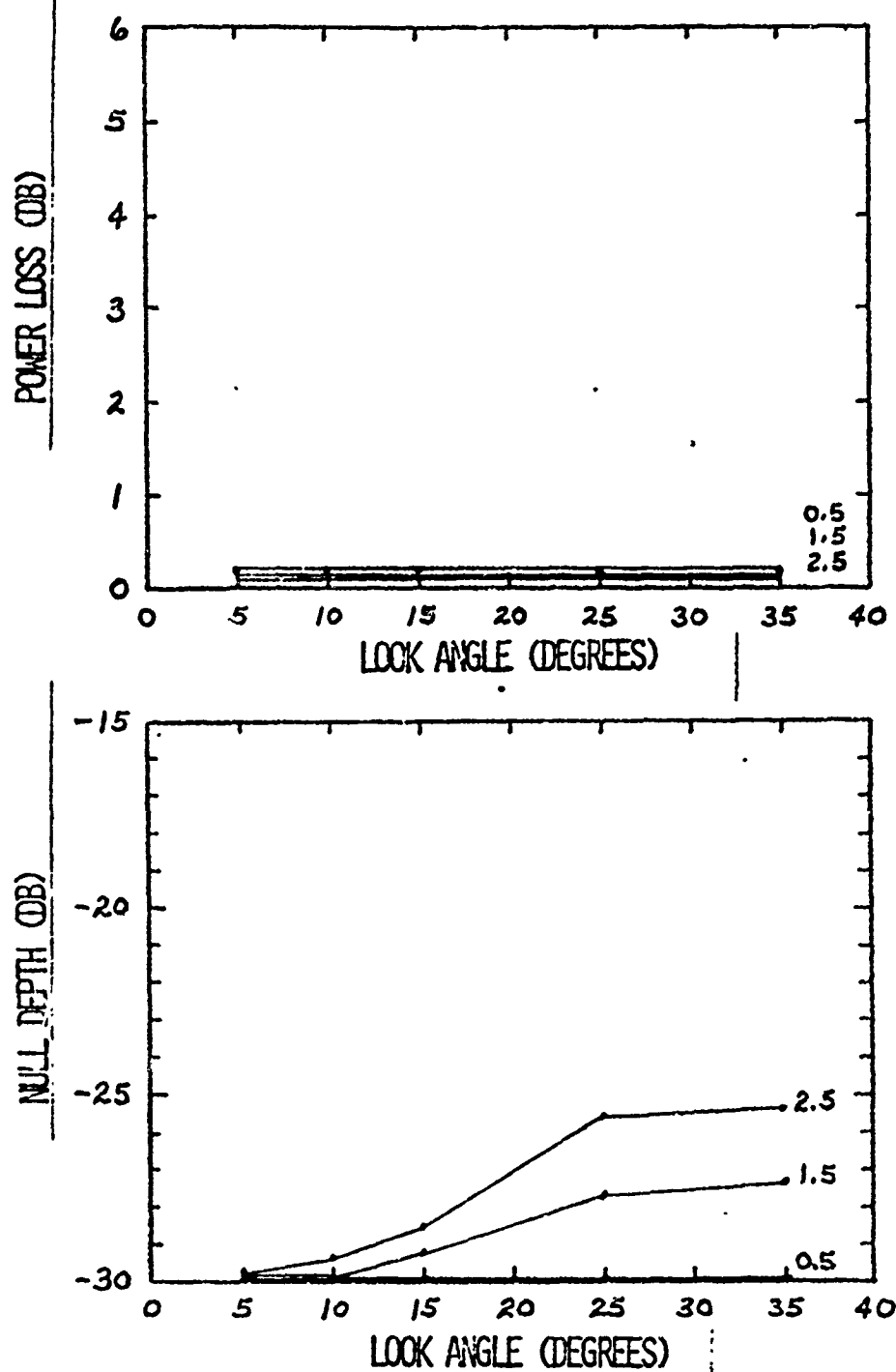
FIGURE 19. POWER LOSS IN 3 DB CONTOUR OF SUM PATTERN AND NULL
DEPTH OF MONOPULSE RATIO VERSUS LOOK ANGLE AND
FINENESS RATIO FOR FUSED SILICA AT 12 GHZ.

51
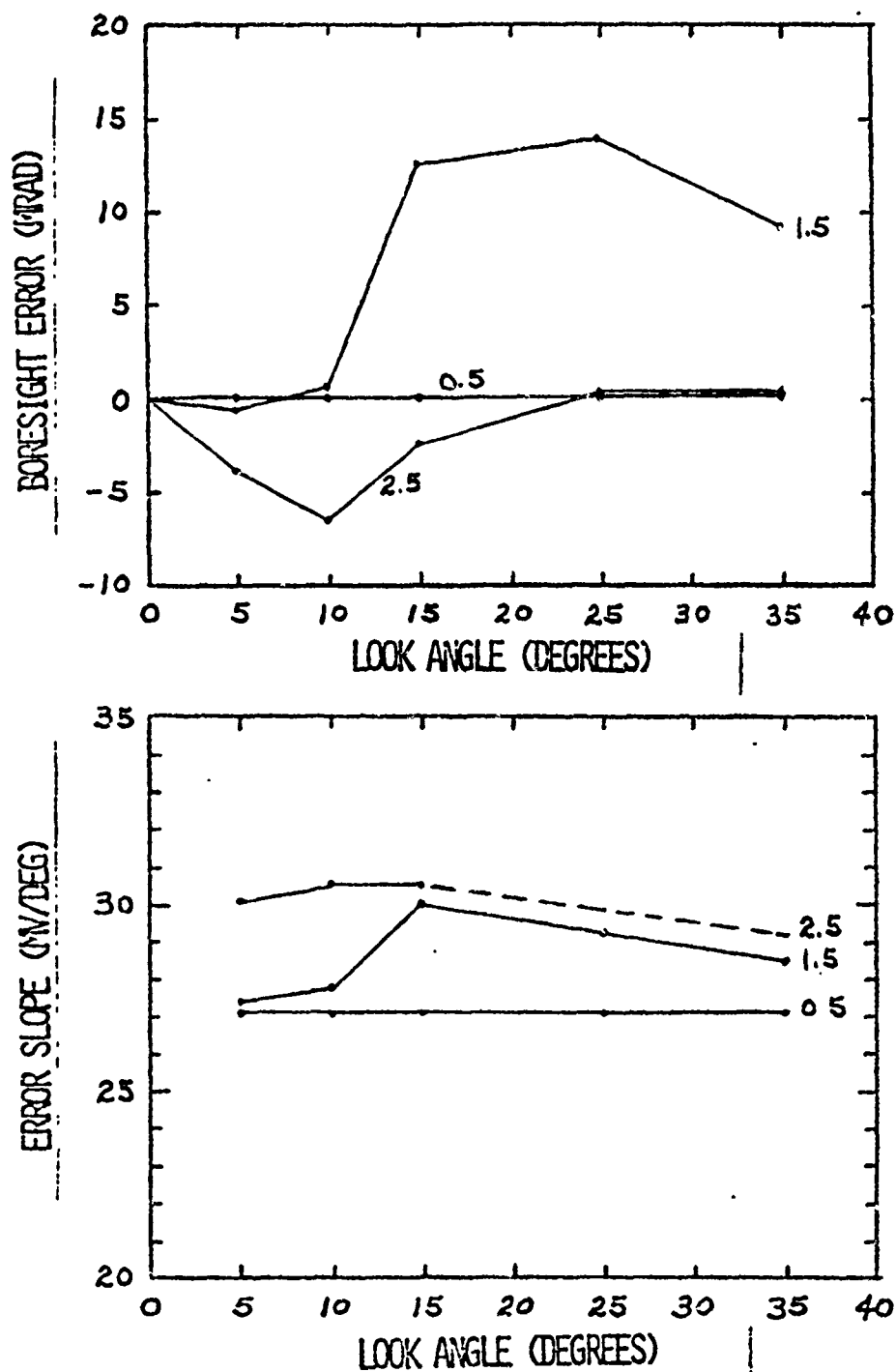
FIGURE 20. BORESIGHT ERROR AND MONOPULSE ERROR SLOPE VERSUS LOOK
ANGLE AND FINENESS RATIO FOR FUSED SILICA AT 18 GHZ.
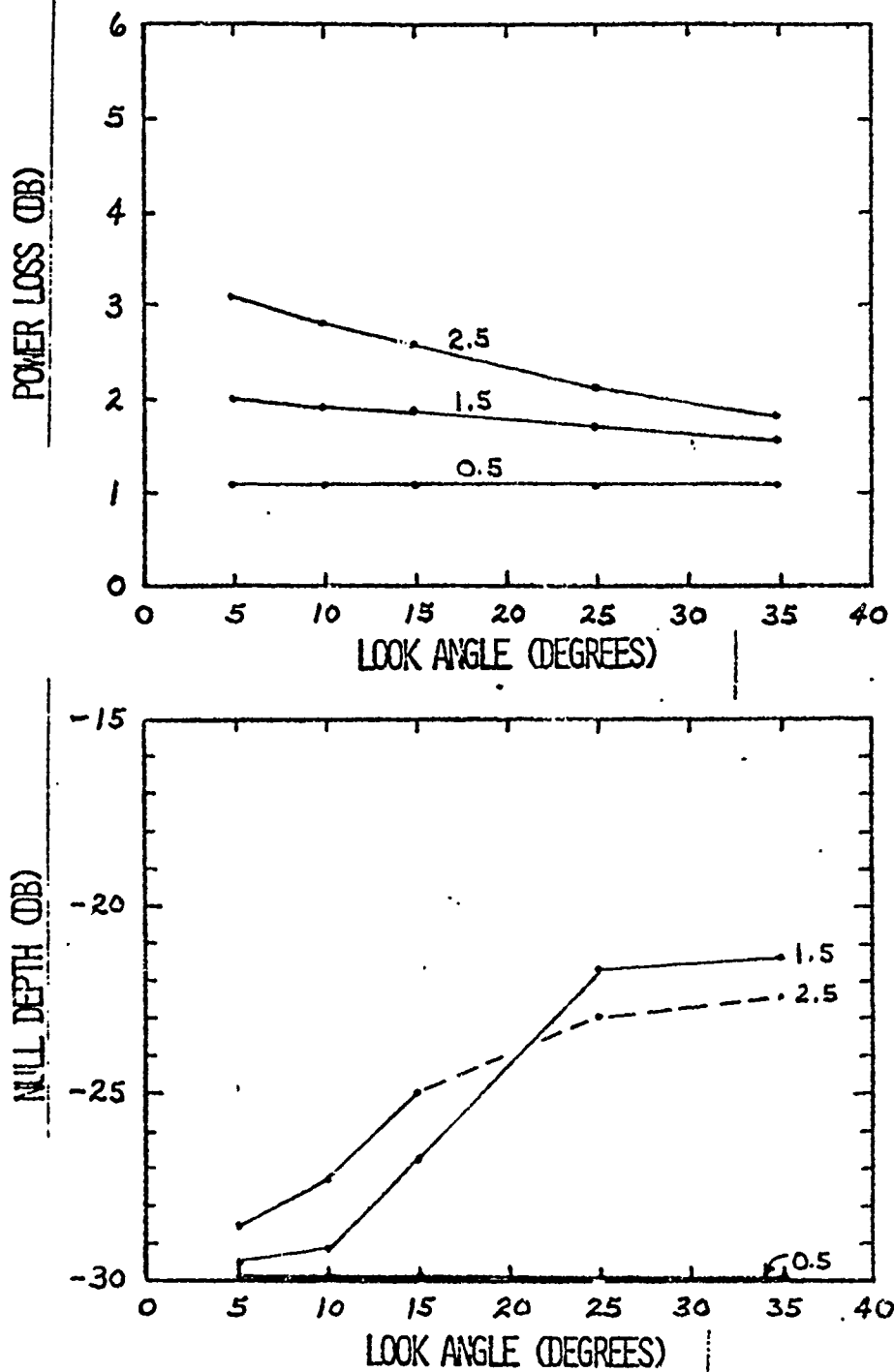
FIGURE 21. POWER LOSS IN 3 DB CONTOUR OF SUM PATTERN AND NULL
DEPTH OF MONOPULSE RATIO VERSUS LOOK ANGLE AND
FINENESS RATIO FOR FUSED SILICA AT 18 GHZ.
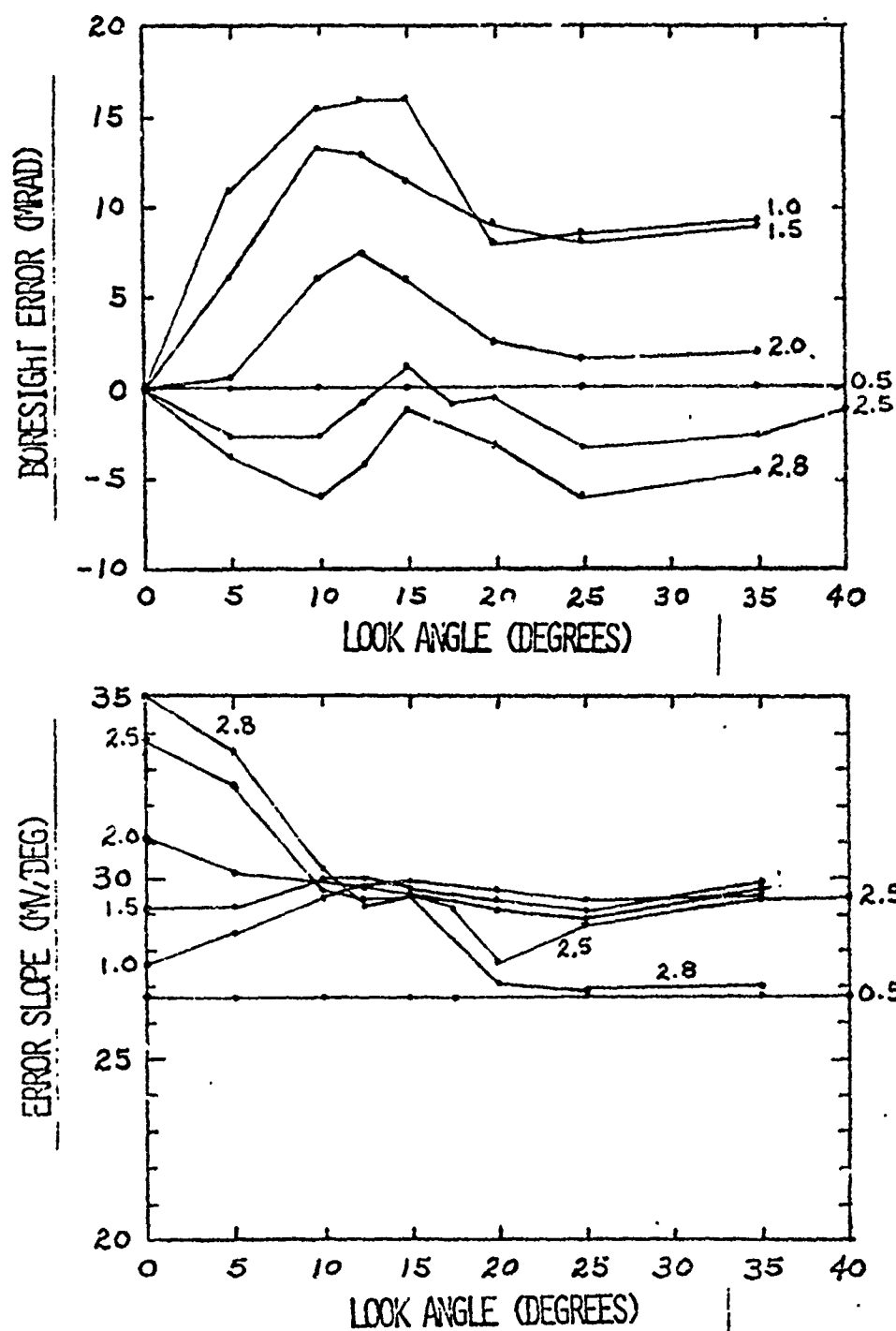
FIGURE 22. BORESIGHT ERROR AND MONOPULSE ERROR SLOPE VERSUS LOOK ANGLE AND FINENESS RATIO FOR POLYIMIDE AT 8 GHZ.
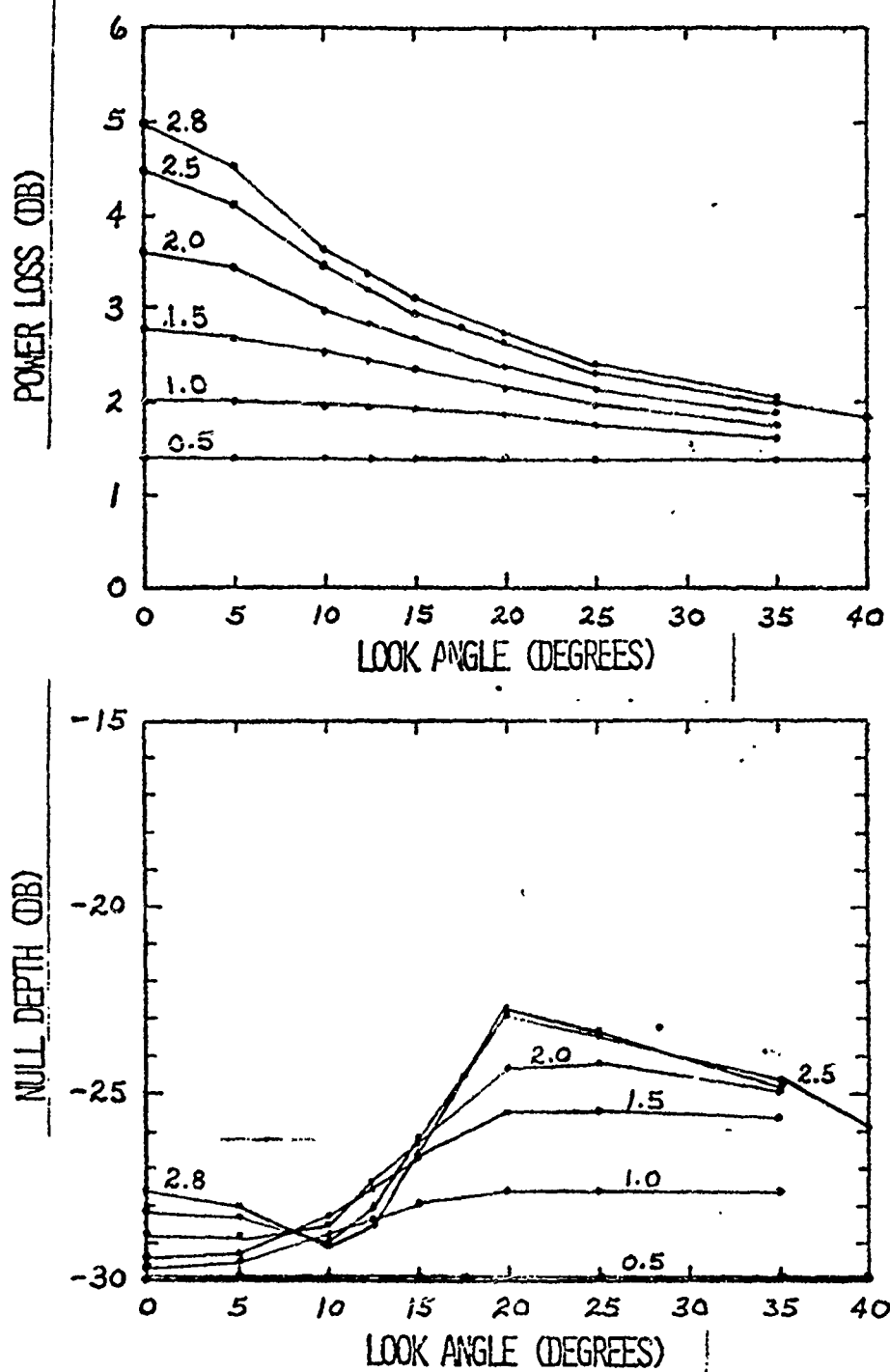
FIGURE 23. POWER LOSS IN 3 DB CONTOUR OF SUM PATTERN AND NULL
DEPTH OF MONOPULSE RATIO VERSUS LOOK ANGLE AND
FINENESS RATIO FOR POLYIMIDE AT 8 GHZ.

55
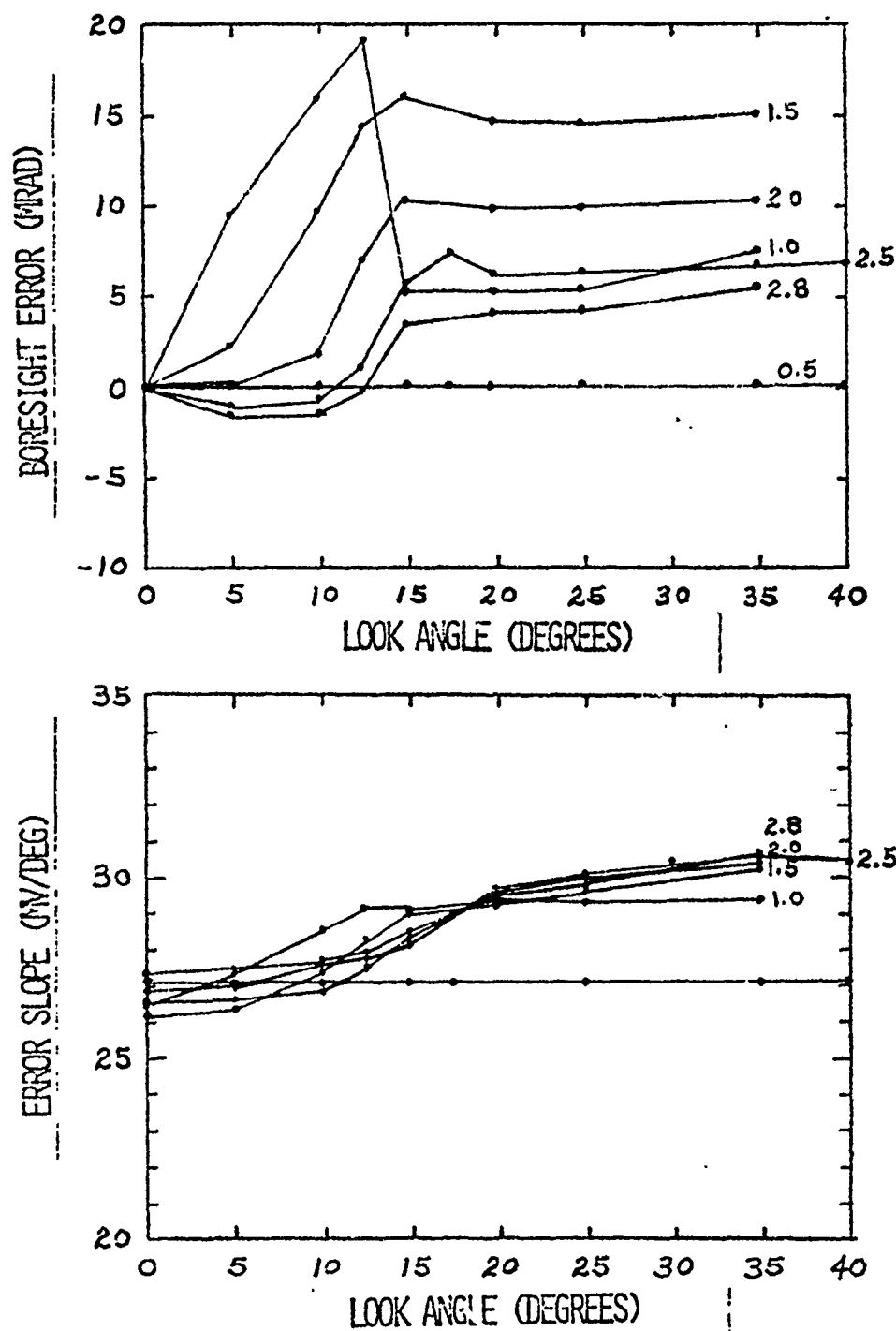
FIGURE 24. BORESIGHT ERROR AND MONOPULSE ERROR SLOPE VERSUS LOOK
ANGLE AND FINENESS RATIO FOR POLYIMIDE AT 12 GHZ.

5?
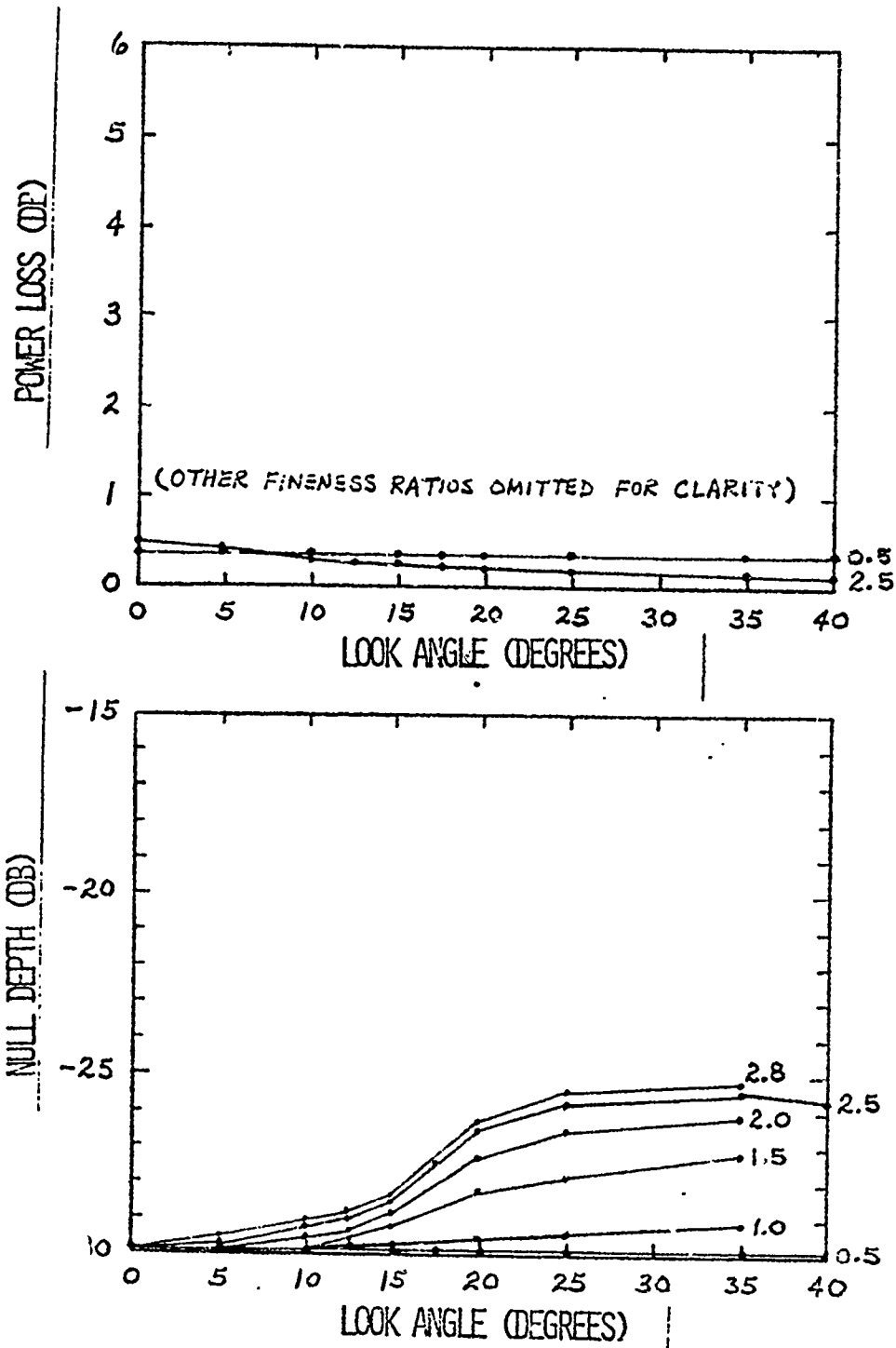
FIGURE 25. POWER LOSS IN 3 DB CONTOUR OF SUM PATTERN AND NULL DEPTH OF MONOPULSE RATIO VERSUS LOOK ANGLE AND FINENESS RATIO FOR POLYIMIDE AT 12 GHZ.

57

FIGURE 2: BORESIGHT ERROR AND MONOPULSE ERROR SLOPE VERSUS LOOK ANGLE AND FINENESS RATIO FOR POLYIMIDE AT 18 GHZ.

58
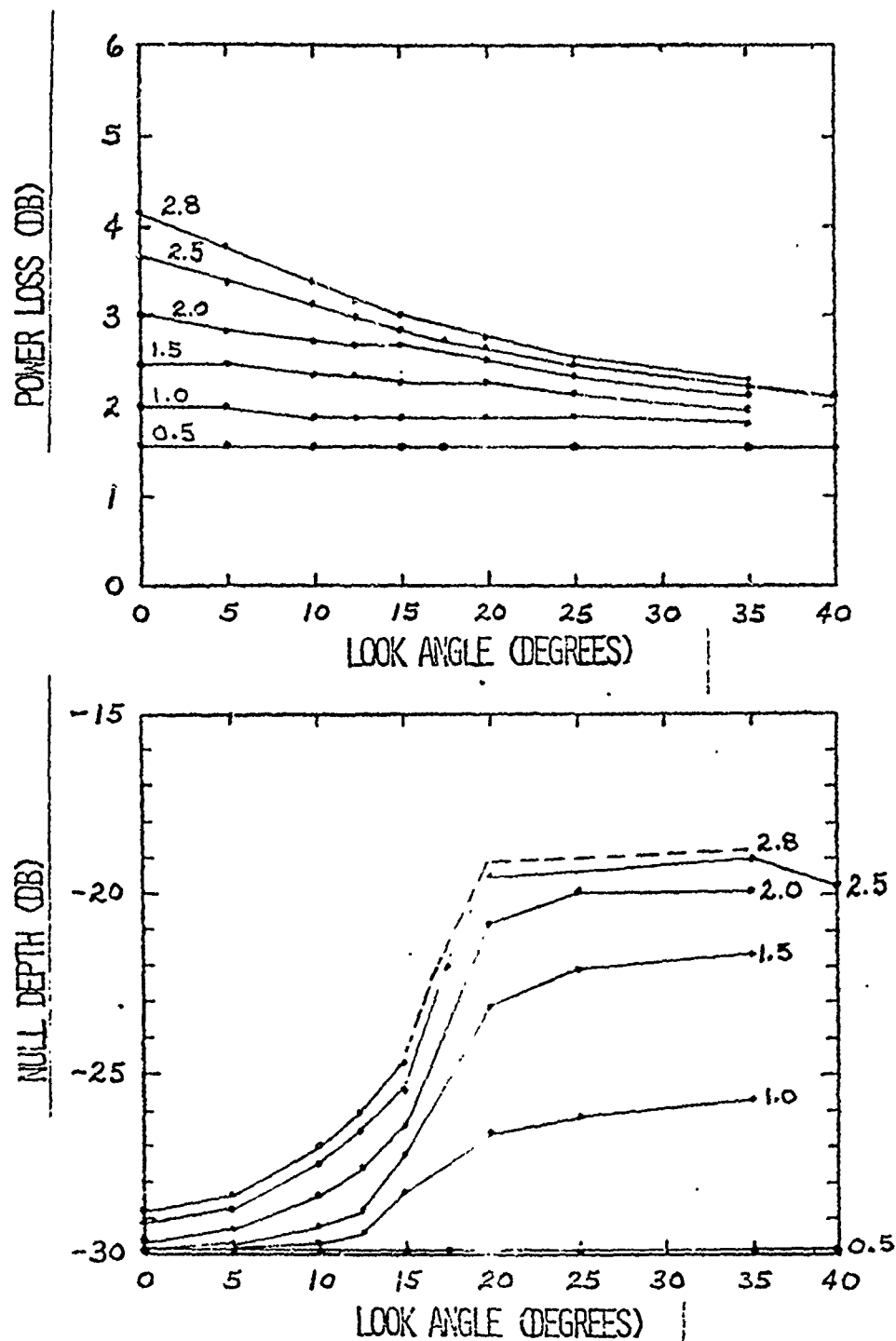
FIGURE 27. POWER LOSS IN 3 DB CONTOUR OF SUM PATTERN AND NULL
DEPTH OF MONOPULSE RATIO VERSUS LOOK ANGLE AND
FINENESS RATIO FOR POLYIMIDE AT 18 GHz.
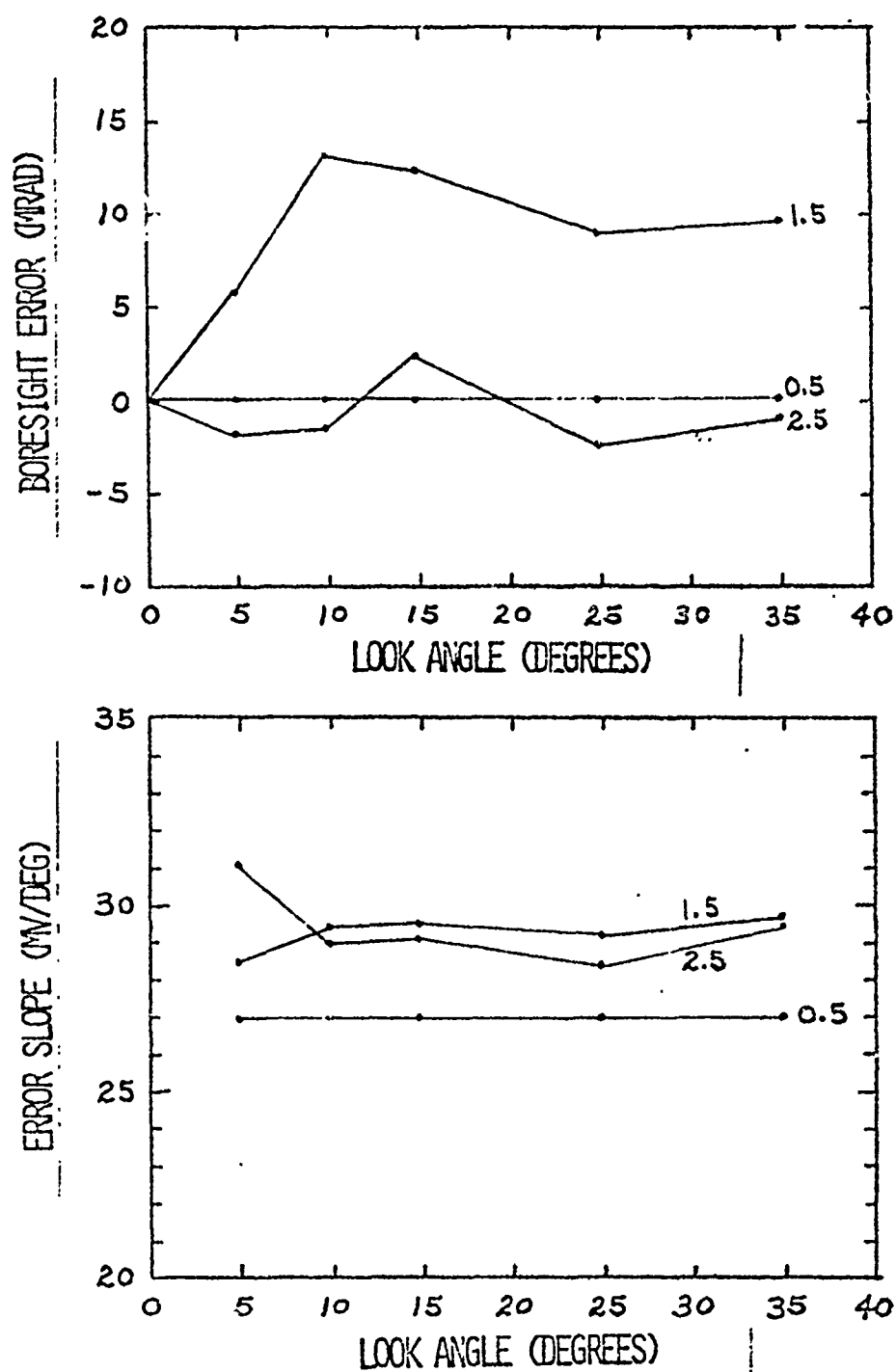
FIGURE 28. BORESIGHT ERROR AND MONOPULSE ERROR SLOPE VERSUS LOOK
ANGLE AND FINENESS RATIO FOR PYROCERAM AT 8 GHZ.
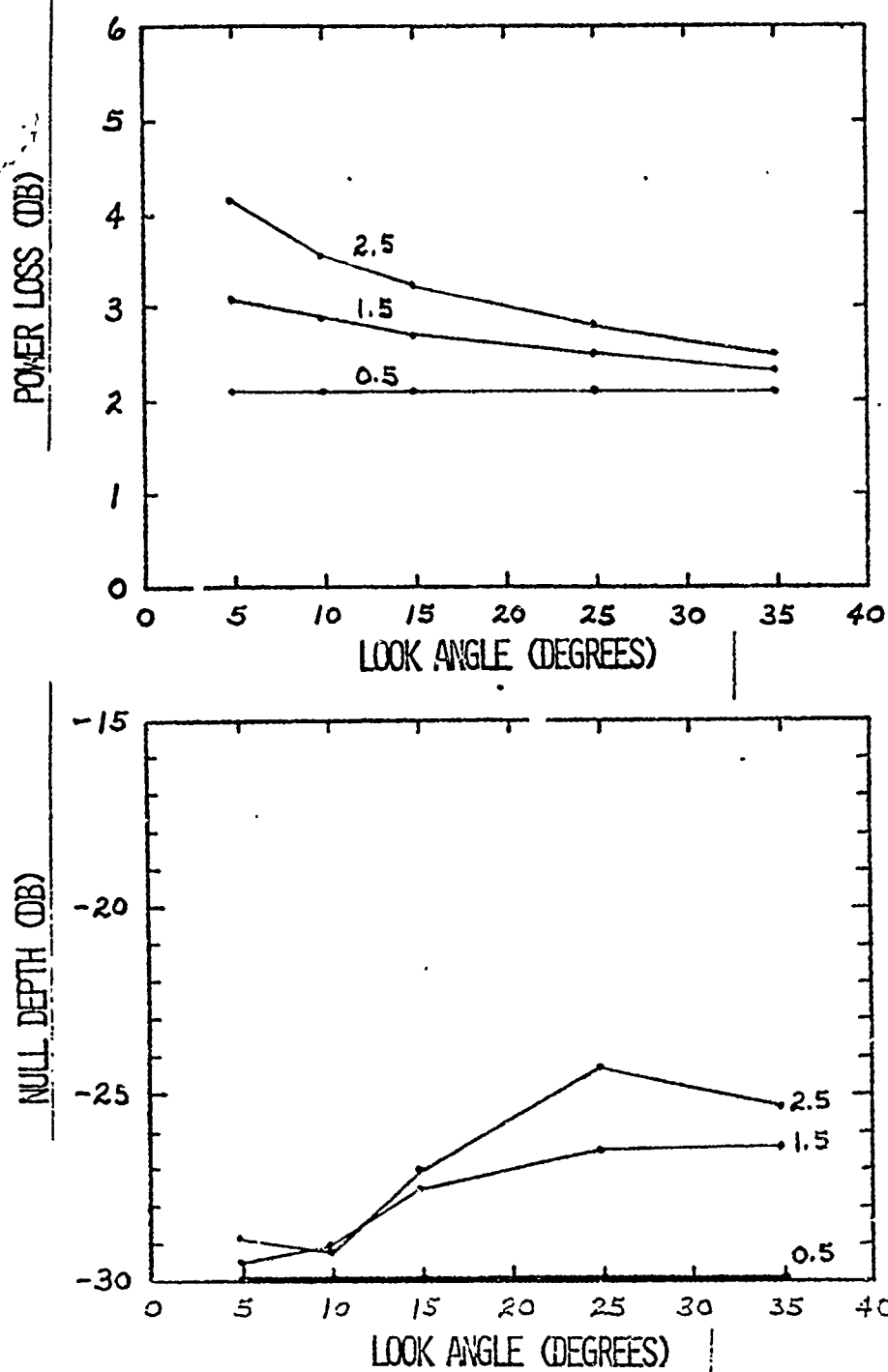
FIGURE 29. POWER LOSS IN 3 DB CONTOUR OF SUM PATTERN AND NULL
DEPTH OF MONOPULSE RATIO VERSUS LOOK ANGLE AND
FINENESS RATIO FOR PYROCERAM AT 8 GHZ.

61

FIGURE 30. BORESIGHT ERROR AND MONOPULSE ERROR SLOPE VERSUS LOOK
ANGLE AND FINENESS RATIO FOR PYROCERAM AT 12 GHZ.

FIGURE 31. POWER LOSS IN 3 DB CONTOUR OF SUM PATTERN AND NULL
DEPTH OF MONOPULSE RATIO VERSUS LOOK ANGLE AND
FINENESS RATIO FOR PYROCERAM AT 12 GHZ.

FIGURE 32. BORESIGHT ERROR AND MONOPULSE ERROR SLOPE VERSUS LOOK
ANGLE AND FINENESS RATIO FOR PYROCERAM AT 18 GHZ.
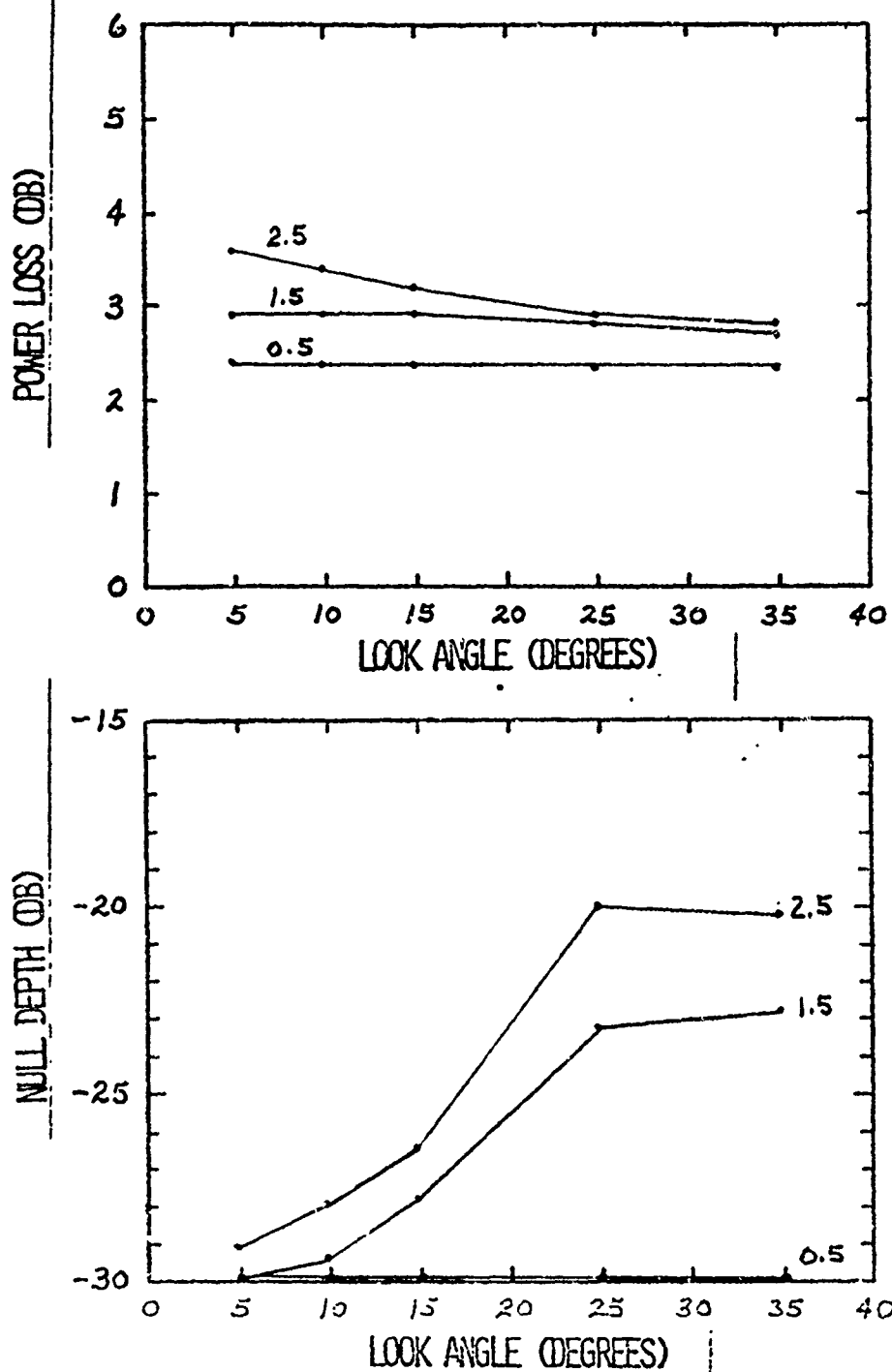
FIGURE 33. POWER LOSS IN 3 DB CONTOUR OF SUM PATTERN AND NULL
DEPTH OF MONOPULSE RATIO VERSUS LOOK ANGLE AND
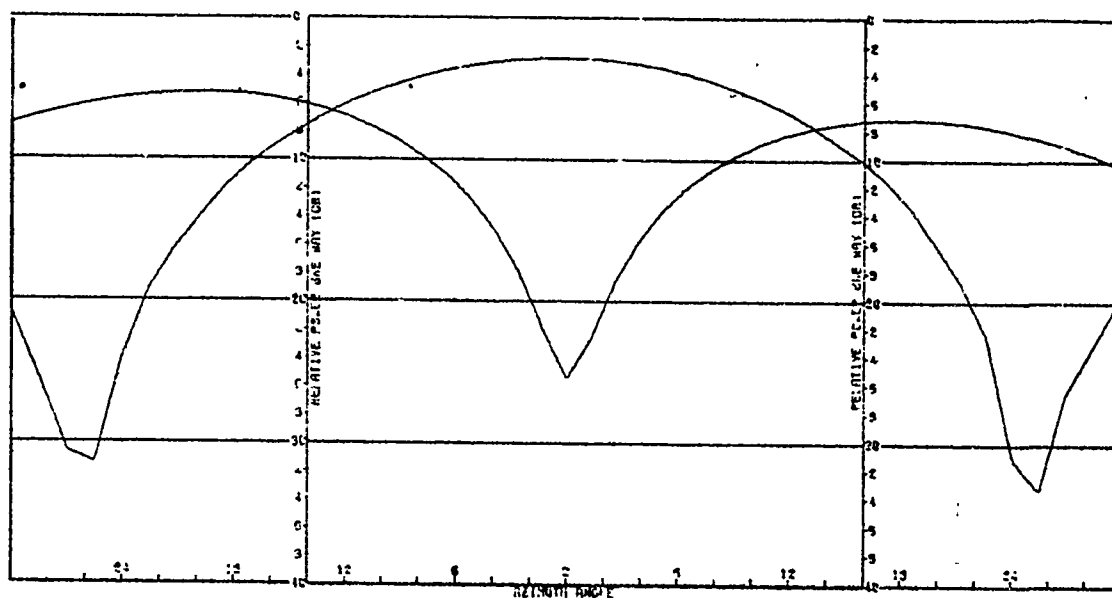FINENESS RATIO FOR PYROCERAM AT 18 GHZ.
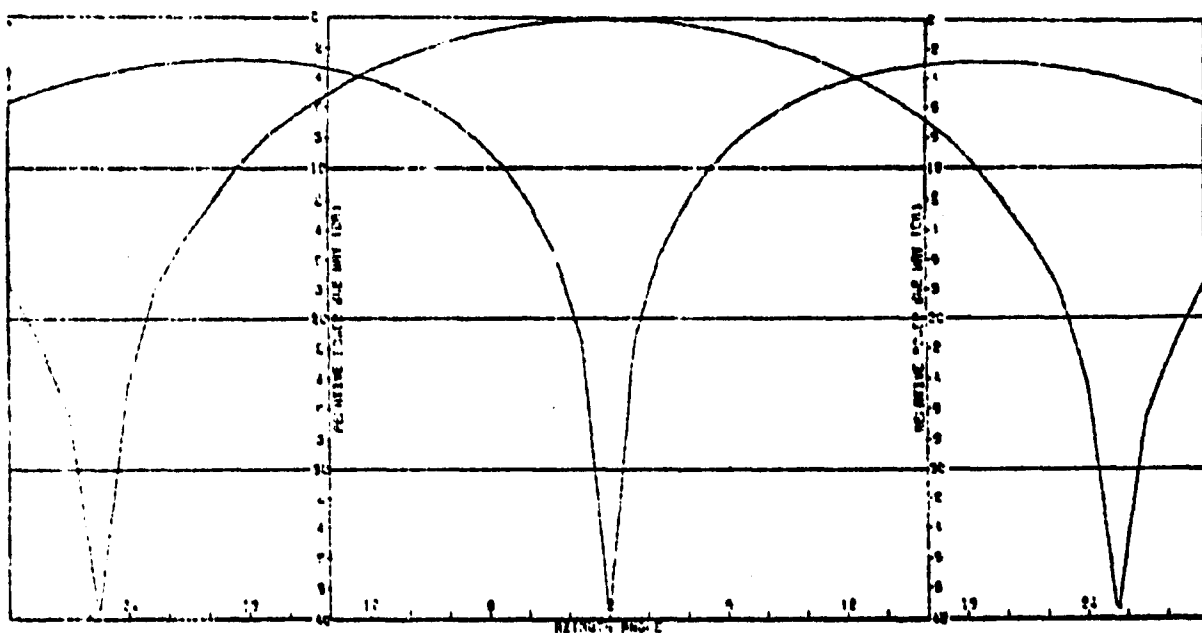
FIGURE 34. SUM AND AZIMUTH DIFFERENCE
PATTERNS FOR FINENESS RATIO OF 2.5 AT
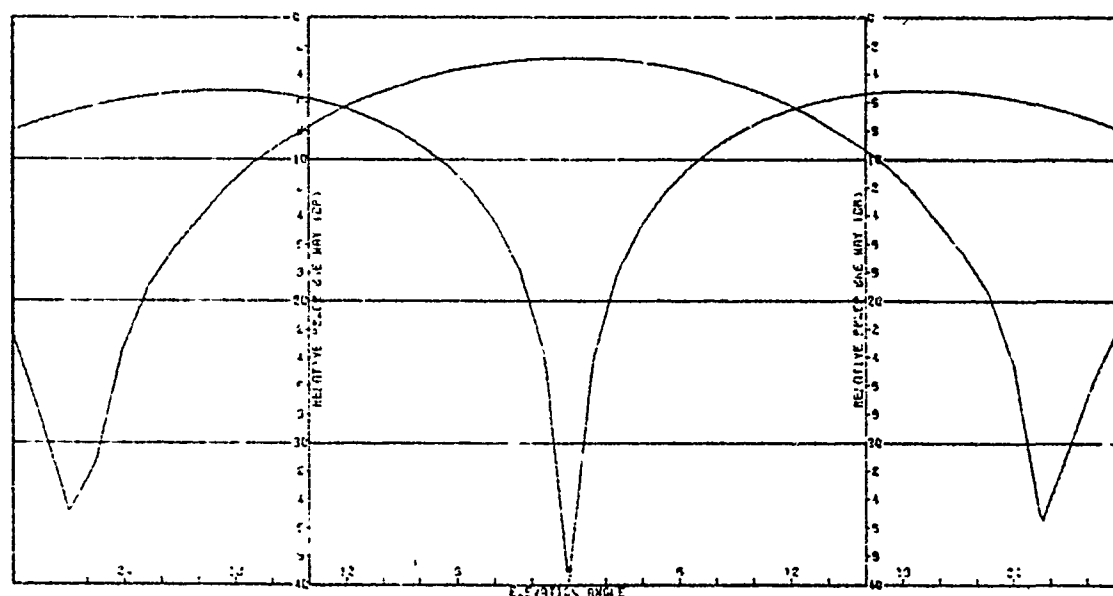8 GHZ FOR LOOK ANGLE OF 0.0 DEG IN
AZIMUTH AND 0.0 DEG IN ELEVATION.
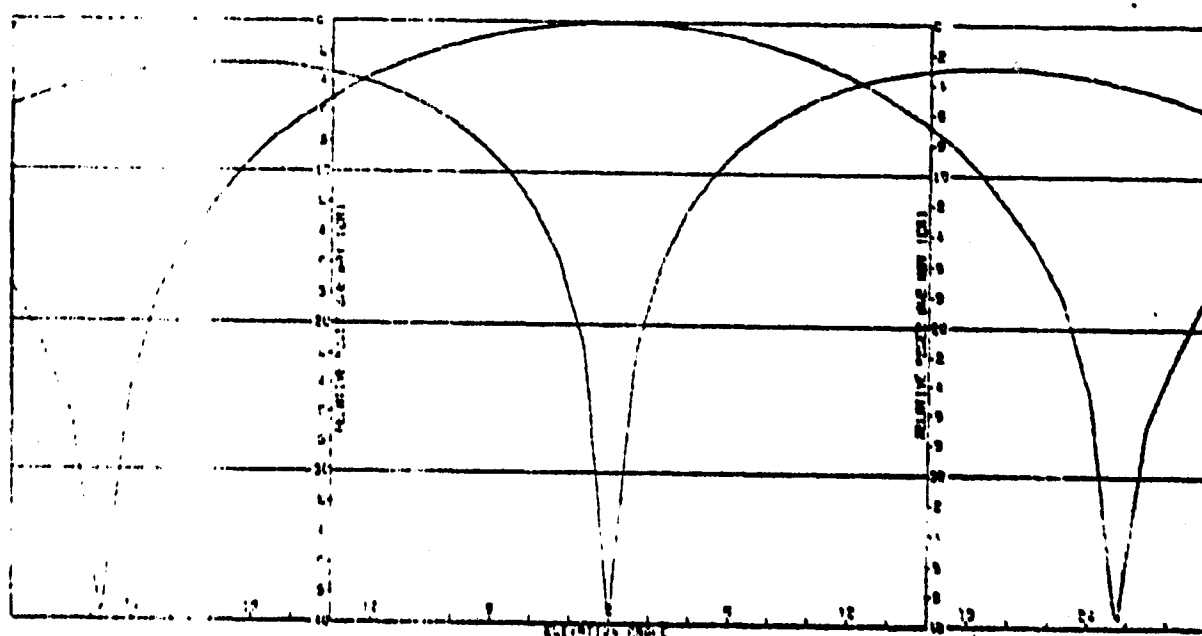
FIGURE 35. SUM AND ELEVATION DIFFERENCE
PATTERNS FOR FINENESS RATIO OF 2.5 AT
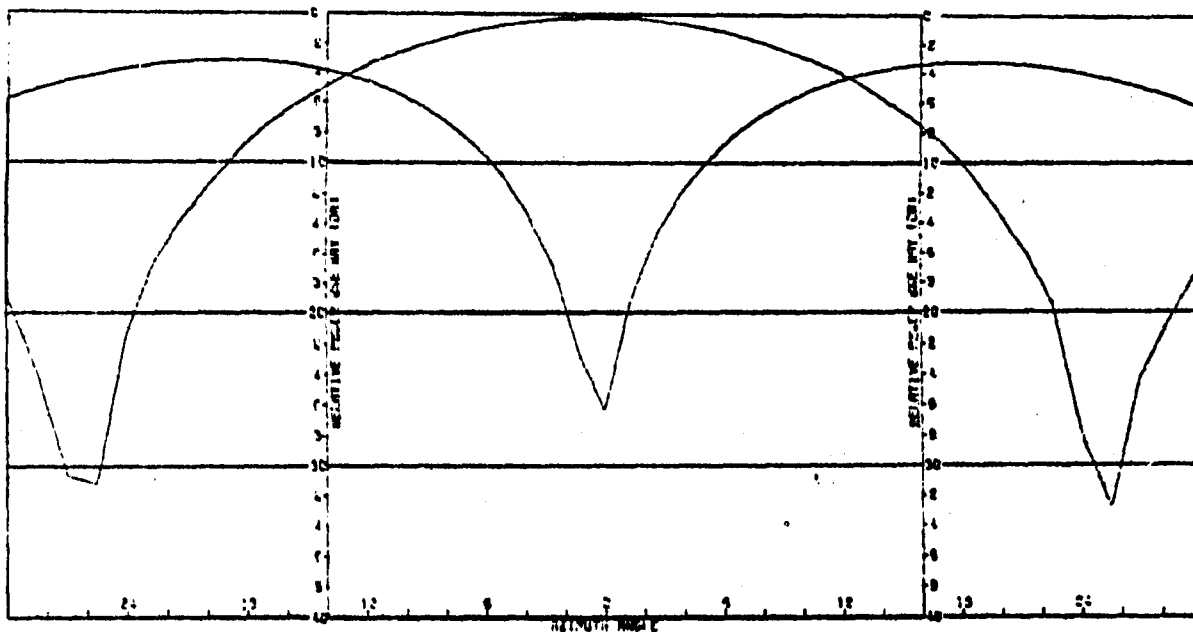8 GHZ FOR LOOK ANGLE OF 0.0 DEG IN
AZIMUTH AND 0.0 DEG IN ELEVATION.
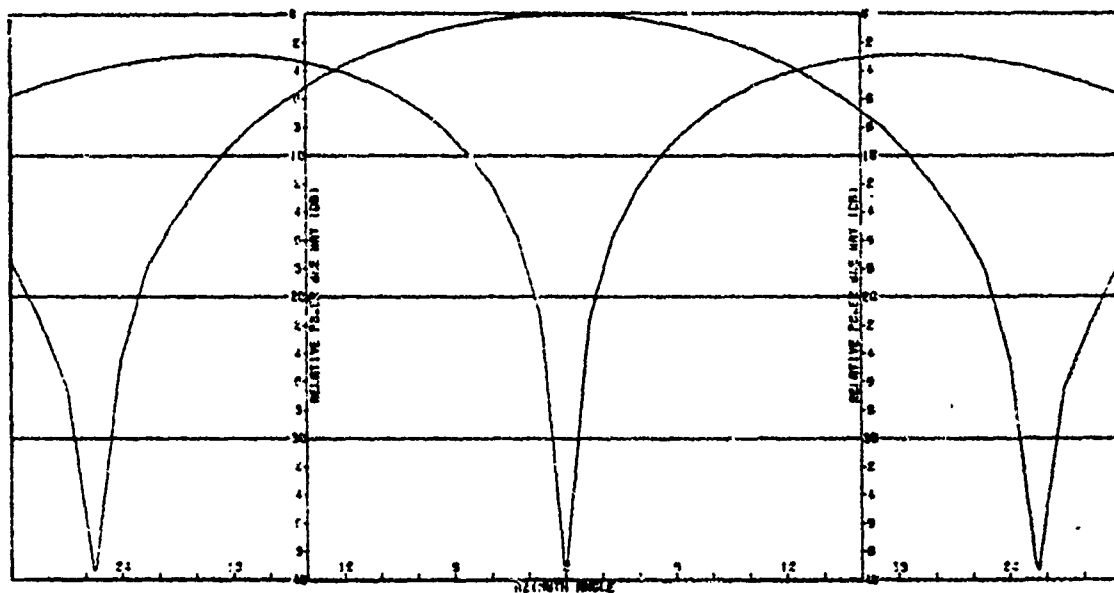
FIGURE 36. SUM AND AZIMUTH DIFFERENCE
PATTERNS FOR FINENESS RATIO OF 2.5 AT
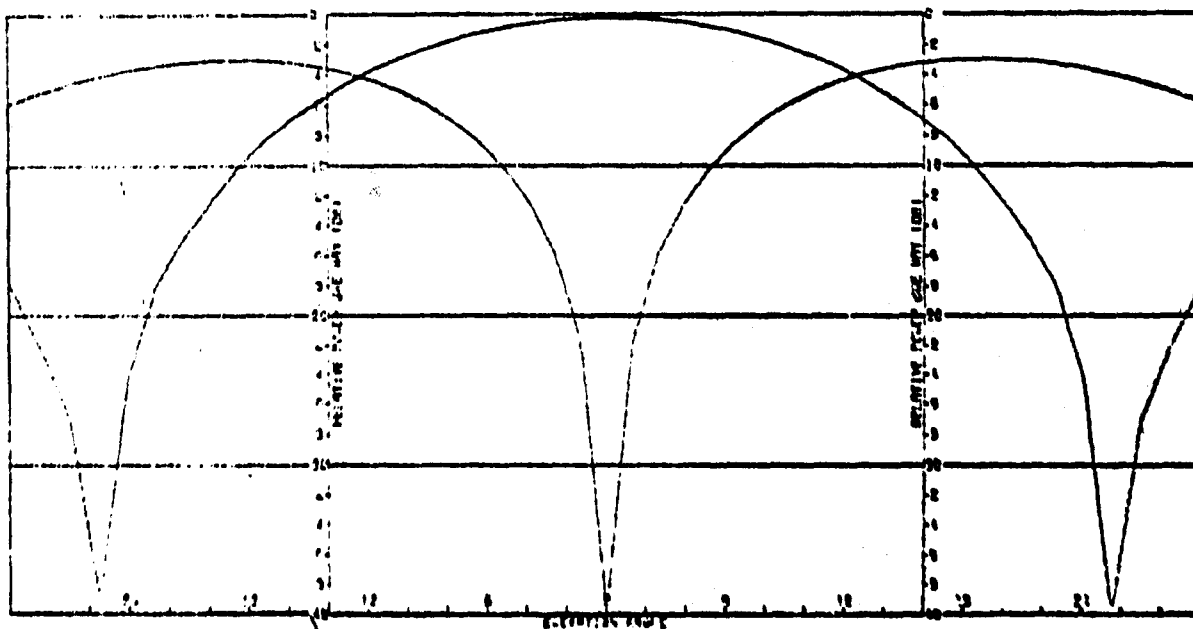12 GHZ FOR LOOK ANGLE OF 0.0 DEG IN
AZIMUTH AND 0.0 DEG IN ELEVATION.
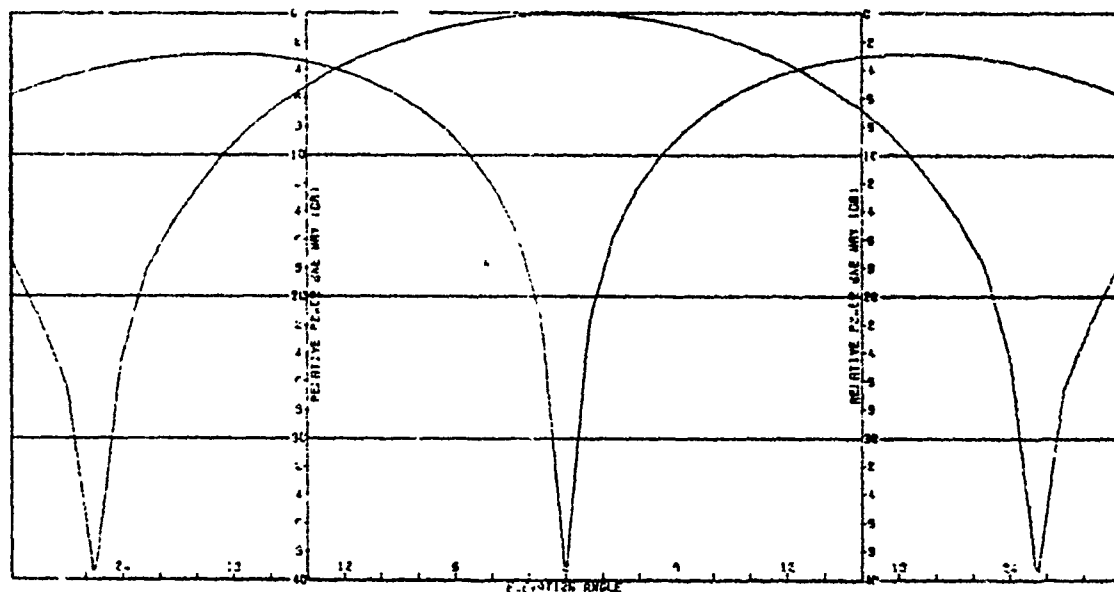
FIGURE 37. SUM AND ELEVATION DIFFERENCE
PATTERNS FOR FINENESS RATIO OF 2.5 AT
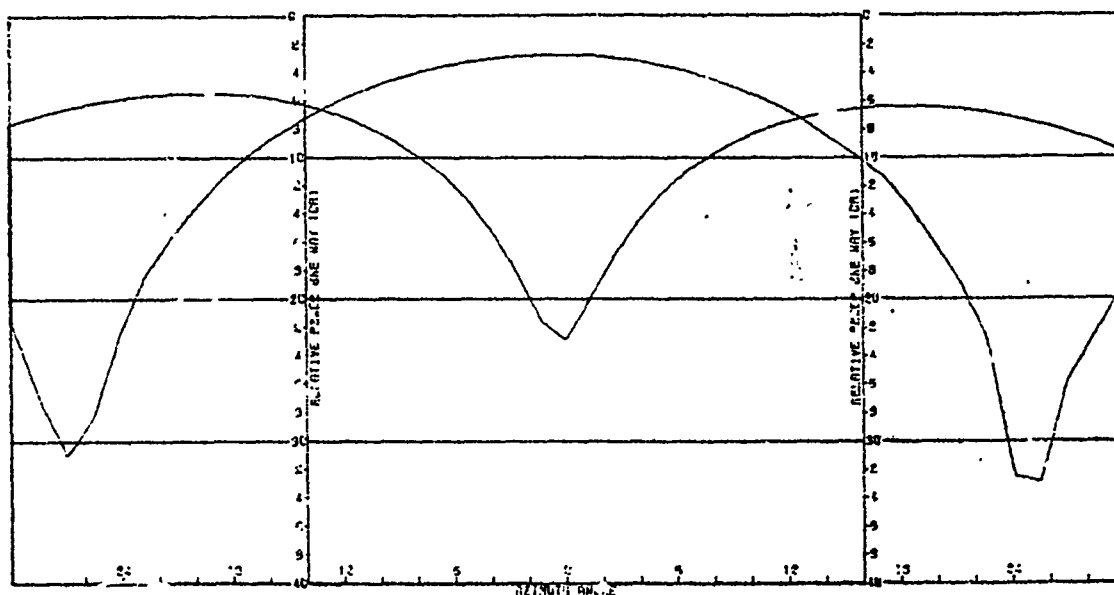12 GHZ FOR LOOK ANGLE OF 0.0 DEG IN
AZIMUTH AND 0.0 DEG IN ELEVATION.
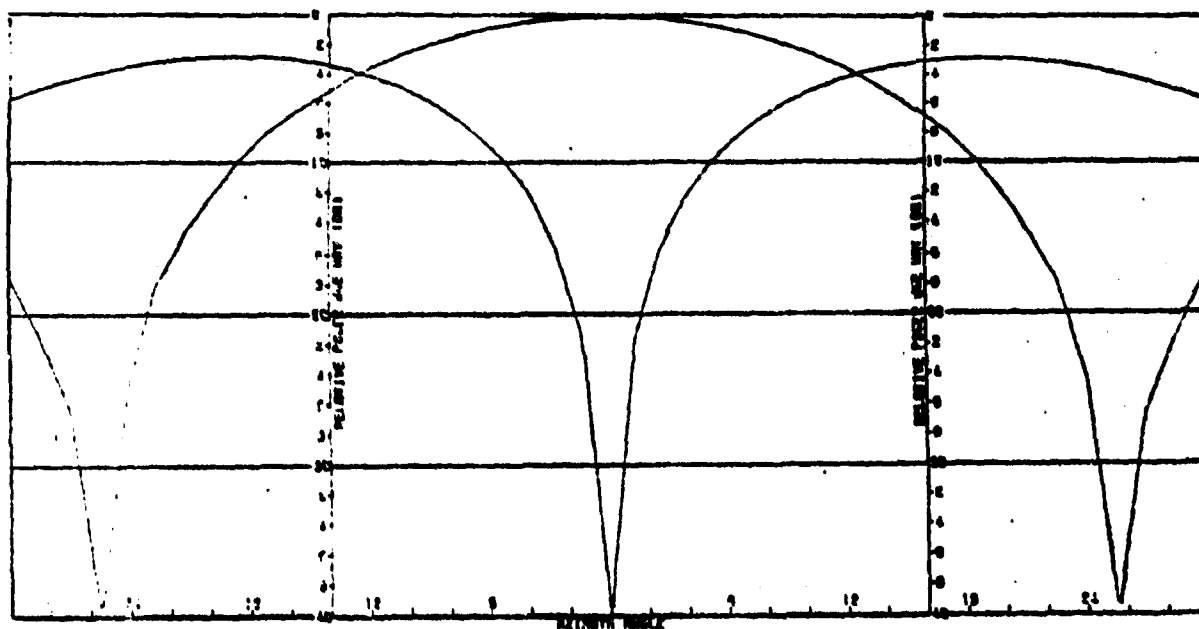
FIGURE 38. SUM AND AZIMUTH DIFFERENCE
PATTERNS FOR FINENESS RATIO OF 2.5 AT
18 GHZ FOR LOOK ANGLE OF 0.0 DEG IN
AZIMUTH AND 0.0 DEG IN ELEVATION.
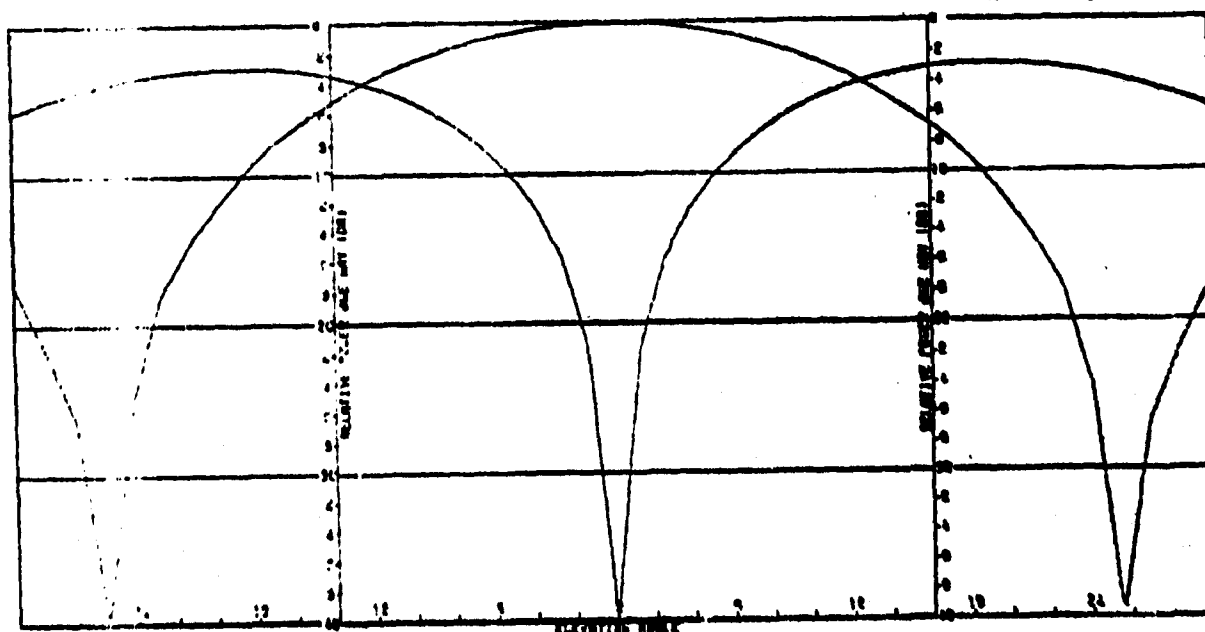
FIGURE 39. SUM AND ELEVATION DIFFERENCE
PATTERNS FOR FINENESS RATIO OF 2.5 AT
18 GHZ FOR LOOK ANGLE OF 0.0 DEG IN
AZIMUTH AND 0.0 DEG IN ELEVATION.
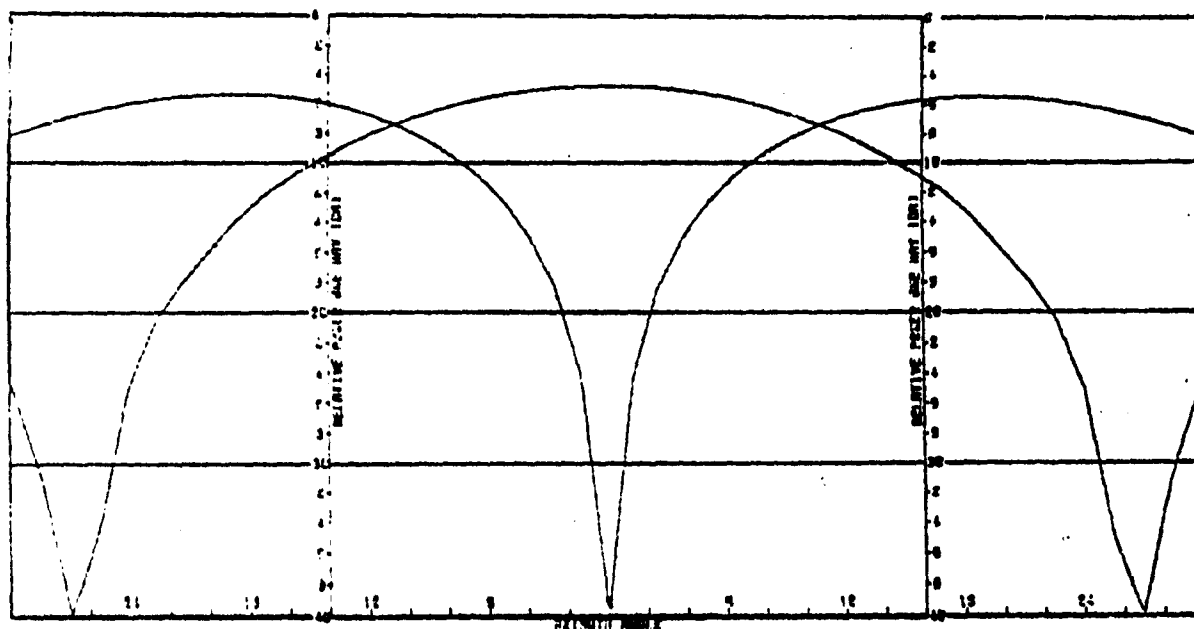
FIGURE 40. SUM AND AZIMUTH DIFFERENCE
PATTERNS FOR FINENESS RATIO OF 2.5 AT
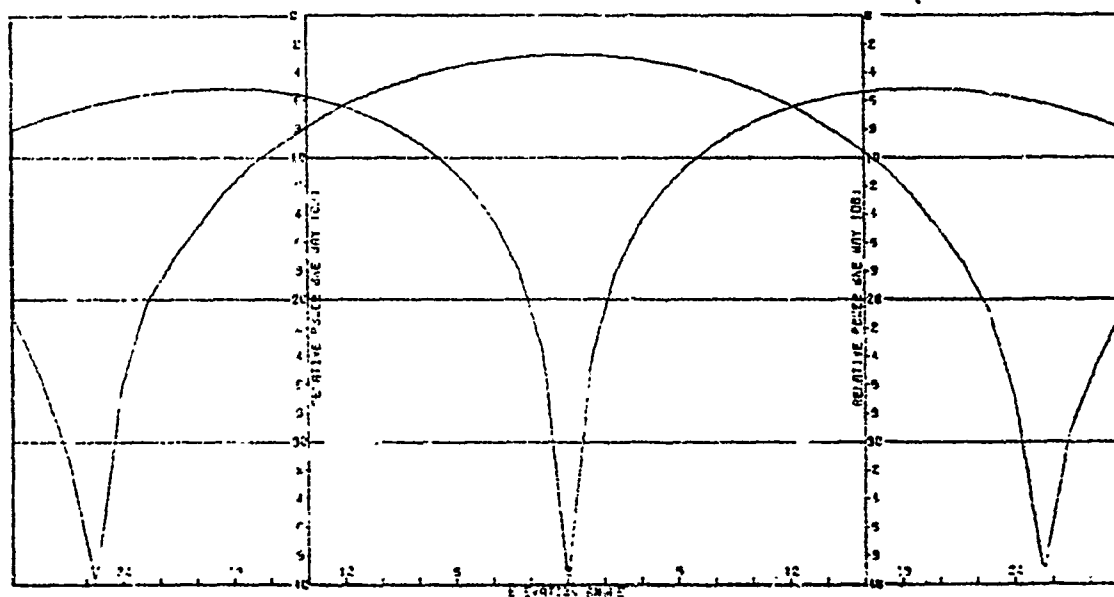8 GHZ FOR LOOK ANGLE OF 0.0 DEG IN
AZIMUTH AND 0.0 DEG IN ELEVATION.
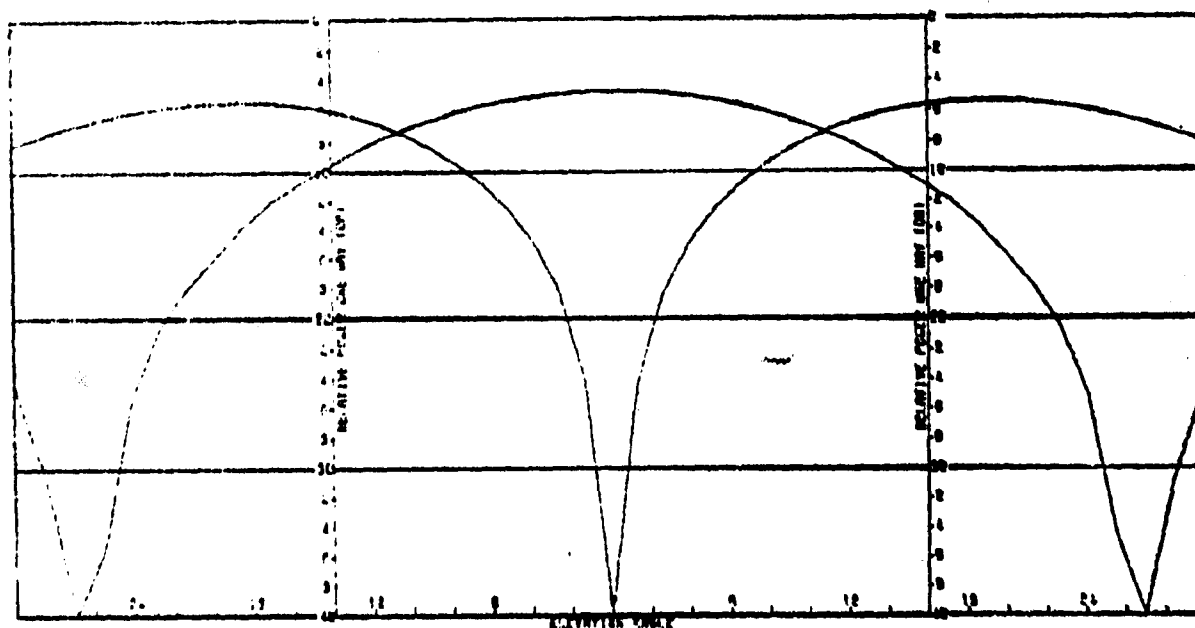
FIGURE 41. SUM AND ELEVATION DIFFERENCE
PATTERNS FOR FINENESS RATIO OF 2.5 AT
8 GHZ FOR LOOK ANGLE OF 0.0 DEG IN
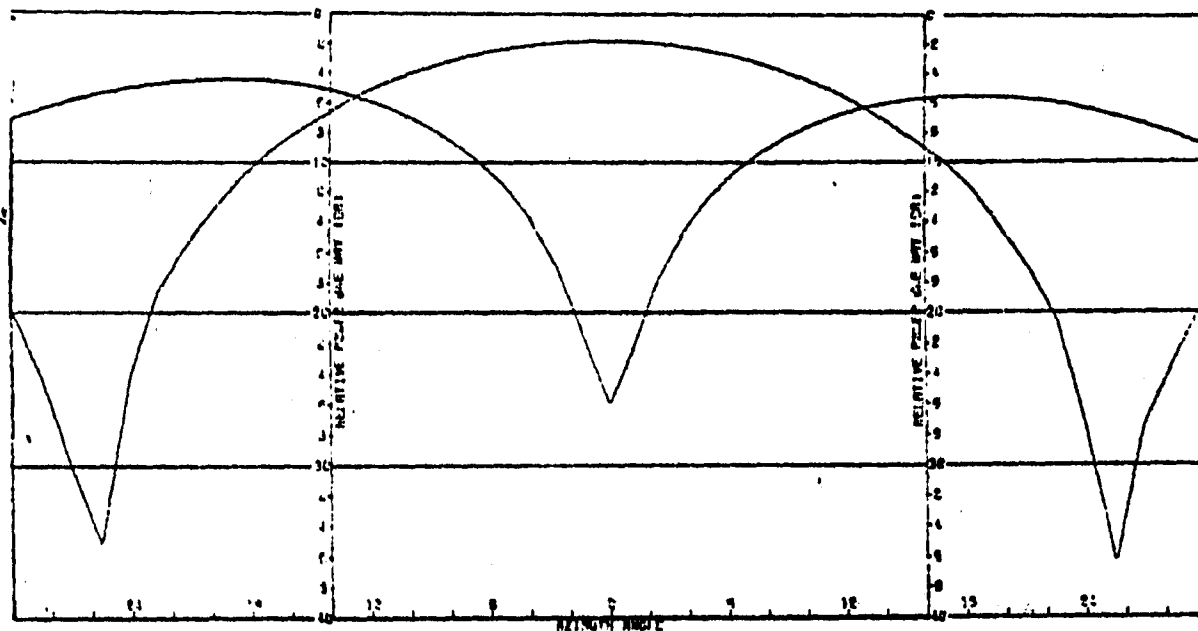AZIMUTH AND 0.0 DEG IN ELEVATION.

69
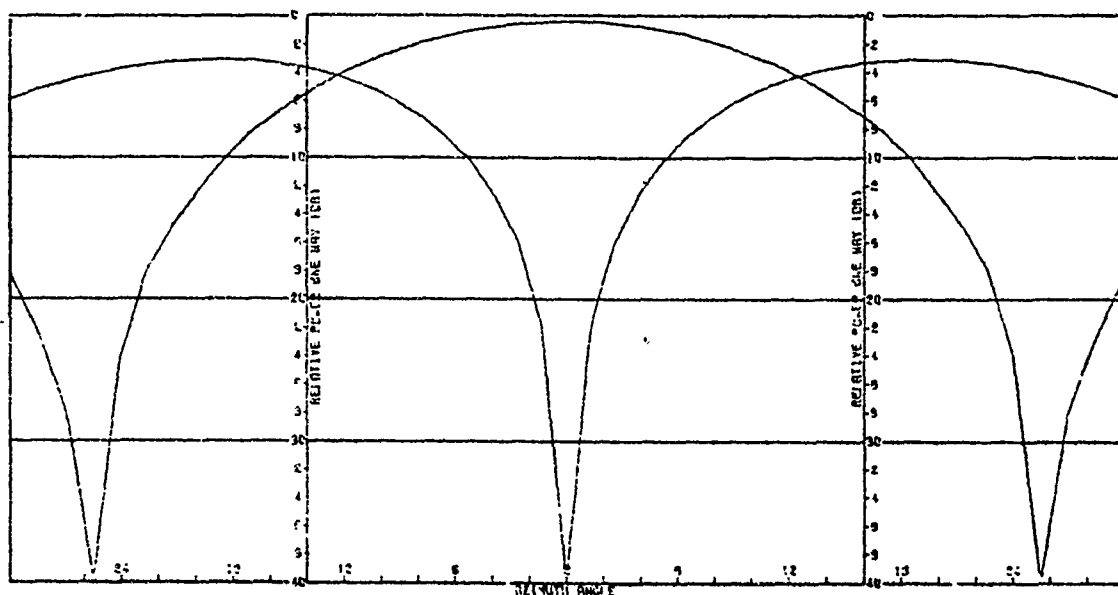
FIGURE 42. SUM AND AZIMUTH DIFFERENCE
PATTERNS FOR FINENESS RATIO OF 2.5 AT
12 GHZ FOR LOOK ANGLE OF 0.0 DEG IN
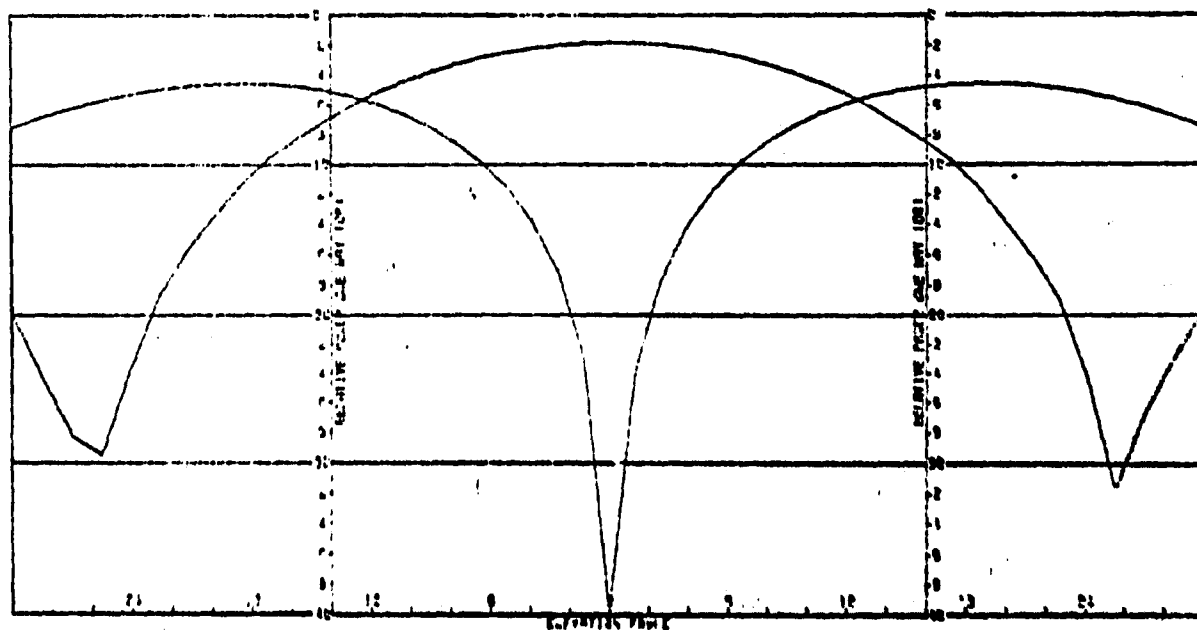AZIMUTH AND 0.0 DEG IN ELEVATION.
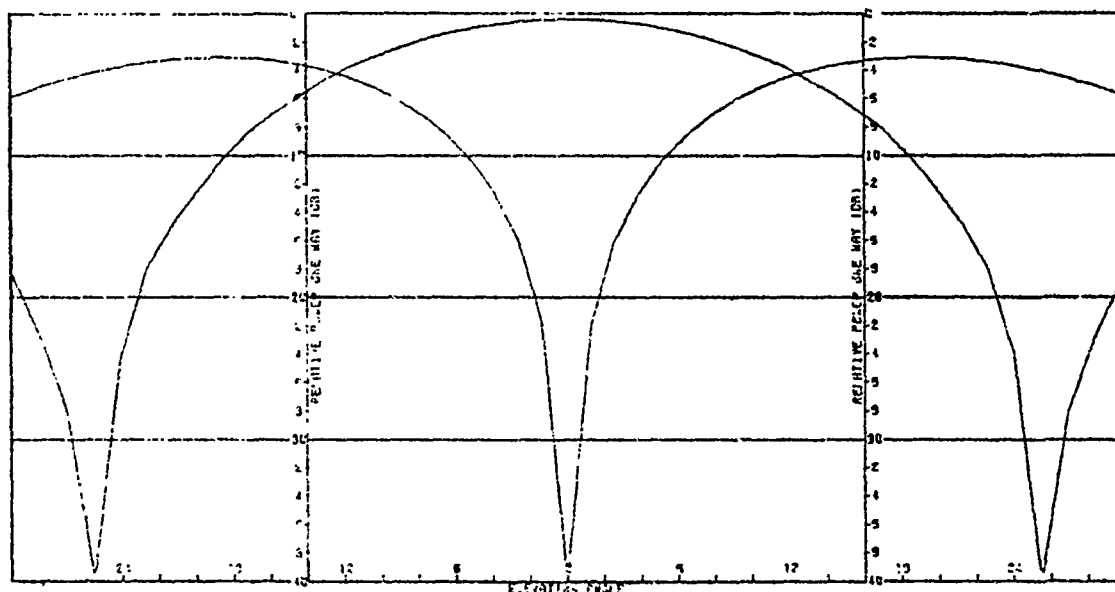
FIGURE 43. SUM AND ELEVATION DIFFERENCE
PATTERNS FOR FINENESS RATIO OF 2.5 AT
12 GHZ FOR LOOK ANGLE OF 0.0 DEG IN
AZIMUTH AND 0.0 DEG IN ELEVATION.
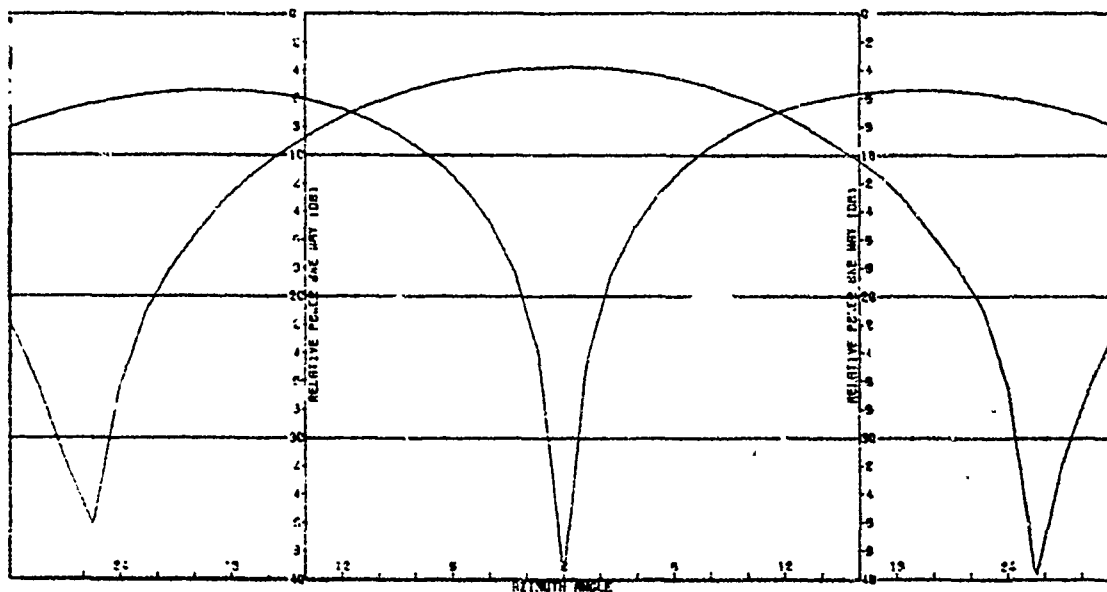
FIGURE 44. SUM AND AZIMUTH DIFFERENCE
PATTERNS FOR FINENESS RATIO OF 2.5 AT
18 GHZ FOR LOOK ANGLE OF 0.0 DEG IN
AZIMUTH AND 0.0 DEG IN ELEVATION.
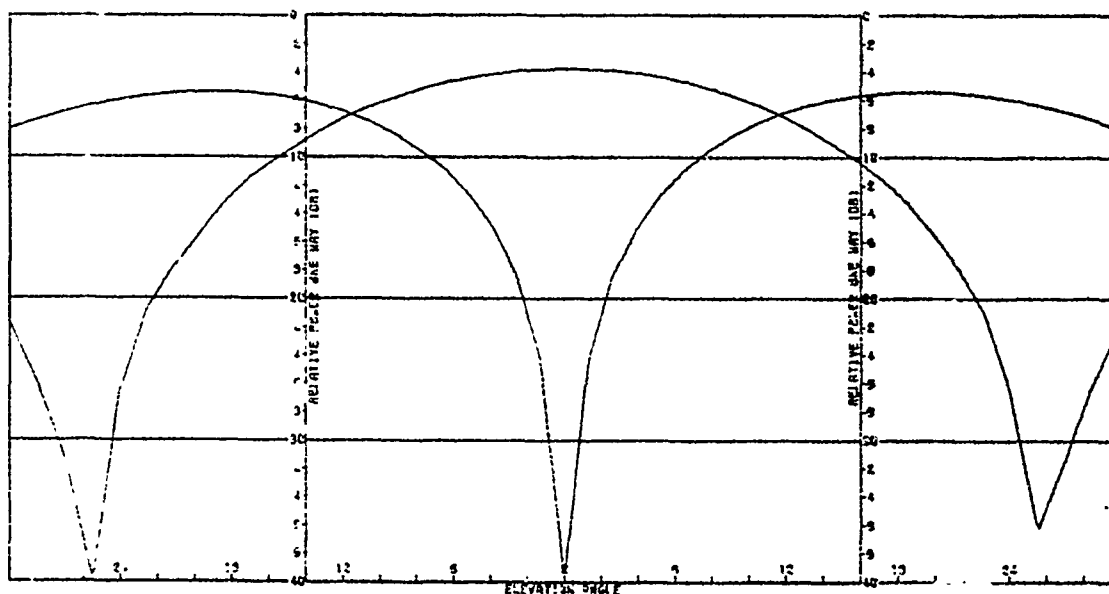
FIGURE 45. SUM AND ELEVATION DIFFERENCE
PATTERNS FOR FINENESS RATIO OF 2.5 AT
18 GHZ FOR LOOK ANGLE OF 0.0 DEG IN
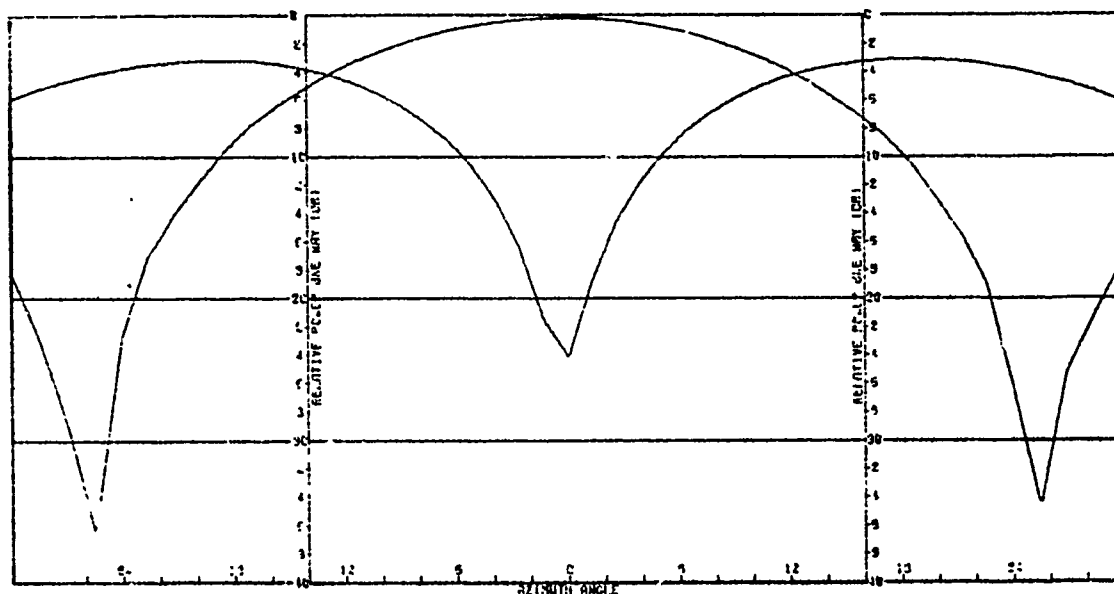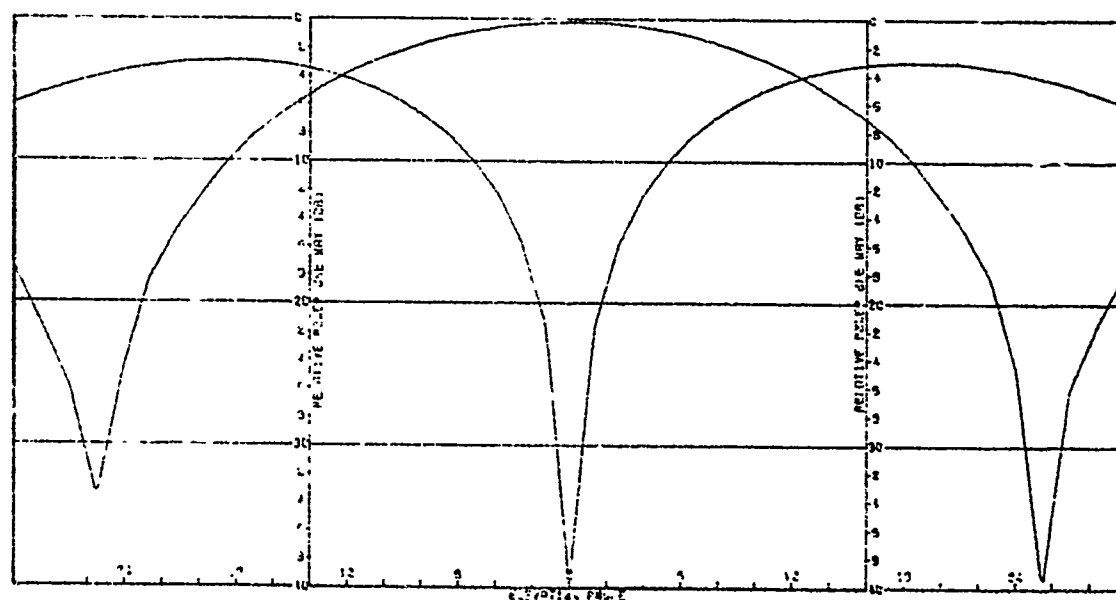AZIMUTH AND 0.0 DEG IN ELEVATION.

71

FIGURE 46. SUM AND AZIMUTH DIFFERENCE
PATTERNS FOR FINENESS RATIO OF 2.5 AT
8 GHZ FOR LOOK ANGLE OF 17.5 DEG IN
AZIMUTH AND 0.0 DEG IN ELEVATION.

FIGURE 47. SUM AND ELEVATION DIFFERENCE
PATTERNS FOR FINENESS RATIO OF 2.5 AT
8 GHZ FOR LOOK ANGLE OF 17.5 DEG IN
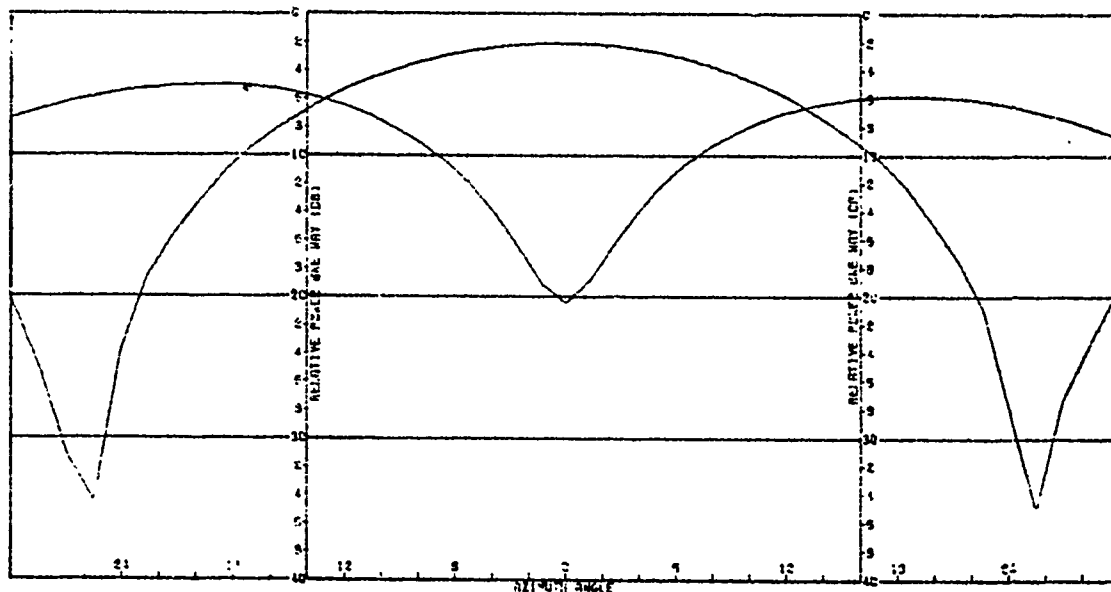AZIMUTH AND 0.0 DEG IN ELEVATION.

FIGURE 48. SUM AND AZIMUTH DIFFERENCE
PATTERNS FOR FINENESS RATIO OF 2.5 AT
12 GHZ FOR LOOK ANGLE OF 17.5 DEG IN
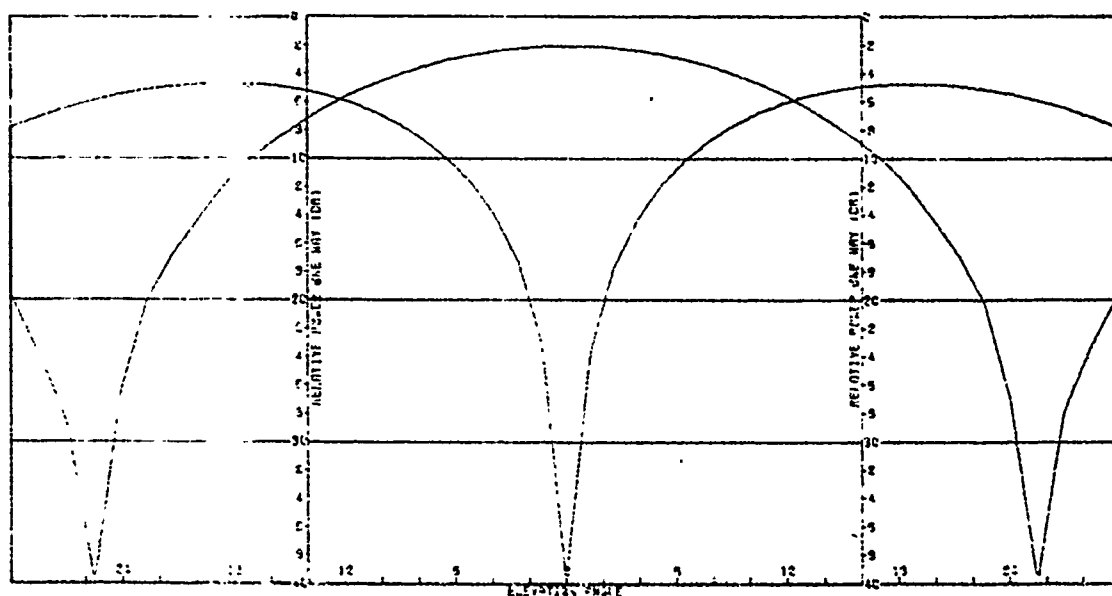AZIMUTH AND 0.0 DEG IN ELEVATION.

FIGURE 49. SUM AND ELEVATION DIFFERENCE
PATTERNS FOR FINENESS RATIO OF 2.5 AT
12 GHZ FOR LOOK ANGLE OF 17.5 DEG IN
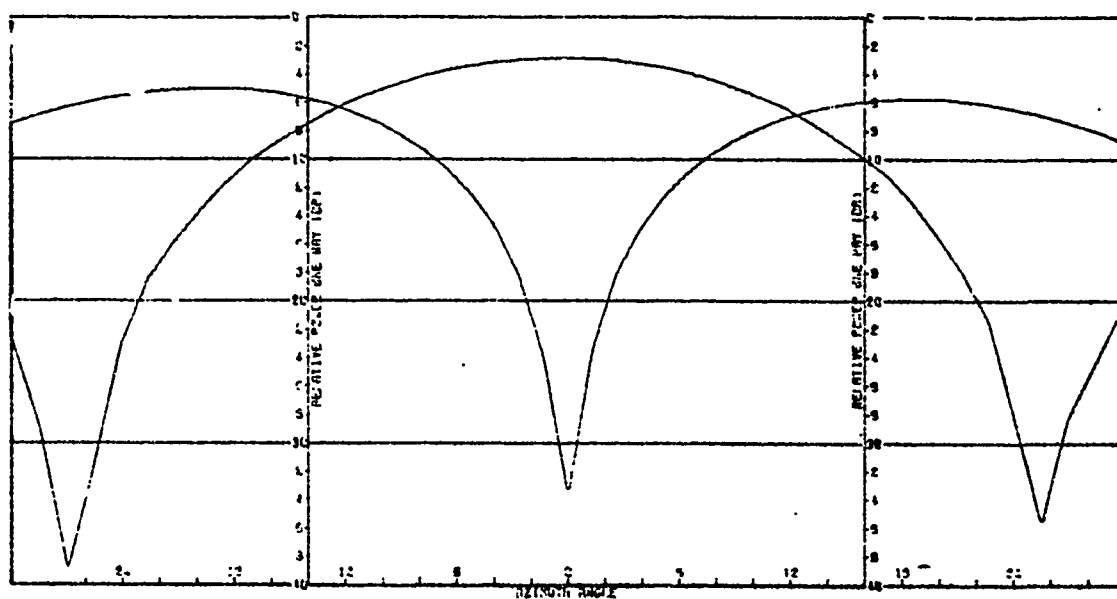AZIMUTH AND 0.0 DEG IN ELEVATION.

73

FIGURE 50. SUM AND AZIMUTH DIFFERENCE
PATTERNS FOR FINENESS RATIO OF 2.5 AT
18 GHZ FOR LOOK ANGLE OF 17.5 DEG IN
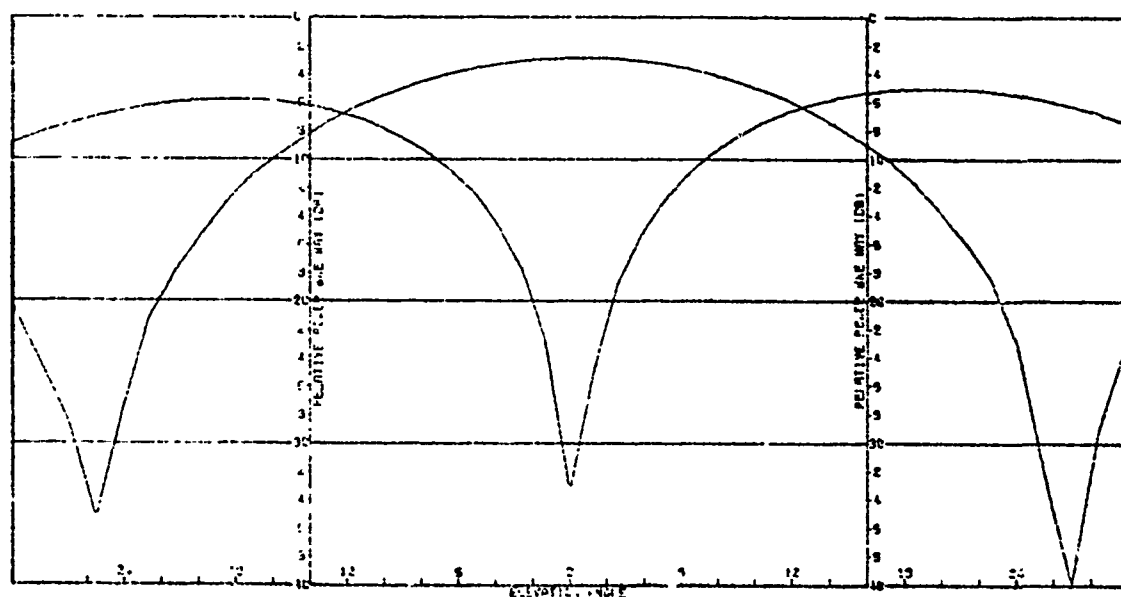AZIMUTH AND 0.0 DEG IN ELEVATION.

FIGURE 51. SUM AND ELEVATION DIFFERENCE
PATTERNS FOR FINENESS RATIO OF 2.5 AT
18 GHZ FOR LOOK ANGLE OF 17.5 DEG IN
AZIMUTH AND 0.0 DEG IN ELEVATION.

74

FIGURE 52. SUM AND AZIMUTH DIFFERENCE
   PATTERNS FOR FINENESS RATIO OF 2.5 AT
   8   GHZ FOR LOOK ANGLE OF 40.0 DEG IN
   AZIMUTH AND 0.0   DEG IN ELEVATION.

FIGURE 53. SUM AND ELEVATION DIFFERENCE
   PATTERNS FOR FINENESS RATIO OF 2.5 AT
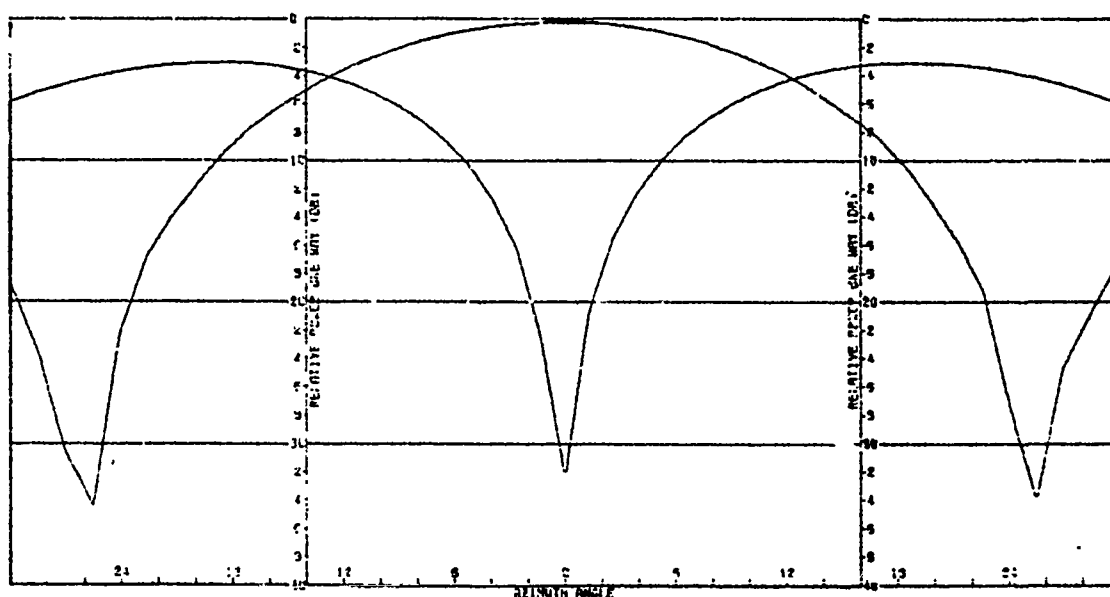   8   GHZ FOR LOOK ANGLE OF 40.0 DEG IN
   AZIMUTH AND 0.0   DEG IN ELEVATION.

FIGURE 54. SUM AND AZIMUTH DIFFERENCE
PATTERNS FOR FINENESS RATIO OF 2.5 AT
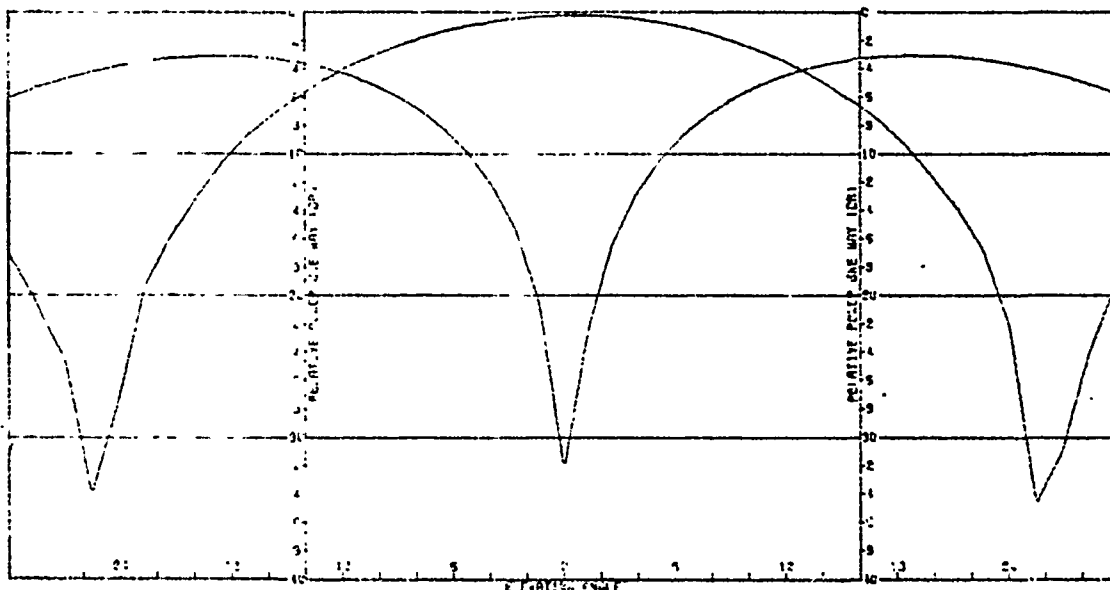12 GHZ FOR LOOK ANGLE OF 40.0 DEG IN
AZIMUTH AND 0.0 DEG IN ELEVATION.

FIGURE 55. SUM AND ELEVATION DIFFERENCE
PATTERNS FOR FINENESS RATIO OF 2.5 AT
12 GHZ FOR LOOK ANGLE OF 40.0 DEG IN
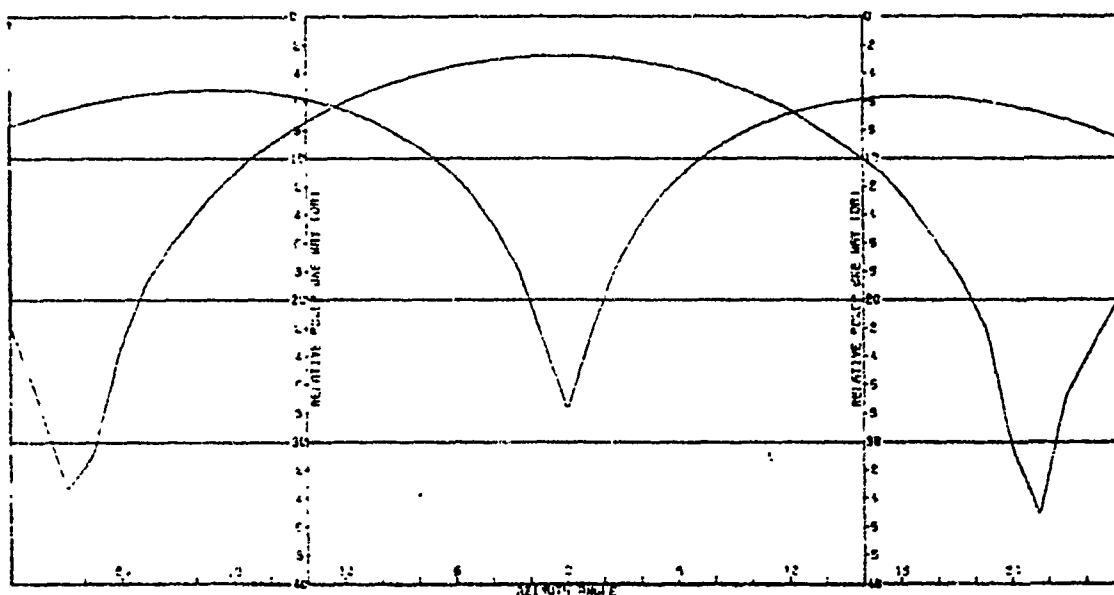AZIMUTH AND 0.0 DEG IN ELEVATION.

76

FIGURE 56. SUM AND AZIMUTH DIFFERENCE
PATTERNS FOR FINENESS RATIO OF 2.5 AT
18 GHZ FOR LOOK ANGLE OF 40.0 DEG IN
AZIMUTH AND 0.0 DEG IN ELEVATION.

FIGURE 57 SUM AND ELEVATION DIFFERENCE
PATTERNS FOR FINENESS RATIO OF 2.5 AT
18 GHZ FOR LOOK ANGLE OF 40.0 DEG IN
AZIMUTH AND 0.0 DEG IN ELEVATION.

77

FIGURE 58. SUM AND AZIMUTH DIFFERENCE
PATTERNS FOR FINENESS RATIO OF 2.5 AT
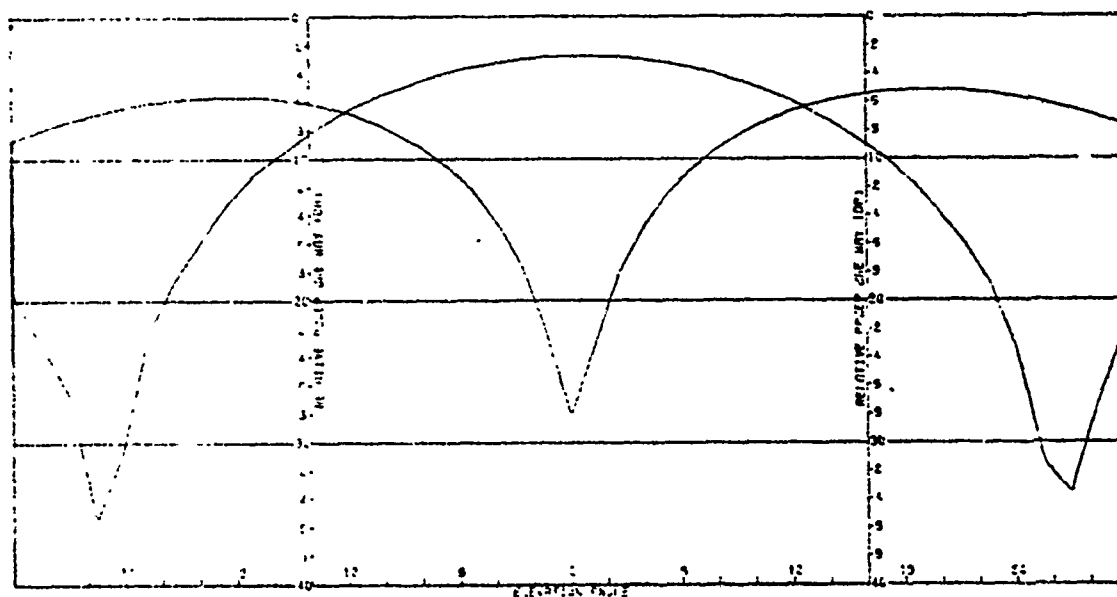8 GHZ FOR LOOK ANGLE OF 17.5 DEG IN
AZIMUTH AND 45.0 DEG IN ELEVATION.

FIGURE 59. SUM AND ELEVATION DIFFERENCE
PATTERNS FOR FINENESS RATIO OF 2.5 AT
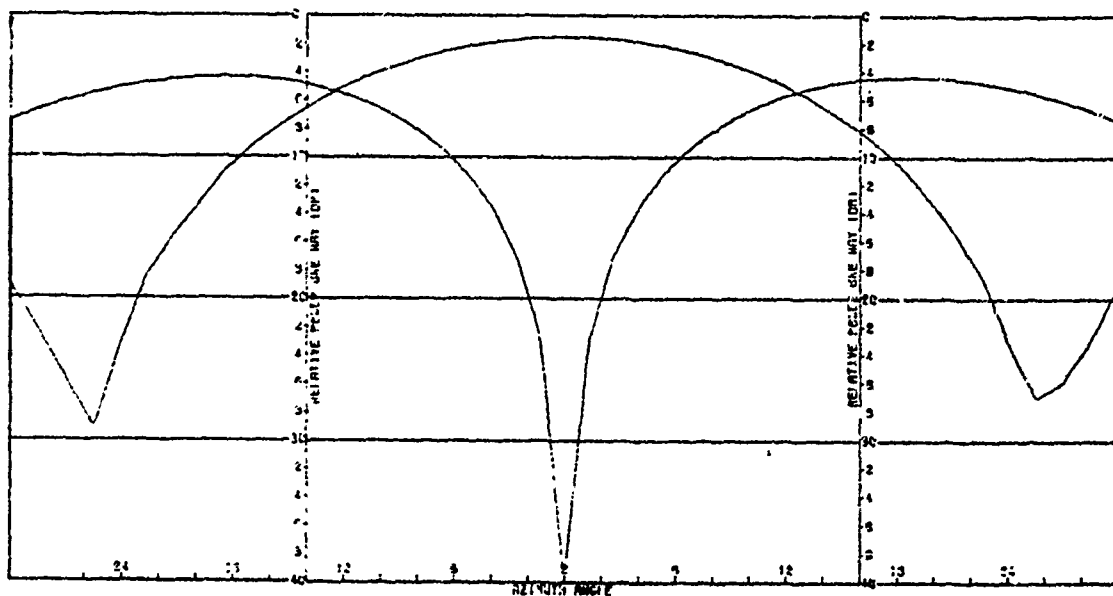8 GHZ FOR LOOK ANGLE OF 17.5 DEG IN
AZIMUTH AND 45.0 DEG IN ELEVATION.

78

FIGURE 60. SUM AND AZIMUTH DIFFERENCE
PATTERNS FOR FINENESS RATIO OF 2.5 AT
12 GHZ FOR LOOK ANGLE OF 17.5 DEG IN
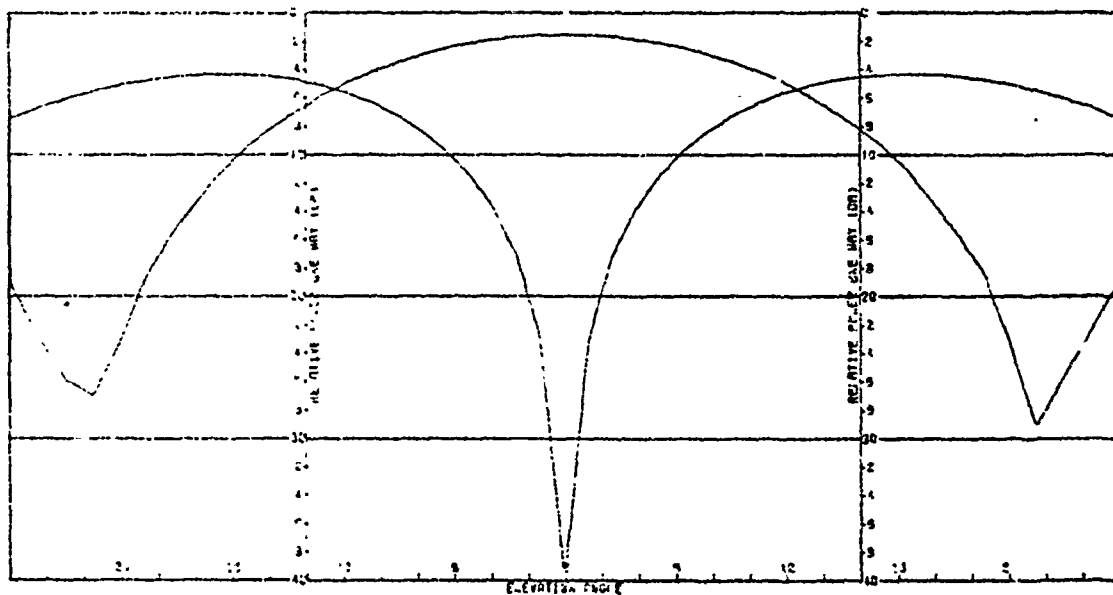AZIMUTH AND 45.0 DEG IN ELEVATION.

FIGURE 61. SUM AND ELEVATION DIFFERENCE
PATTERNS FOR FINENESS RATIO OF 2.5 AT
12 GHZ FOR LOOK ANGLE OF 17.5 DEG IN
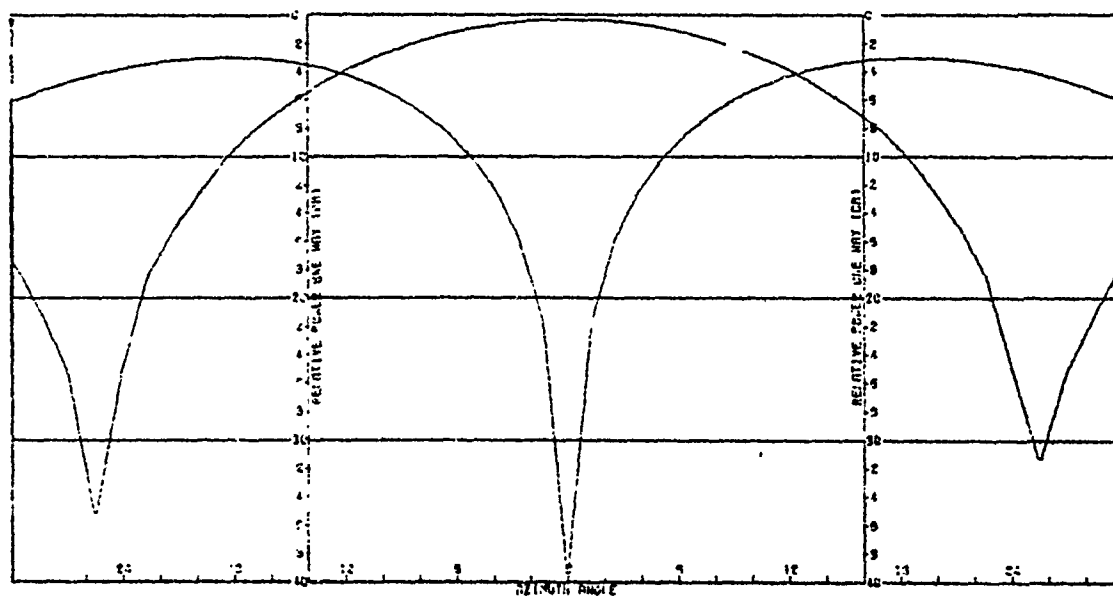AZIMUTH AND 45.0 DEG IN ELEVATION.

FIGURE 62. SUM AND AZIMUTH DIFFERENCE
   PATTERNS FOR FINENESS RATIO OF 2.5 AT
   18 GHZ FOR LOOK ANGLE OF 17.5 DEG IN
   AZIMUTH AND 45.0 DEG IN ELEVATION.

FIGURE 63. SUM AND ELEVATION DIFFERENCE
   PATTERNS FOR FINENESS RATIO OF 2.5 AT
   18 GHZ FOR LOOK ANGLE OF 17.5 DEG IN
   AZIMUTH AND 45.0 DEG IN ELEVATION.

80

FIGURE 64. SUM AND AZIMUTH DIFFERENCE
PATTERNS FOR FINENESS RATIO OF 0.5 AT
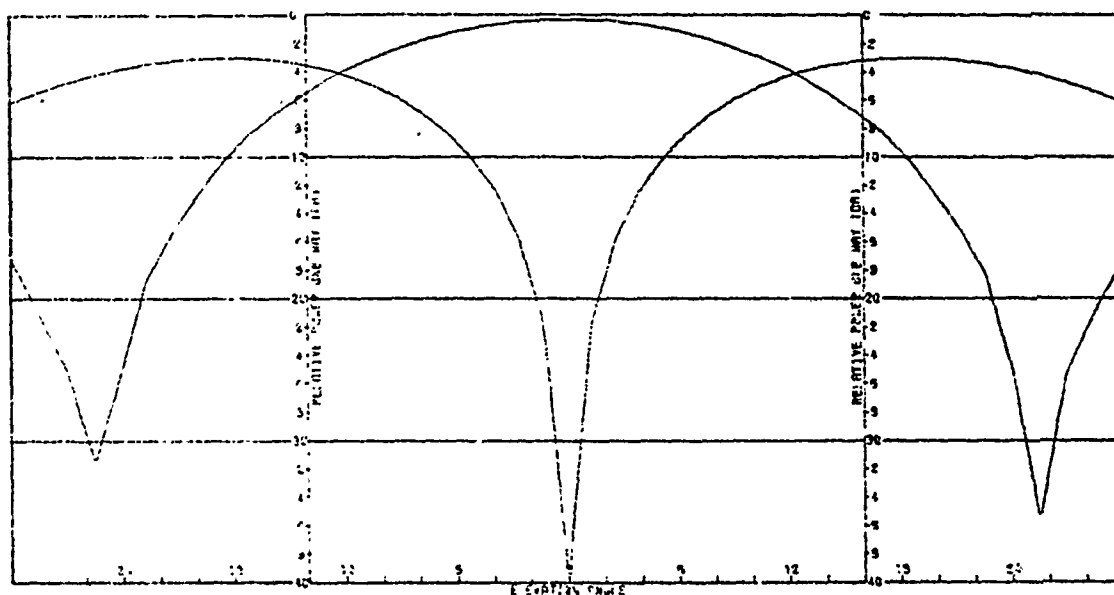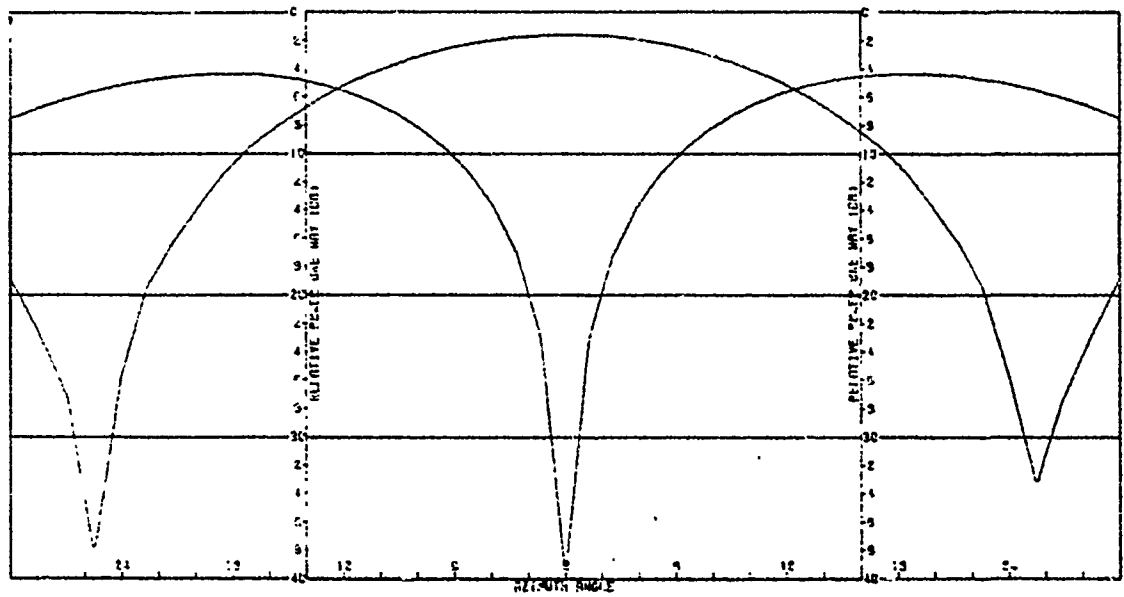8 GHZ FOR LOOK ANGLE OF 0.0 DEG IN
AZIMUTH AND 0.0 DEG IN ELEVATION.

FIGURE 65. SUM AND ELEVATION DIFFERENCE
PATTERN FOR FINENESS RATIO OF 0.5 AT
8 GHZ FOR LOOK ANGLE OF 0.0 DEG IN
AZIMUTH AND 0.0 DEG IN ELEVATION.

81

FIGURE 66. SUM AND AZIMUTH DIFFERENCE
    PATTERNS FOR FINENESS RATIO OF 0.5 AT
    12 GHZ FOR LOOK ANGLE OF 0.0 DEG IN
    AZIMUTH AND 0.0 DEG IN ELEVATION.
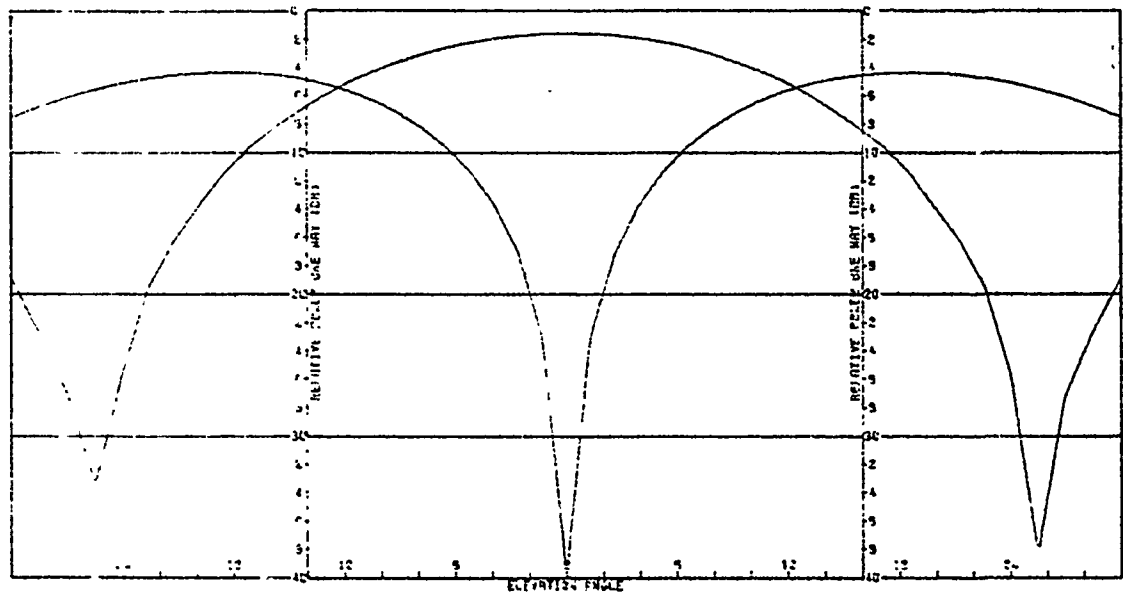

FIGURE 67. SUM AND ELEVATION DIFFERENCE
    PATTERNS FOR FINENESS RATIO OF 0.5 AT
    12 GHZ FOR LOOK ANGLE OF 0.0 DEG IN
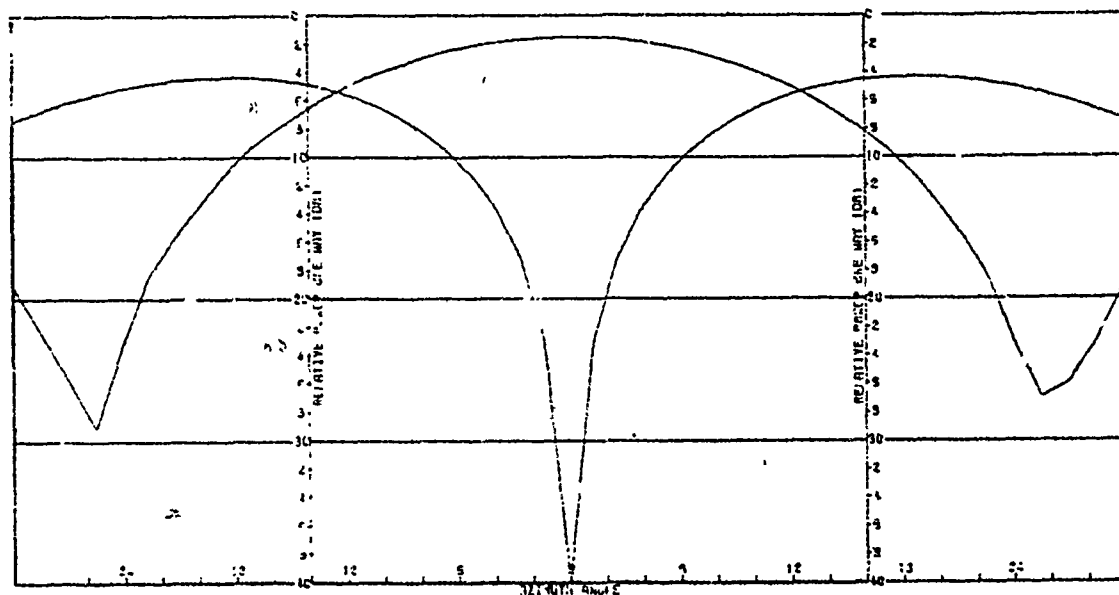   AZIMUTH AND 0.0 DEG IN ELEVATION.

FIGURE 68. SUM AND AZIMUTH DIFFERENCE
PATTERNS FOR FINENESS RATIO OF 0.5 AT
18 GHZ FOR LOOK ANGLE OF 0.0 DEG IN
AZIMUTH AND 0.0 DEG IN ELEVATION.

FIGURE 69. SUM AND ELEVATION DIFFERENCE
PATTERNS FOR FINENESS RATIO OF 0.5 AT
18 GHZ FOR LOOK ANGLE OF 0.0 DEG IN
AZIMUTH AND 0.0 DEG IN ELEVATION.

83

FIGURE 70. SUM AND AZIMUTH DIFFERENCE
PATTERNS FOR FINENESS RATIO OF 0.5 AT
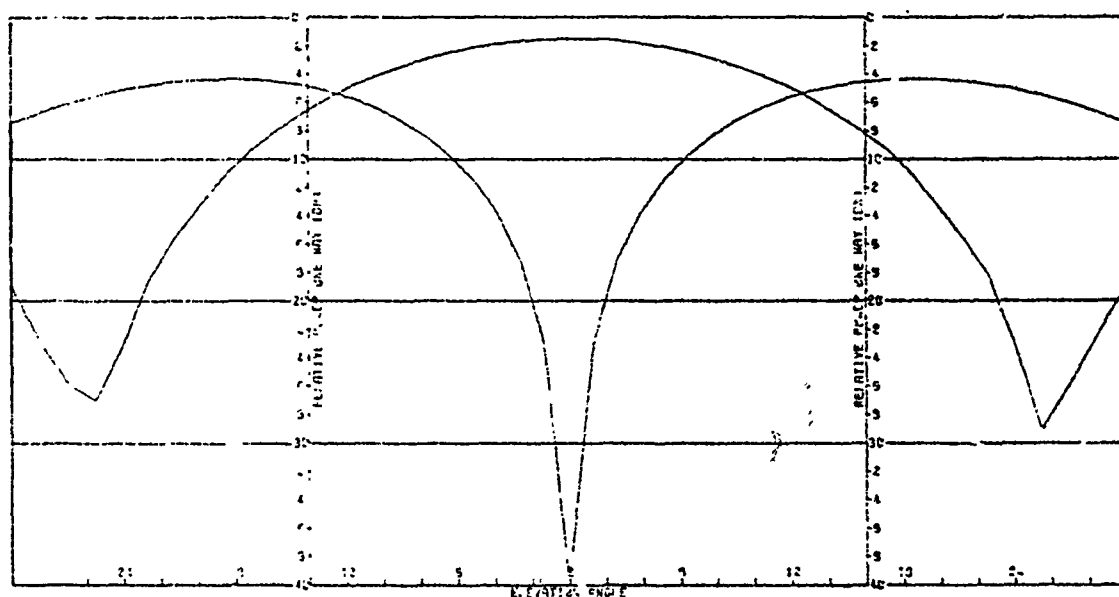8 GHZ FOR LOOK ANGLE OF 17.5 DEG IN
AZIMUTH AND 0.0 DEG IN ELEVATION.

FIGURE 71. SUM AND ELEVATION DIFFERENCE
PATTERNS FOR FINENESS RATIO OF 0.5 AT
8 GHZ FOR LOOK ANGLE OF 17.5 DEG IN
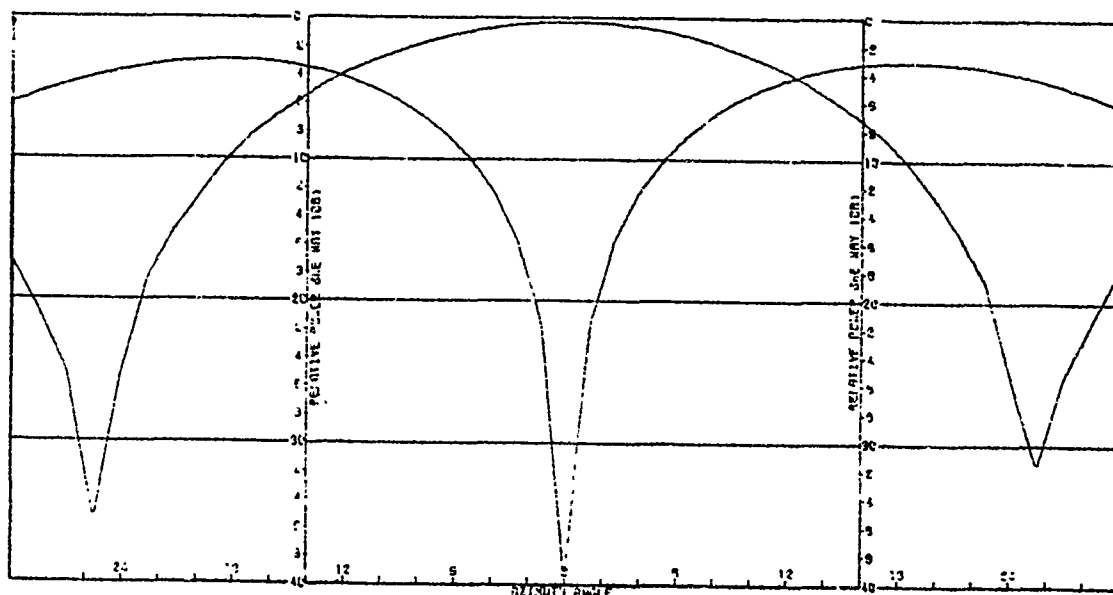AZIMUTH AND 0.0 DEG IN ELEVATION.

84

FIGURE 72. SUM AND AZIMUTH DIFFERENCE
PATTERNS FOR FINENESS RATIO OF 0.5 AT
12 GHZ FOR LOOK ANGLE OF 17.5 DEG IN
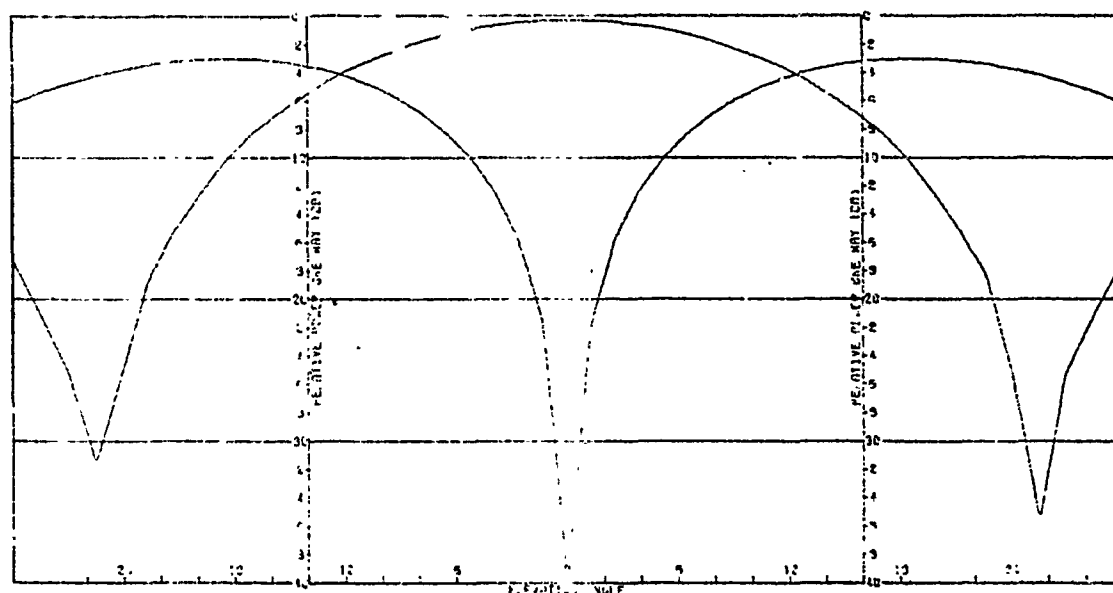AZIMUTH AND 0.0 DEG IN ELEVATION.

FIGURE 73. SUM AND ELEVATION DIFFERENCE
PATTERNS FOR FINENESS RATIO OF 0.5 AT
12 GHZ FOR LOOK ANGLE OF 17.5 DEG IN
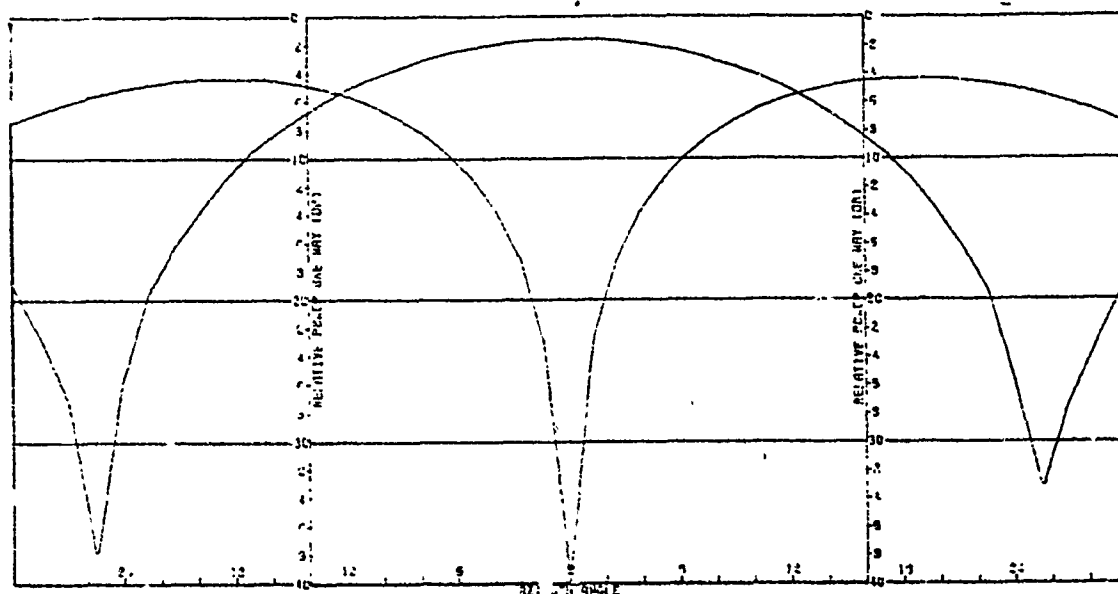AZIMUTH AND 0.0 DEG IN ELEVATION.

FIGURE 74. SUM AND AZIMUTH DIFFERENCE
PATTERNS FOR FINENESS RATIO OF 0.5 AT
18 GHZ FOR LOOK ANGLE OF 17.5 DEG IN
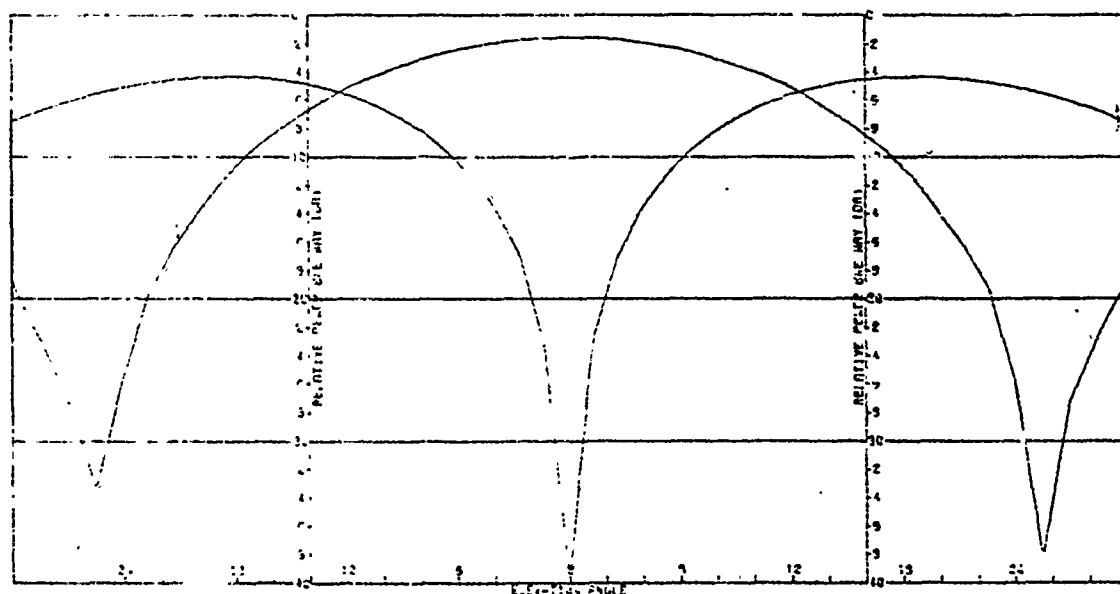AZIMUTH AND 0.0 DEG IN ELVATION.

FIGURE 75. SUM AND ELEVATION DIFFERENCE
PATTERNS FOR FINENESS RATIO OF 0.5 AT
18 GHZ FOR LOOK ANGLE OF 17.5 DEG IN
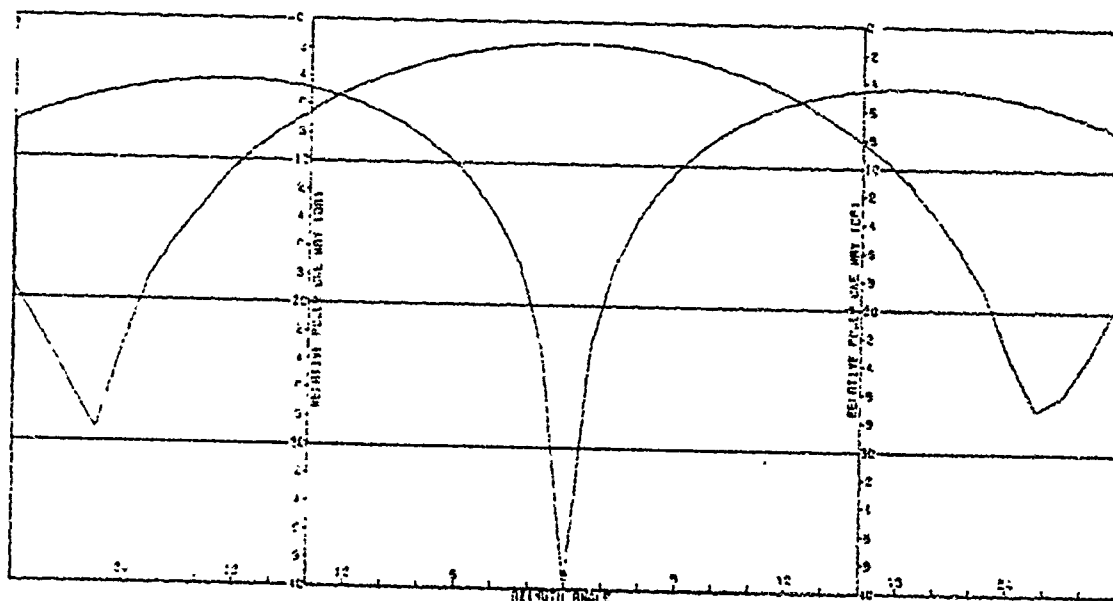AZIMUTH AND 0.0 DEG IN ELEVATION.

FIGURE 76. SUM AND AZIMUTH DIFFERENCE
PATTERNS FOR FINENESS RATIO OF 0.5 AT
8 GHZ FOR LOOK ANGLE OF 40.0 DEG IN
AZIMUTH AND 0.0 DEG IN ELEVATION.

FIGURE 77. SUM AND ELEVATION DIFFERENCE
PATTERNS FOR FINENESS RATIO OF 0.5 AT
8 GHZ FOR LOOK ANGLE OF 40.0 DEG IN
AZIMUTH AND 0.0 DEG IN ELEVATION.

87

FIGURE 78. SUM AND AZIMUTH DIFFERENCE
PATTERNS FOR FINENESS RATIO OF 0.5 AT
12 GHZ FOR LOOK ANGLE OF 40.0 DEG IN
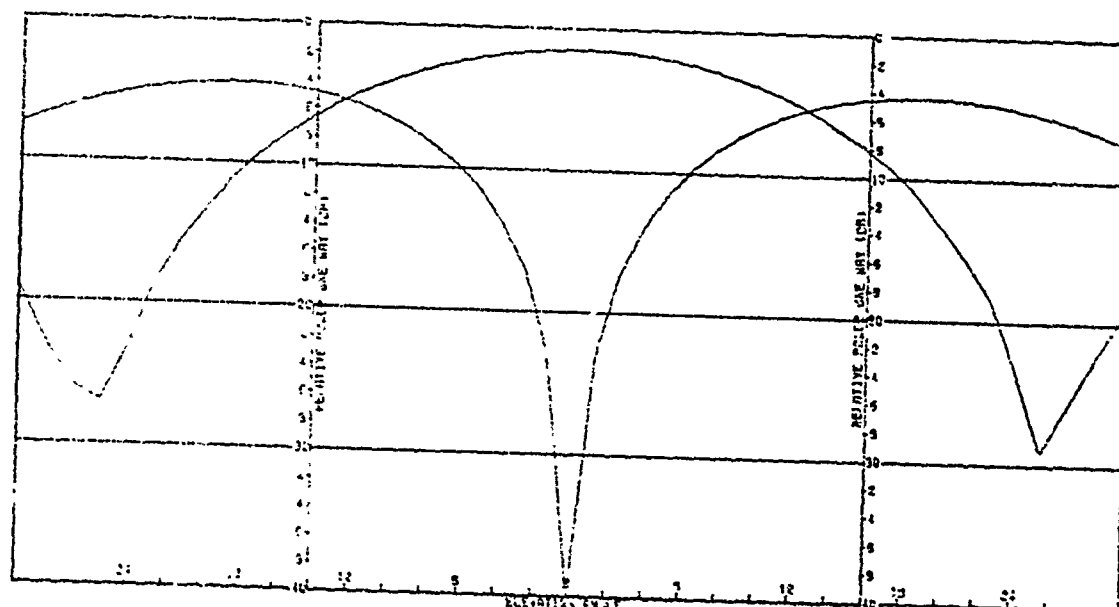AZIMUTH AND 0.0 DEG IN ELEVATION.

FIGURE 79 SUM AND ELEVATION DIFFERENCE
PATTERNS FOR FINENESS RATIO OF 0.5 AT
12 GHZ FOR LOOK ANGLE OF 40.0 DEG IN
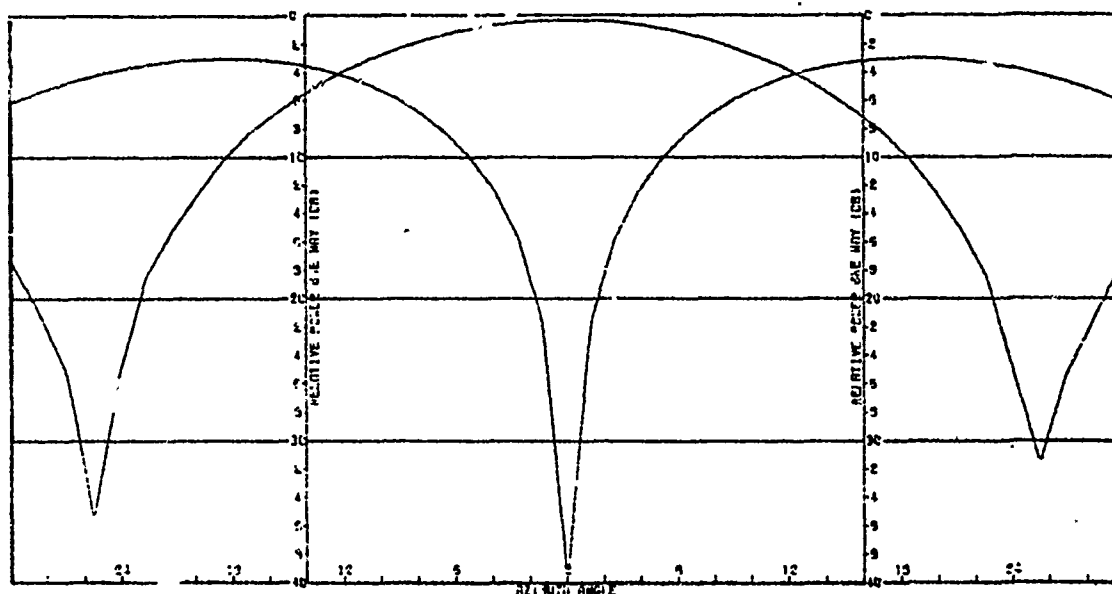AZIMUTH AND 0.0 DEG IN.ELEVATION.

FIGURE 80. SUM AND AZIMUTH DIFFERENCE
   PATTERNS FOR FINENESS RATIO OF 0.5 AT
   18 GHZ FOR LOOK ANGLE OF 40.0 DEG IN
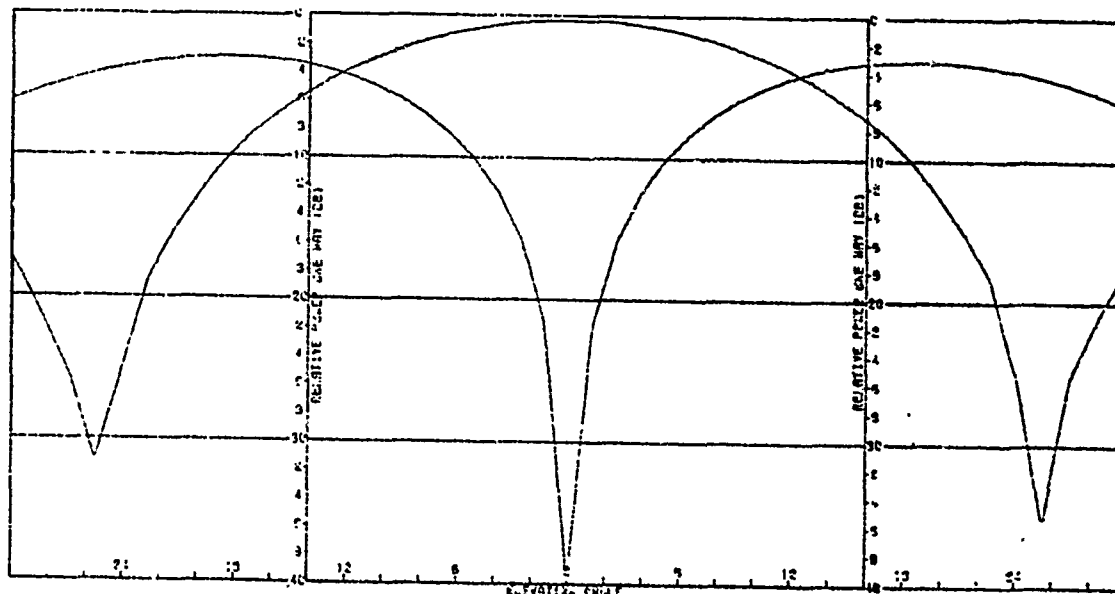   AZIMUTH AND 0.0 DEG IN ELEVATION.

FIGURE 81. SUM AND ELEVATION DIFFERENCE
   PATTERNS FOR FINENESS RATIO OF 0.5 AT
   18 GHZ FOR LOOK ANGLE OF 40.0 DEG IN
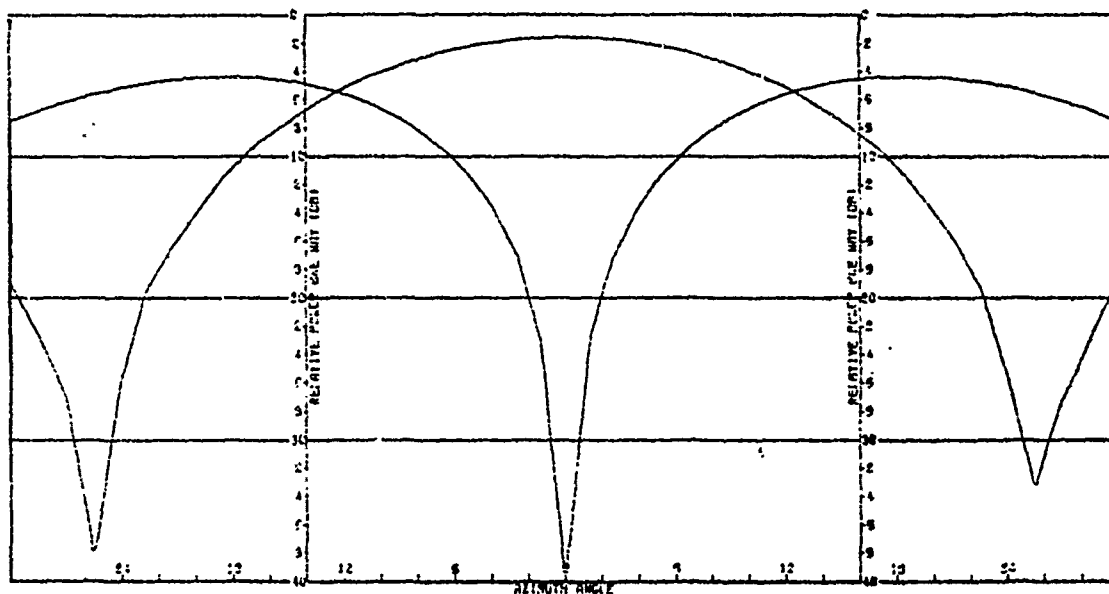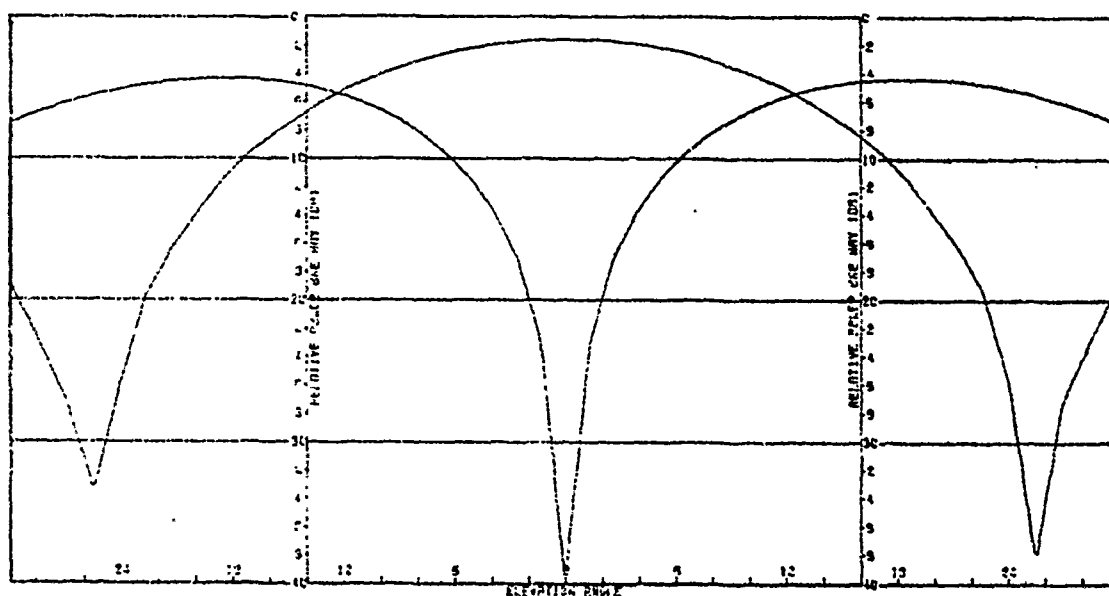   AZIMUTH AND 0.0 DEG IN ELEVATION.

89

FIGURE 82. SUM AND AZIMUTH DIFFERENCE
PATTERNS FOR FINENESS RATIO OF 0.5 AT
8 GHZ FOR LOOK ANGLE OF 17.5 DEG IN
AZIMUTH AND 45.0 DEG IN ELEVATION.

FIGURE 83. SUM AND ELEVATION DIFFERENCE
PATTERNS FOR FINENESS RATIO OF 0.5 AT
8 GHZ FOR LOOK ANGLE OF 17.5 DEG IN
AZIMUTH AND 45.0 DEG IN ELEVATION.

FIGURE 84. SUM AND AZIMUTH DIFFERENCE
PATTERNS FOR FINENESS RATIO OF 0.5 AT
12 GHZ FOR LOOK ANGLE OF 17.5 DEG IN
AZIMUTH AND 45.0 DEG IN ELEVATION.

FIGURE 85. SUM AND ELEVATION DIFFERENCE
PATTERNS FOR FINENESS RATIO OF 0.5 AT
12 GHZ FOR LOOK ANGLE OF 17.5 DEG IN
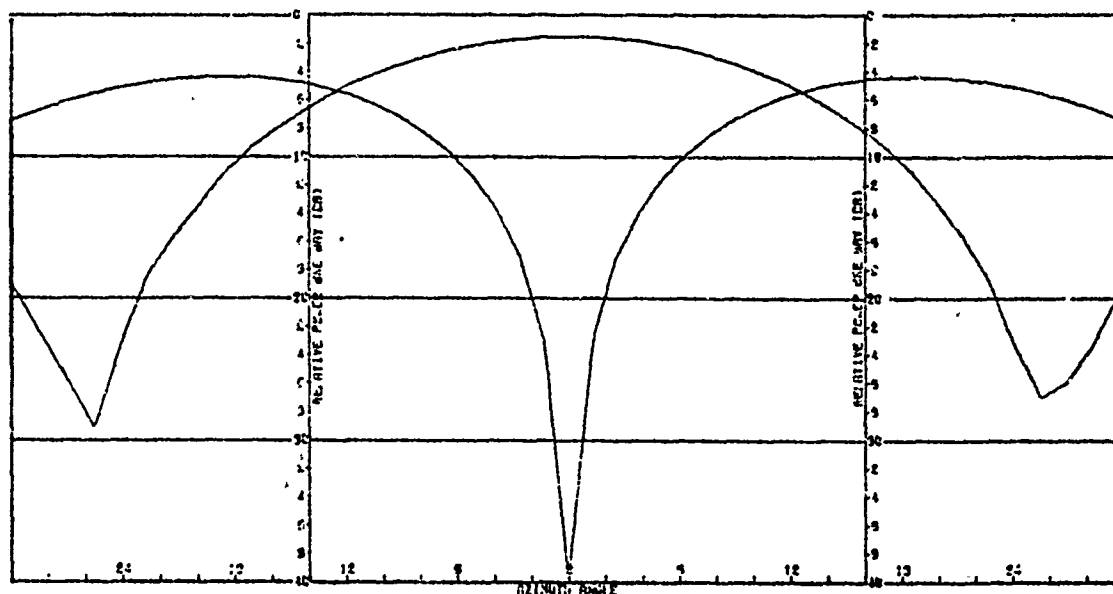AZIMUTH AND 45.0 DEG IN ELEVATION.

91

FIGURE 86. SUM AND AZIMUTH DIFFERENCE
PATTERNS FOR FINENESS RATIO OF 0.5 AT
18 GHZ FOR LOOK ANGLE OF 17.5 DEG IN
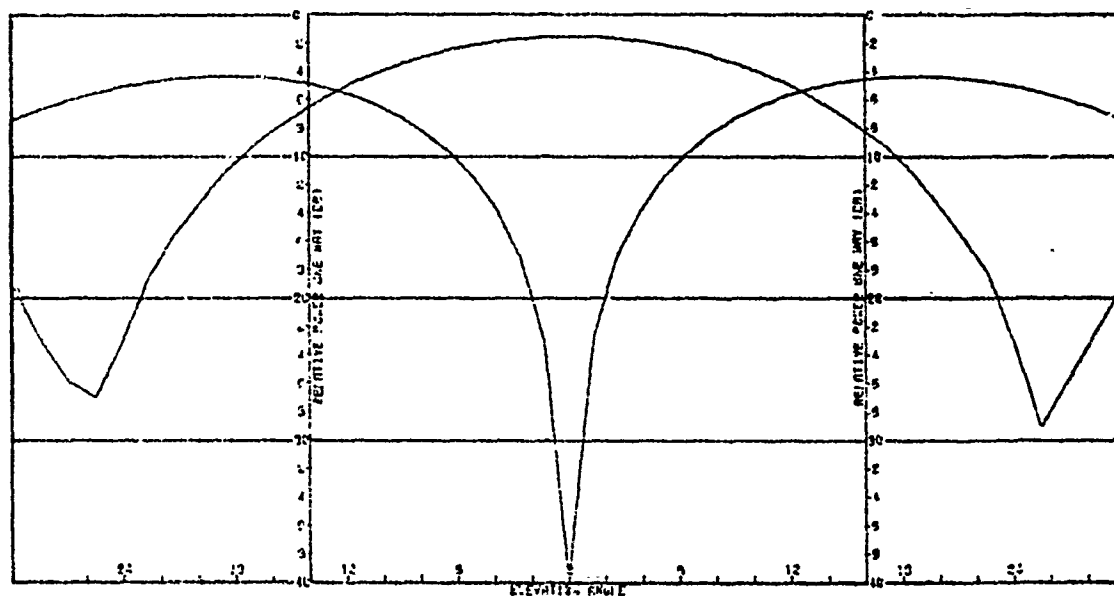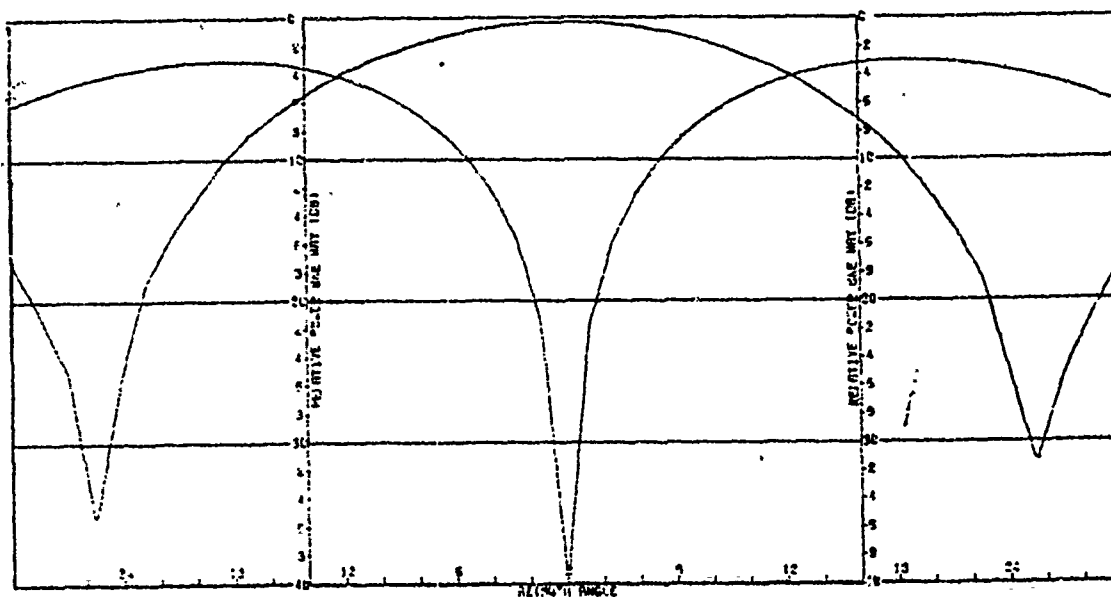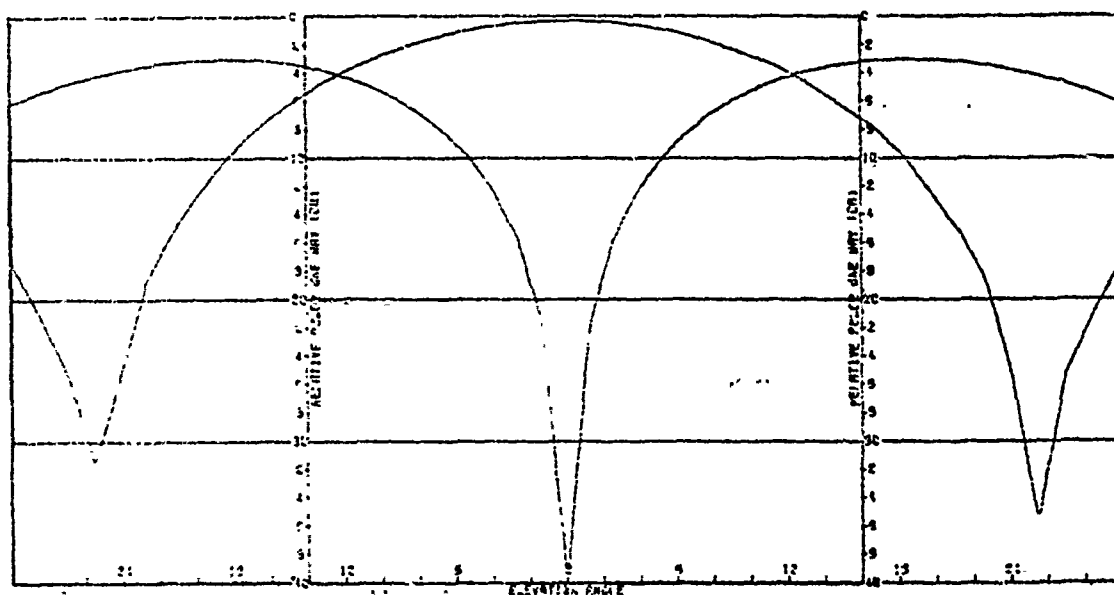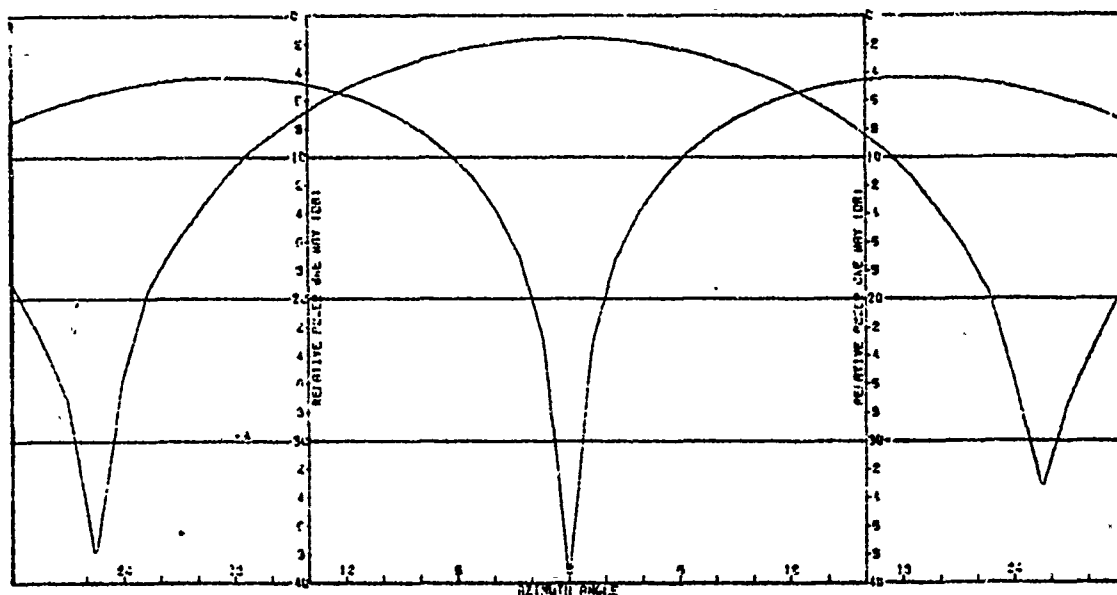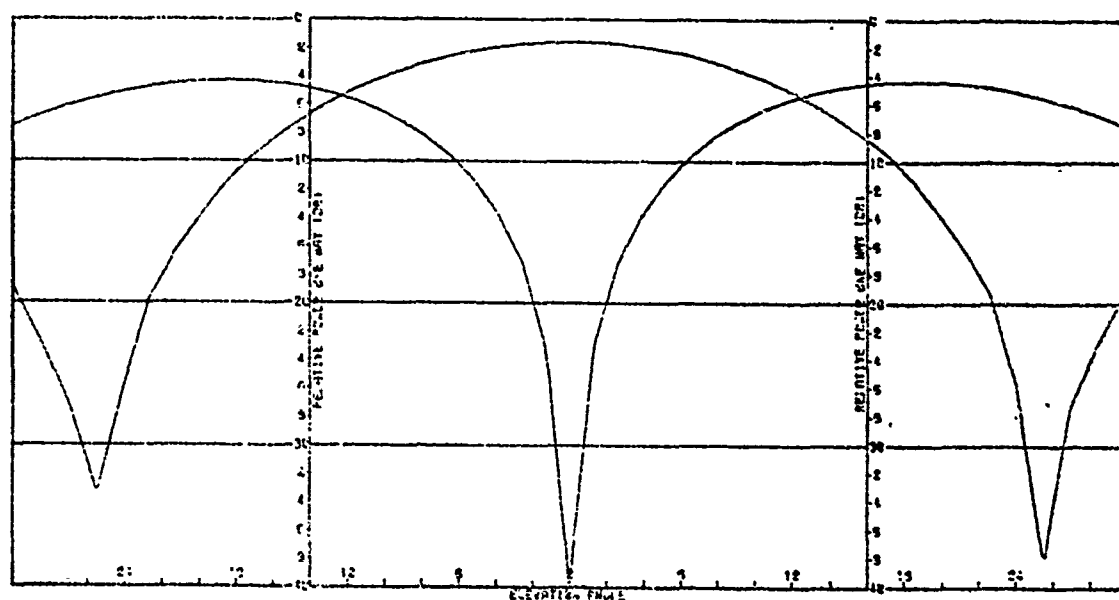AZIMUTH AND 45.0 DEG IN ELEVATION.

FIGURE 87. SUM AND ELEVATION DIFFERENCE
PATTERNS FOR FINENESS RATIO OF 0.5 AT
18 GHZ FOR LOOK ANGLE OF 17.5 DEG IN
AZIMUTH AND 45.0 DEG IN ELEVATION.

SECTION V

CONCLUSIONS AND RECOMMENDATIONS

1. Conclusions

Based on the data presented in Sections II through IV, the following conclusions may be drawn:

(a) Radome Materials

All of the four radome materials considered (fused silica, polyimide quartz, polyimide E-glass, and Pyroceram) were found to have mechanical, thermal, and electrical properties commensurate with the mission of the radome under consideration. Therefore, the selection of a single material for this radome application must be based on small differences in electrical performance and other considerations such as rain erosion resistance, ease of fabrication, cost, and handling in the field.

(b) Radome Shape

Of the six tangent ogive radome shapes considered, the two shapes with fineness ratios of $F = 0.5$ and $F = 2.5$ were found to be electrically superior. Aerodynamically, only those radome shapes having fineness ratios greater than approximately 1.5 will fulfill the minimum range and velocity requirements. All radome shapes having fineness ratios in the range 0.5 to 2.8 were found to be acceptable from a thermal and mechanical point of view.

(c) Wall Structure

Due to the stringent requirements on mechanical strength and maximum radome wall thickness, the monolithic first-order (half-wave) wall structure was selected.

93

2. Recommendations

(a) Radome Composition

It is recommended that the radome be a monolithic first-order (half-wave) wall structure constructed of polyimide quartz material having a dielectric constant of 3.40, loss tangent less than 0.006, and a thickness of 0.299 inch. The thickness is based on Equation (2) when a design frequency of 12 GHz and a design angle of 60 degrees are used. Deciding factors in this recommendation are superior electrical performance, ease of fabrication, and ease of handling in the field.

(b) Radome Shape

It is recommended that the radome shape be a tangent ogive surmounting a 5-inch outside diameter cylinder as shown in Figure 11 with an inside diameter of 4.402 inches. The fineness ratio of the tangent ogive section is recommended to be 2.5 so that both the electrical and aerodynamic performances will be acceptable; however, if the minimum range were reduced, a fineness ratio of 0.5 would be recommended because of its vastly superior electrical performance.

REFERENCES

1. Van Driest, E. R., "The Problem of Aerodynamic Heating," Aeronautical Engineering Review, October 1956.

2. Foye, E. E., "Newtonian Aerodynamics for Tangent Ogive Bodies of Revolution," Report X-671-65-244, Goddard Space Flight Center, June 1965.

3. Bomar, S. H., et.al., Radome Materials Evaluation, Final Technical Report AFAL-TR-73-222 by Engineering Experiment Station, Georgia Institute of Technology for Air Force Avionics Laboratory under contract F33615-72-C-1615, July 1973.

4. Chase, V., Manufacturing Technology for Polybezimidazole Resin in Composite Structures, Technical Report AFML-TR-70-48, Vol. II, by Whittaker Corporation for Air Force Materials Laboratory under contract AF-33(615)1180, January 1971.

5. Joy, E. B. and Huddleston, G. K., "Radome Effects on Ground Mapping Radar," Contract DAAH01-72-C-0598, Georgia Institute of Technology, Atlanta, Georgia, March 1973 and August 1973.

6. Walton, J. D., Radome Engineering Handbook, Design and Principles, Marcel and Decker, Inc., New York, 1970.